Developments in target – ion source chemistry for ISOL facilities

Dissertation

zur Erlangung des Grades

„Doktor der Naturwissenschaften“

im Promotionsfach Chemie

am Fachbereich Chemie, Pharmazie und Geowissenschaften (FB 09)

der Johannes Gutenberg-Universität

in Mainz

Carola Jost

Mainz, den 17.8.2010

1. Gutachter:
2. Gutachter:

Prüfungsdatum: 13.8.2010

Science is the topography of ignorance

Oliver Wendell Holmes, Sr.

Table of Contents

Figures

Tables

1 INTRODUCTION

1.1 Motivation

The question of the origin of our world and the properties of the matter from which it is built has frequently engaged the interest of humankind. For many centuries, scientific explanations of these phenomena seemed utterly out of reach. Since the discovery of radioactivity by H. Becquerel in 1896 (Becquerel, 1896) and the subsequent realization of ongoing nuclear reactions in stars our knowledge of the universe has expanded significantly. But although we have attained considerable knowledge about how the evolution of our universe and the production of elements proceed, we are still a long way from completely understanding these processes. Most interestingly, the investigation of micro and macro cosmos, nuclear physics and astrophysics, are deeply interconnected. Knowledge about nuclear structure and properties helps us understand and simulate processes in space whereas, for example, the existence of the resonance state in ^{12}C was predicted by F. Hoyle (Hoyle, 1954) on the basis of carbon abundance in the universe.

For a deeper understanding of nuclear structure we require experimental data on nuclear masses, half-lives, reaction cross sections, radiation energies and other properties. A powerful method for investigating nuclear properties in laboratories is the use of Radioactive Ion Beams (RIBs). Unstable nuclei that are produced via nuclear reactions are removed from the location of the reaction as a RIB and mass-separated to allow measurement on specific nuclides, which is necessary to attain precise data.

One of the main methods of producing RIBs is Isotope Separation On Line (ISOL). It is used in many research sites all over the world and there are plans to build additional, more powerful facilities of this type.

For the ISOL method the chemistry of the element of interest plays a crucial role, facilitating or hindering the fast extraction of short-lived isotopes as well as the formation of a pure beam. As a typical ISOL target-ion source system runs at temperatures above 1800°C, with high radiation levels and often a mixture of many elements present, its chemistry poses a severe challenge. In order to use the chemical reactions to our advantage we need a more complete understanding of the transport processes involved. One possible approach is to break these processes down in separate parts to be studied off-line. Another is to change only one parameter of the system at a time

while trying to keep the others constant; although in some cases this is impossible due to the complexity of the system.

Data collected from both these approaches will at some point allow us to build up a comprehensive model to describe and predict the complete on-line system. This will enable us to improve and use the powerful tool of ISOL-type RIBs for new experiments to further the understanding of nuclear structure and of our universe.

1.2 Aims and Objectives

One step in the production of RIBs, the transport of reaction products from the target to the ion source, is the main focus of this work. The mechanisms of this diffusion process are strongly dependent on the diffusing species, surface materials and temperatures. As transport rates are crucial, in particular for short-lived reaction products, the parameters of the transfer line are expected to have strong effects on the intensity and purity of a given RIB.

Recently, CERN-ISOLDE demonstrated an ability to reduce 1^{st} and 3^{rd} main group elements as a surface-ionized contamination from a laser ion source, using a low-temperature quartz surface in an angled transfer line (Bouquerel, 2008). However, it is unclear how much of the observed reduction is due to a chemical effect.
The objective of this work was to determine the extent of a possible chemical effect by the transfer line surface and its temperature dependence for several chemical elements. The quantification of this suppression would allow predictions of the yields of a number of species for investigators interested in those regions *per se*, allowing them to evaluate the system's ability to produce sufficient yields.

A simple spectroscopic measurement of ^{131}Cd using a quartz transfer line demonstrates the usefulness of the methods investigated.

2 FOUNDATIONS & LITERATURE

2.1 Radioactive Ion Beam production – In-flight and ISOL

A Radioactive Ion Beam (RIB) is formed from accelerated and ionized unstable nuclear reaction products. The nuclides are subjected to electrostatic and / or magnetic fields so that they can be transported, separated and accelerated to a given energy to suit the needs of physics experiments. The two main objectives in producing RIBs must be the delivery of high-intensity as well as high-purity beams, thus minimizing the signal-to-noise ratio of the acquired experimental data.

Although there are different production methods they have basic principles in common: A primary ion beam consisting of stable or long-lived isotopes (also referred to as projectiles) is used to induce the production of unstable nuclides. The projectiles are ionized and accelerated by a driver accelerator, the acceleration energy depending on the desired nuclear reaction. Common drivers are cyclotrons, linear accelerators (linacs) or synchrotrons. The primary beam impinges on a target and initiates fission, spallation or fragmentation reactions.

The choice of the primary beam and target material is where the RIB production methods differ. The two main possibilities currently in use are in-flight separation and ISOL (Isotope Separation On Line). As the experiments for this work have been done using the ISOL method only, discussion of the in-flight method will be omitted here.

2.2 The ISOL method

The ISOL method is the historically first method for RIB production. It was introduced by O. Kofoed-Hansen and K. Nielsen in 1951 to investigate short-lived Kr isotopes diffusing out of a uranium oxide target (Kofoed-Hansen, 1951). The idea was taken up again about 10 years later and finally led to the design of the ISOLDE facility at CERN which started operation in 1967 (Rudstam, 1965).
The basic principle is the use of a light ion beam on a thick target of a high-mass material to induce nuclear reactions. The primary beam is stopped completely in the target or a catcher as are the recoils from the nuclear reactions. Depending on the energy of the primary beam the target atoms will undergo fission, spallation or fragmentation (see fig 2.1). The reaction products diffuse out of the target material and are transported via a transfer line into an ion source. The produced ions are then

accelerated and the resulting beam of mixed reaction products is fanned out in the magnetic field of an isotope separator. The beam containing the mass of interest is then either post-accelerated to higher energies or directly led to the experimental area.

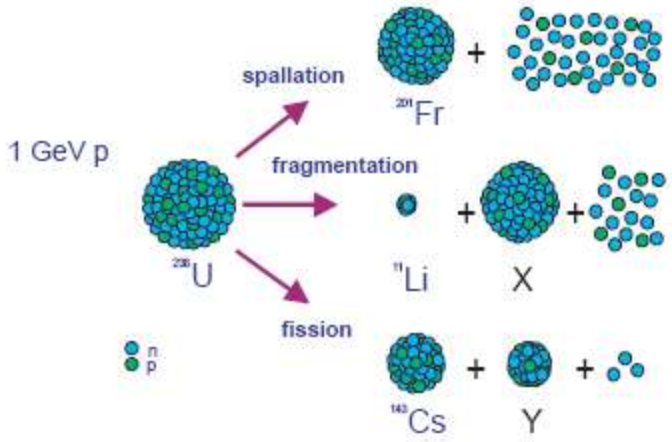

Fig. 2.1: Possible nuclear reactions induced by 1 GeV protons on U

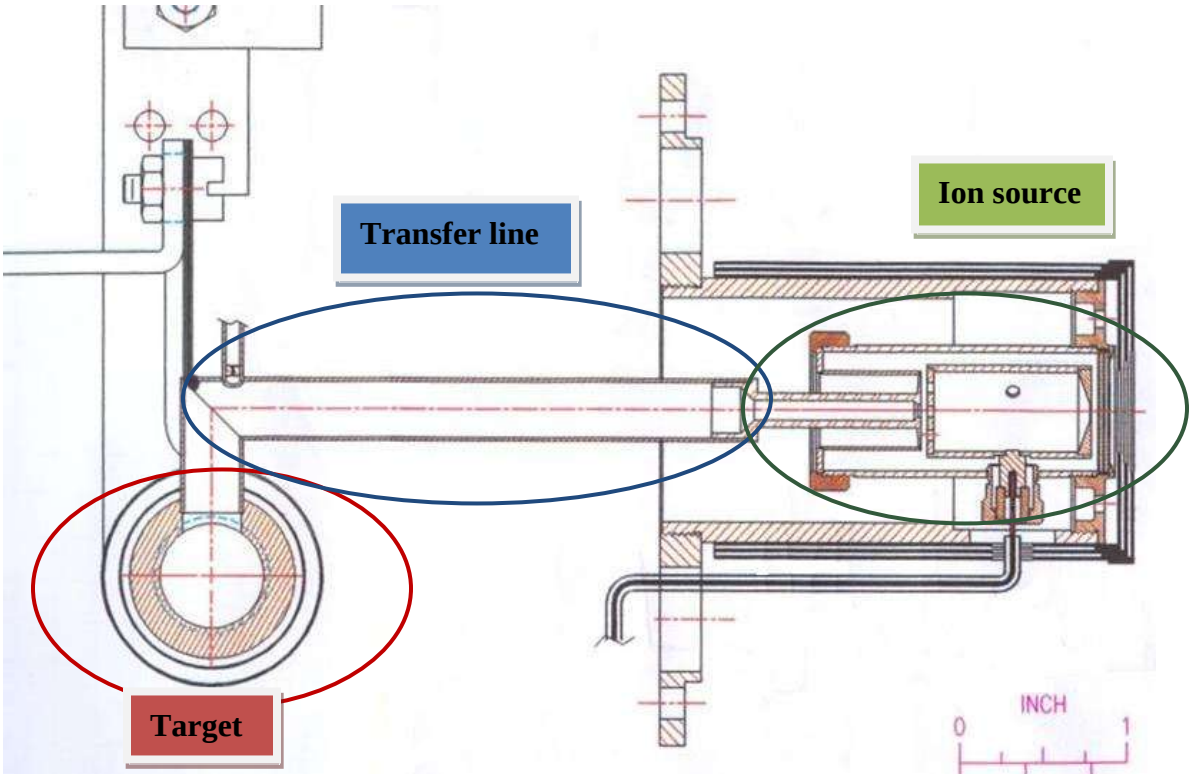

Fig. 2.2: ORNL standard target-ion source system

The ISOL method generally produces higher primary yields with better optical beam quality than the in-flight method. However, the inherent chemical effects in the system completely prohibit the production of beams of several elements, such as the refractories.

The yield of a given nuclide produced from an ISOL system can be described thus:

$$Y = N_t \, \Phi \, \sigma \, \varepsilon_{target} \, \varepsilon_{transport} \, \varepsilon_{ion} \qquad (2.1)$$

with N_t the number of atoms per unit area in the target, Φ the primary beam flux, σ the cross section of the nuclear reaction and ε the efficiencies of diffusion in the target, transport to the ion source and ionization (see fig. 2.2). To optimize the yields all efficiencies should be as high as possible. Both the efficiencies of target and transport are inversely dependent on the time it takes the atom to complete these processes since the radioactive nuclides will decay. Therefore fast release from the entire system is one of the main concerns in target-ion source development.

2.2.1 ISOL targets

The ISOL method uses targets of sufficient thickness to reduce the primary beam to energies at which it does not induce any more nuclear reactions. This maximizes the production rates R. Thus the length of the usually cylindrical target depends on the energy of the projectile beam. The diameter is defined by achievable beam focus; it is also dependent on beam intensity and energy through the amount of heat the target material can dissipate.

The diffusion of the produced radionuclides through the target material to its surface is usually the main process delaying the release from the target-ion source unit. Theoretical descriptions of diffusion behavior can be found in the literature, *e.g.* by Glicksman (Glicksman, 2000). The basis is Fick's second law (Fick, 1859) and the boundary condition:

$$\left(\frac{\partial C(\vec{r},t)}{\partial t}\right) = \nabla^2 C(\vec{r},t) \qquad (2.2)$$

$$D\left(\frac{\partial C(\vec{r},t)}{\partial \hat{n}}\right) = kC_s \qquad (2.3)$$

with $\vec{r}$ and t describing space and time, C the volumetric density of atoms, D the diffusion coefficient described by the Arrhenius equation (eq. 2.4), C_s the density of atoms on the surface and k a proportionality constant.

$$D = D_o exp\left(-\frac{Q}{RT}\right) \quad (2.4)$$

with Q the activation energy for diffusion, R the universal gas constant and T the temperature in K.

Assuming that the residence time of atoms on the surface of the target is short compared to diffusion times, that there is a homogenous distribution of atoms and that the diffusion coefficient is independent of space and time, Fujioka (Fujioka, 1981) gives the following equation for the diffusion flux f:

$$f(\hat{t}) = \frac{2n}{\pi^2}\sum_{m=1}^{\infty}\frac{exp(-N_m \hat{t})}{N_m}, \quad (2.5)$$

valid for foils/slabs (n = 1), fibers/cylinders (n = 2) and particles/spheres (n =3),

$$N_m = \begin{cases} (m-1)^2 \text{ ; } n=1 \\ (j_{0,m}/\pi^2) \text{ ; } n=2 \\ m^2 \text{ ; } n=3 \end{cases}$$

Where $\hat{t}$ is a non-dimensional parameter corresponding to the ratio of the elapsed time to the diffusion time constant,

$\hat{t} = \frac{t}{\tau_D}$; $\tau_D = \frac{1}{\eta} = \frac{a^2}{\pi^2 D}$,

2a being the thickness of the slab or the diameter of the cylinders or spheres. $j_{0,m}$ represents the m^{th} positive root of the Bessel function of order zero.

As can be seen in eq. 2.4 and 2.5, the main parameters to influence diffusion are target geometry, its diffusion activation energy and the target temperature. To minimize diffusion and desorption (from the surface) times the target is usually kept at temperatures above 1800°C (or at the maximum temperature the target material can withstand). Target materials are metals and their compounds in various forms. They are enclosed in a high-temperature stable, chemically inert (towards the target material) target container.

Another important trait apart from good release properties is the stability of the material. It must be able to maintain low vapor pressures at high temperatures and withstand prolonged periods of heating and irradiation without structural changes. Metal targets

can be made from massive material, foils or powders. Metal-compound targets, usually carbides or oxides, are made from pressed powders, fibers or a framework like graphite foam coated with the respective compound.
Each of these target materials exhibits specific release properties for every element produced and must therefore be carefully chosen to suit the desired beam. Release characteristics depend on the diffusion behavior as well as the effusion of the element. Whichever of those delays forms the rate-determining step for the release must be minimized by the target design to allow the release of short-lived reaction products.

2.2.2 ISOL transfer line

Target and ion source are connected via a short tube (see fig. 2.2), most often made from tantalum, to allow transport of the reaction products. Atoms will randomly move within the vacuum system until they reach the ion source. Since the system is typically under molecular flow conditions (that is, no pressure gradient exists), the trajectories of the particles are straight lines between wall collisions (see fig. 2.3). This transport process is commonly called “effusion”. In a typical transfer line (~ 5 cm length) an atom will experience about 500 collisions with the tube’s inner surface before it reaches the ion source.

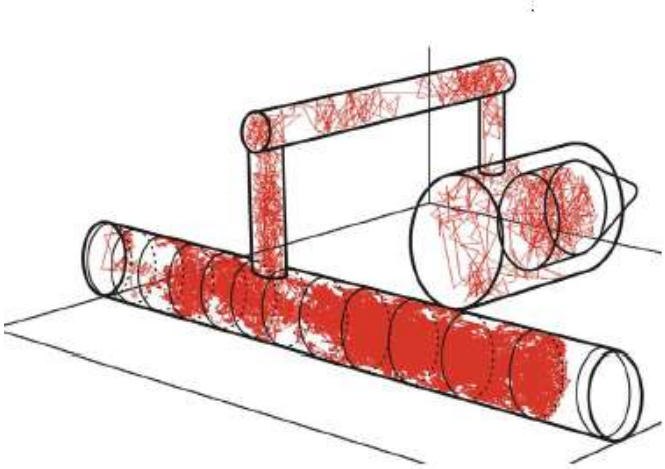

Fig. 2.3: Path of an atom travelling out of a foil target to the ion source (RIBO code, (Santana-Leitner, 2005))

When a particle collides with the inner walls of the transfer line, there are three possible interactions:

a) reflection
b) reversible adsorption
c) irreversible adsorption

Which interaction will actually occur depends on the primary chemical valence forces of both the surface and the incoming atom; that is, it varies with the amount of electrons in the outer shells of the element and its chemical state (elemental or compound). It also varies with surface coverage γ_i, which is described as follows (Kogan, 1969):

$$\gamma_i = N_i \tau_a \sigma \qquad (2.6)$$

with N_i the bombarding flux, τ_a the sticking time and σ the chemical adsorption cross section.

a) In the case of *reflection* there are two possible mechanisms, elastic and diffuse reflection:

Elastic reflection conserves the energy of the atom and the reflection angle is dependent on the incoming angle (see fig. 2.4). This mechanism is rare since surfaces usually are not flat on a microscopic scale; also, there can be no chemical interactions between the surface and the atom.

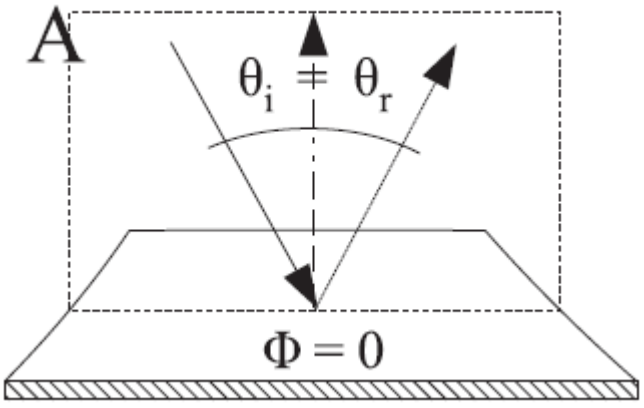

Fig. 2.4: Elastic reflection

Diffuse reflection happens when there is a chemical interaction. The energy of the atom is not conserved. The outgoing angle is incident-angle independent and can be described by the cosine law (Lambert, 1760) or the Lorentz-Lambert model (normalized to solid angle Ω, see fig. 2.5):

$$p(\theta)_\Omega \propto \cos(\theta) \tag{2.7}$$

with $p(\theta)_\Omega$ the probability of the atom leaving at an angle θ.

In this type of reflection the atoms are generally thermalized and their speed is distributed along a Maxwell-Boltzmann curve (Maxwell, 1866):

$$f(v_i) = \sqrt{\frac{m}{2\pi kT}}\, exp\left[\frac{-mv_i^2}{2kT}\right] \tag{2.8}$$

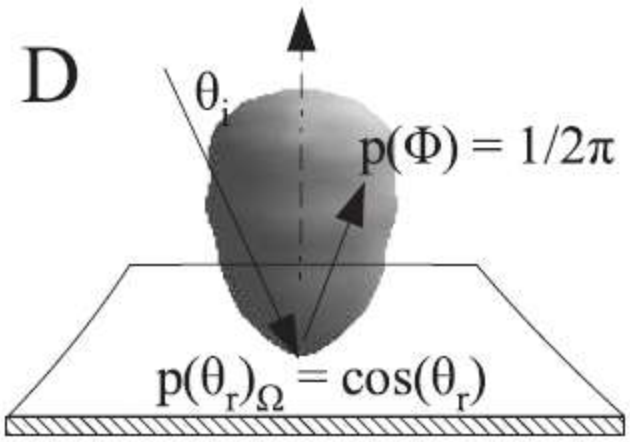

Fig. 2.5: Diffuse reflection

b) In case of *reversible adsorption*, the atom will stick to the surface for some time, usually as a result of a chemical interaction, and then return to the gas phase. Sticking times t_s can be described by the Frenkel equation (Loeb, 1934):

$$t_s = t_0 exp\left(-\frac{\Delta H_{ads}}{kT}\right) \tag{2.9}$$

with t_0 the inverse of the Debye frequency, ΔH_{ads} the adsorption enthalpy, k the Boltzmann constant and T the temperature of the surface.
Atoms return to the gas phase at an angle according to the cosine law and a Maxwell-Boltzmann distribution in speed.

c) There is also the possibility of *irreversible adsorption*. This can be caused by several mechanisms: Condensation, irreversible chemical reaction or diffusion into the bulk of the adsorbent.

To keep residence time on the surface as short as possible, standard transfer lines must be operated at high temperatures (see eq. 2.9). This is often achieved by running the current used for heating the ion source though the transfer line as well (see fig.2.2).

In some cases the difference in residence time on transfer line surfaces has been used to achieve higher beam purity. A very important case is the use of water-cooled transfer lines for the production of beams of volatile species (S. Sundell, 1992). Another example is the quartz transfer line employed at CERN-ISOLDE to retain easily surface-ionized elements from group 1a and 3a (Bouquerel, 2007).

2.2.3 ISOL ion sources

Ionization of the reaction products can be achieved by surface, laser or plasma ion sources.

Surface ion sources can be used to produce positive or negative ions but they usually exhibit good efficiencies only for the elements with the lowest ionization energies or highest electron affinities. For elements with ionization potential < 5eV (alkalis and alkaline earths) or electron affinities > 2 eV (halogens) the Saha-Langmuir equation (Langmuir, 1925) gives ionization efficiencies of 50-100%:

$$\frac{N_+}{N_0} = \frac{g_+}{g_0} \exp\left(-\frac{e(\Phi - V)}{kT}\right) \qquad (2.10)$$

with N_+, N_0 the number density of positive ions and neutral atoms, g_+, g_0: statistical weights of ions and neutral atoms (material constants), e the electronic charge, Φ the surface work function, V the first ionization potential of the atom and T the equilibrium temperature of the system (Dresser, 1968).It can be seen that the temperature of the ionization surface plays a crucial role and must thus be kept at high values.

The ion source consists of simple tube coated with a material with a high work function (for positive ionization, e.g. W) or a low work function (for negative ionization, *e.g.* LaB_6) (see fig. 2.6).

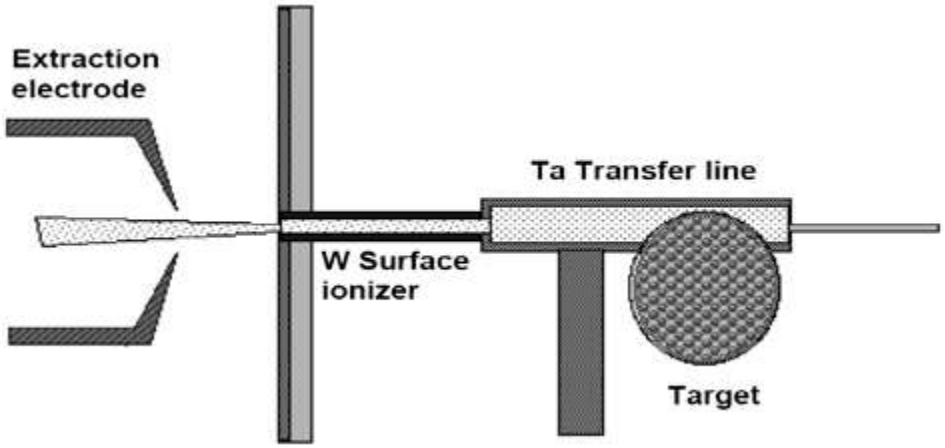

Fig. 2.6: ISOLDE surface ion source

Laser ion sources have the same basic geometry as a surface ion source (see fig. 2.6). The laser beam is focused in the tubular ionizer. It consists of laser light of different wave lengths, each tuned to a specific electronic transition of the element of interest, finally exciting the electron to the continuum and ionizing the atom. Thus laser ionization is a highly selective method. Unfortunately the ionization cavity needs to be kept at high temperatures to reduce sticking times. This leads to contaminations by easily surface-ionized species. Therefore a laser ion source is not selective *per se* but only improves the ratio of the laser-ionized element vs. the surface-ionized contaminations.

Plasma ion sources are the least selective sources used for RIB production and are employed for elements that cannot be ionized with a surface or laser ion source. Ions are produced in a magnetically confined plasma, which can be defined as: “a quasi-neutral gas that exhibits collective behavior when exposed to external electro-magnetic fields” (Wolf, 1995). There is no well defined phase transition point from the gaseous state to the plasma which consists of electrons, ions and neutral atoms or molecules. The most significant difference between a plasma and a neutral gas is the number of freely moving charges that make the plasma a good conductor. An ionized gas can be considered a plasma if the following, so-called plasma conditions are fulfilled:

- The typical length scale (dimension) L of the plasma has to exceed its shielding length λ_D (Debye length). The Debye length determines how far the charge imbalance due to thermal motion in the equilibrium state or the impact of an external electric potential can extend in the plasma or in the ionized medium. The condition can be written for electrons as (Wolf, 1995):

$$L \gg \lambda_0 = \sqrt{\frac{\varepsilon_0 k T_e}{e^2 n_e}} \qquad (2.11)$$

where ε_0 is the permittivity constant (≈ 8.854·10^{-12} F/m), k the Boltzmann constant (≈1.38·10^{-23} J/K), T_e the electron temperature (in Kelvin), e the elementary charge (≈1.602·10-19 C) and n_e, the electron density. If this condition is not met, the plasma is not necessarily macroscopically neutral.

– In order to have collective behavior, the number of particles inside the Debye sphere must be sufficiently high such as:

$$n_e \lambda_D^2 \gg 1 \qquad (2.12)$$

– The frequency f_{pe} of collective plasma (electron) oscillations must be higher than the collision frequency v_{en} of electrons and neutrals

$$f_{pe} = \frac{\omega_{pe}}{2\pi} = \frac{1}{2\pi}\sqrt{\frac{e^2 n_e}{\varepsilon_0 m_e}} > v_{en} \qquad (2.13)$$

where m_e is the electron mass (≈ 9.11·10-31 kg). Equation (2.13) defines the plasma oscillation frequency ω_{pe}. This condition is fulfilled as the degree of ionization of the plasma increases. Usually the ionized gas can be considered to be a plasma when its degree of ionization exceeds a few percent (Stix, 1992).

The most popular plasma source, the FEBIAD (Forced Electron Beam Induced Arc Discharge, see fig. 2.7, (S. Sundell, 1992)) or EBPIS (Electron Beam Plasma Ion Source, (Carter, 1997)) operates at the lower limit of the plasma parameters given above. A cathode is heated by an electron current flow to 2000° C. At this temperature the Ta surface emits electrons (thermionic emission) which are accelerated towards the anode grid. Atoms in the path of the electrons will be ionized and a plasma is formed. The density of the plasma can be influenced by the magnetic field of one or several solenoid magnets to achieve maximum ionization efficiencies. Efficiencies from a plasma ion source can be in the range of 50% for most elements except the lighter noble gases (Wolf, 1995).

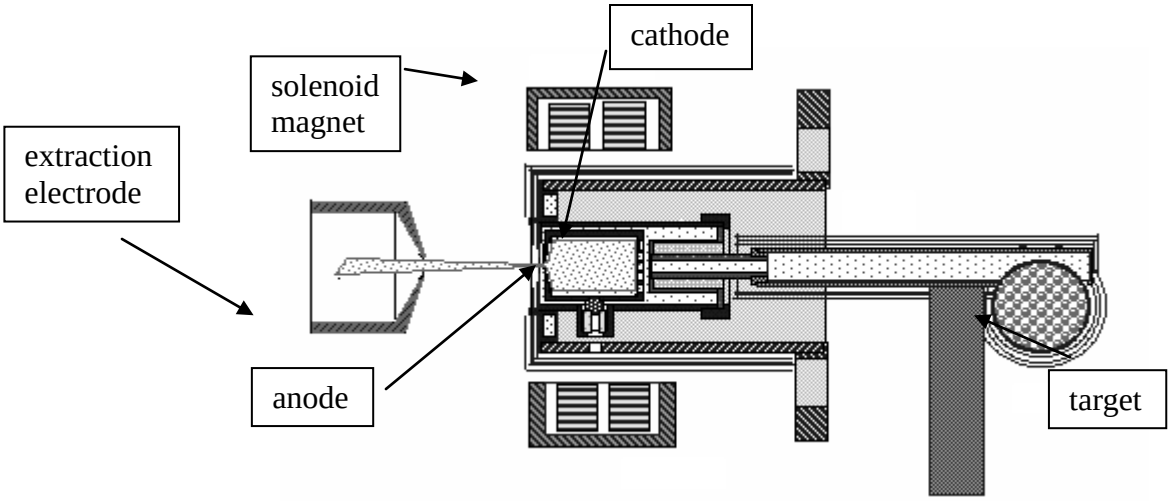

Fig. 2.7: ISOLDE FEBIAD ion source

2.2.4 Beam purity

Ideally, experiments with RIBs should be conducted with isobarically pure beams, *i.e.* beams containing only one nuclide of a given mass. Magnets are used for separation of nuclides. In practice, the mass resolution of separator magnets is almost always too low to achieve this. Since the nuclides of interest for physics experiments typically have short half-lives and low production rates relative to their isobars, isobaric contaminations often make up a considerable percentage of the beam. A chemical / element selective step in the production chain can help improve beam purity (see fig. 2.8).

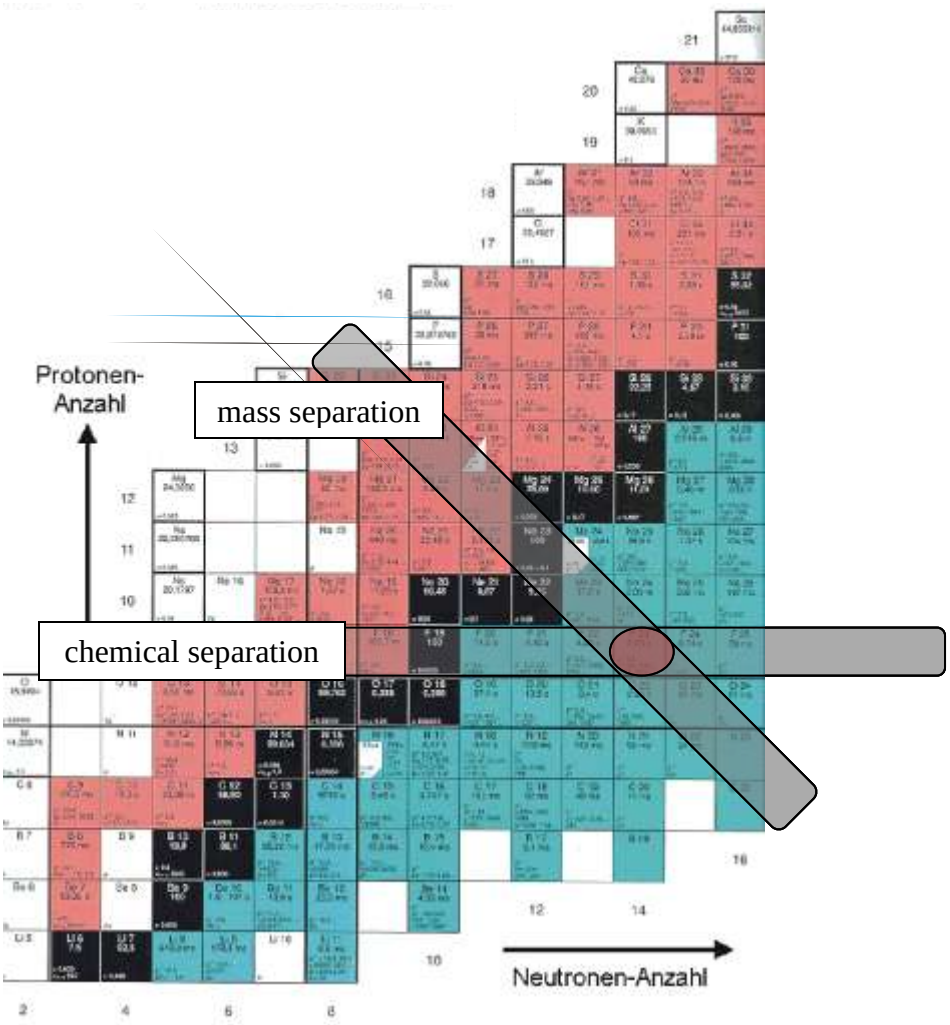

Fig 2.8: A and Z separation

Chemical selectivity can be implemented by employing differences in:

a) ionization – different ionization methods
b) effusion time – sticking times on surfaces are dependent on the chemical species
c) diffusion time – target materials will influence diffusion of elements
d) reactivity – elements that form a stable molecular ion can be mass-separated at a different mass

The basic idea of a) is to use the differences in ionization potentials and electron affinities of elements to separate them. It is utilized in selective ion sources like surface or laser ion sources. Another application is photodetachment where a laser is used to neutralize negative ions of an element contaminating the beam (Liu, 2009).

Method b) encompasses both sticking times on the target surface and the inner surfaces of the target-ion source unit. Parameters controlling these are temperature, the structure and material of surfaces, the chemical state of elements and the concentration of reactive chemicals present. Usually these parameters are interdependent. Recent studies on this have been conducted by Bouquerel et al. (Bouquerel, 2007), (Bouquerel, 2008) at CERN-ISOLDE, investigating the effects of a medium to low temperature transfer line with a quartz glass surface on the yields of a number of elements. They have found considerable reductions of yields for alkali metals and 3rd main group elements while yields of Zn and Cd remained unchanged. However, the exact mechanism of this effect is not known.

Method c) is concerned with the diffusion inside the target, which is influenced by temperature, the chemical composition and structure of the target material, its density and shape (grains, fibers). A lot of current research (Kronenberg, 2008) is focused on understanding how these parameters affect diffusion and optimizing target materials for fast release.

Method d) uses differences in reactivity to mass separate a nuclide as a molecular ion rather than in the elemental state. A recent example for beam purification using this effect is the use of the SnS molecule for production of pure Sn beams. After diffusing to the target surface Sn reacts with the S provided by saturating the system with H_2S. The SnS molecule desorbs faster than elemental Sn from both target and Ta surfaces, leading to increased yields especially at shorter half-lives. It can form stable positive as well as negative ions. Since the isobaric contaminations do not form sulfide ions and a mass separation takes place at the mass A(Sn+S) before the tandem accelerator (see chapter 2.3.2) and at A'(Sn) after post-acceleration (see eq. 2.14), the purity of Sn beams produced by this method can approach 100% (Stracener, 2003).

$$Sn + S \longrightarrow SnS \xrightarrow{I.S.} SnS^{+} \xrightarrow{C.E.} Sn^{-} \xrightarrow{tandem} Sn^{+} \qquad (2.14)$$

2.3 ISOL Facilities

There are currently four major ISOL facilities in the world: CERN-ISOLDE in Switzerland, GANIL-SPIRAL in France, HRIBF in the USA and ISAC-TRIUMF in Canada. Although they are all using the basic ISOL method they differ in their driver

accelerators and the primary beam energies they can achieve as well as their target-ion source designs and post-acceleration energies; therefore, beam intensities and qualities for a given isotope will vary with the facilities.
There are several new ISOL facilities / upgrades planned throughout the world, aiming at higher production rates by improving primary beam intensity, targets, and ion sources. Ongoing projects are SPIRAL2, HIE-ISOLDE and SPES in Europe, as precursors for a planned EURISOL facility, as well as a possible ISOL station at the planned in-flight facility FRIB at Michigan State University.
Since the online experiments described herein have all been conducted at HRIBF and ISOLDE, only those two facilities and their differences will be discussed.

2.3.1 CERN-ISOLDE

ISOLDE uses the CERN proton synchrotron booster (PSB) as driver accelerator (see fig. 2.9). It delivers pulses of 1.0 or 1.4 GeV protons that, with up to half the pulses of the 14.4 s super cycle delivered to ISOLDE, can amount to a current of up to 4μA. Because of the high energy of the primary beam it induces spallation as well as fission and fragmentation reactions, producing a wide range of nuclides from a given target.

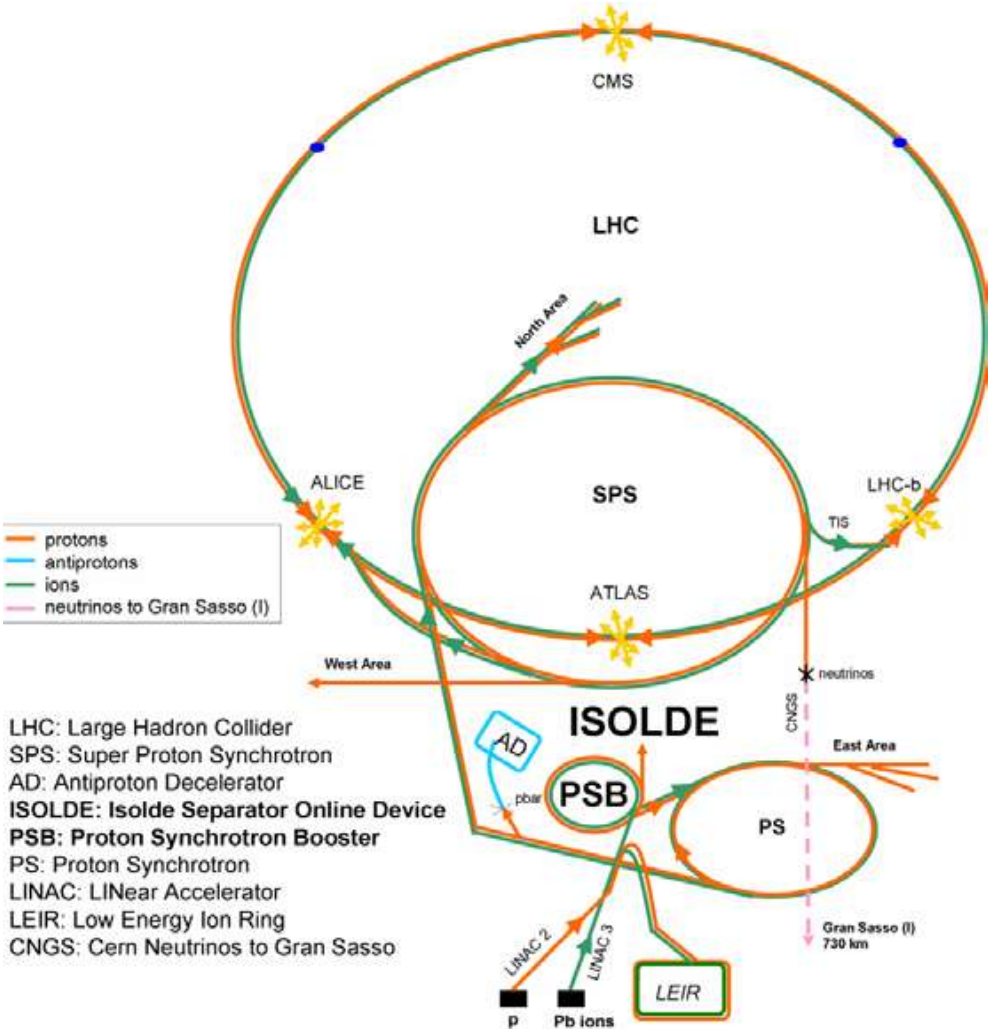

Fig. 2.9: CERN accelerator layout

ISOLDE has two target stations, one each for the high resolution (HRS) and general purpose separator (GPS) (see fig. 2.10). While the GPS station can deliver up to three beams of different masses simultaneously, the HRS is limited to one mass.
The majority of the experiments at ISOLDE are conducted with low-energy beams. For post-acceleration, the linear accelerator REX can provide up to 3.1 MeV/u.
ISOLDE has developed a wide variety of targets and ion sources and produces isotopes of 73 elements. Ion sources used are surface, laser and plasma types. The high energy of the proton pulses imposes severe thermal and mechanical stresses on the targets and the target-ion source unit.

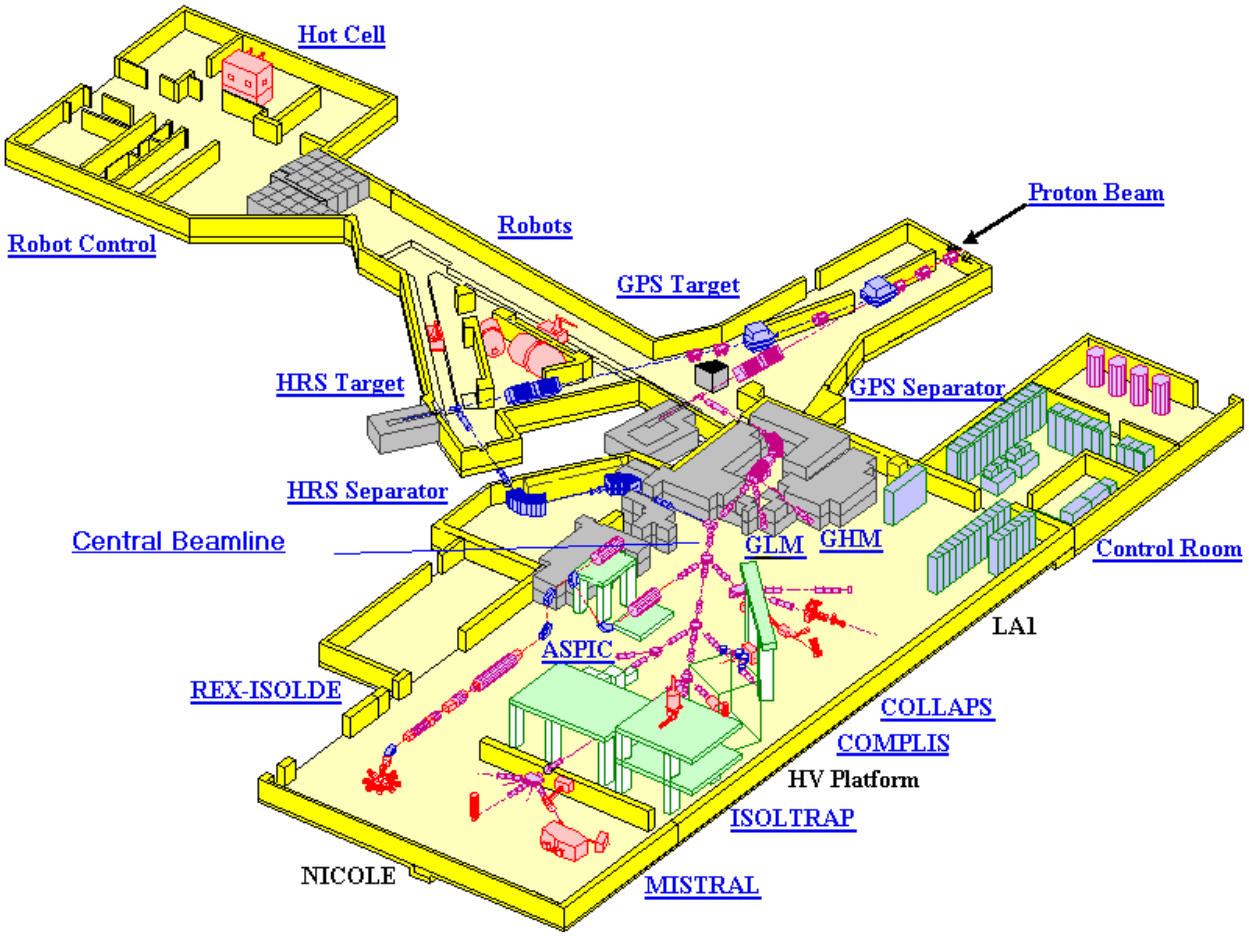

Fig. 2.10: ISOLDE facility layout

2.3.2 Holifield Radioactive Ion Beam Facility (HRIBF)

The HRIBF at the Oak Ridge National Laboratory (ORNL) uses the Oak Ridge Isochronous Cyclotron (ORIC) as a primary driver (see fig. 2.11). It produces continuous beams, with a maximum of 20 μA of up to 54 MeV protons, 12 μA of 49 MeV deuterons and 10 μA of 85 MeV α-particles. Due to the low energy of the primary beam, the production reactions are limited to fission and compound nucleus reactions. The latter produce only a small range of nuclides very close to the target nucleus.

HRIBF also has two production target stations, IRIS1 (Injector for Radioactive Ion Species) and IRIS2 (or High Power Target Lab, HPTL). From both stations, beams can either be delivered to low-energy beam lines or, after charge exchange, injected into the 25 MV tandem accelerator for post-acceleration (up to 5 MeV/u).

HRIBF mainly uses a plasma ion source (EBPIS) (see fig.2.2), but also the Kinetic Ejection Negative Ion Source (KENIS) (G. D. Alton, 2000) and surface ion sources. A facility for use of an online laser ion source is currently being installed at IRIS2.

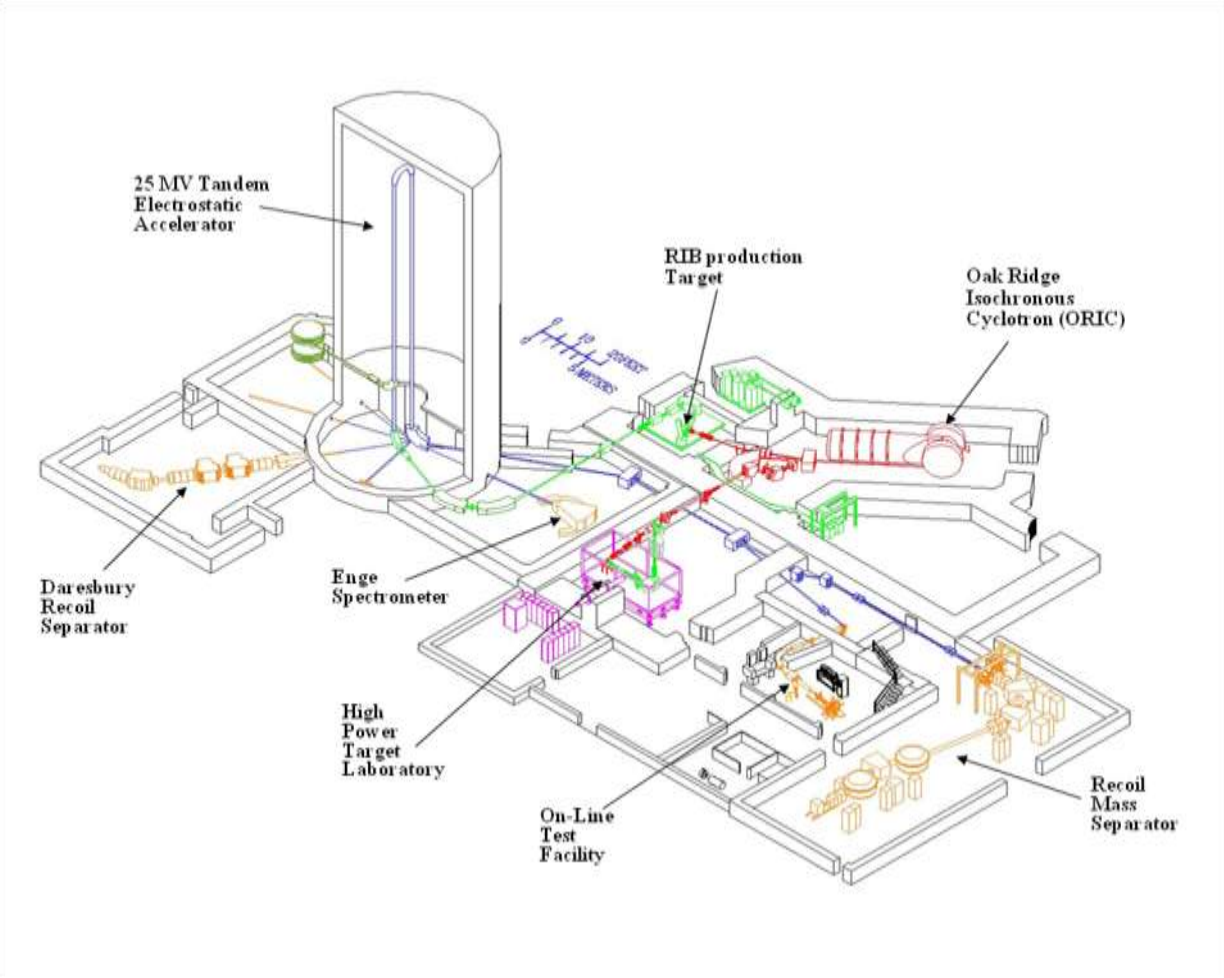

Fig. 2.11: Layout of the HRIBF at the ORNL

For developing and testing new methods online a small-scale version of the production platforms exists at HRIBF, the On-Line Test Facility (OLTF, a.k.a. UNISOR, see fig. 2.12, (Carter, 2008)). The target-ion source unit is identical to the one used for the main beam production and results are scalable. The primary beam is produced by the tandem accelerator. The OLTF can receive stable heavy ion beams and up to 50 nA of 40 MeV protons. The latter is an administrative limit leading to comparatively low radiation levels in the target-ion source area. Therefore the TIS unit becomes accessible very shortly after irradiation. This allows inspection and modification of the facility even after beam has been on target, a useful feature for development work. The OLTF is equipped with a separator magnet ($m/\Delta m=2{,}000$) and three beam lines. It

allows implantations, nuclear and atomic spectroscopy experiments and has a charge-exchange test station.

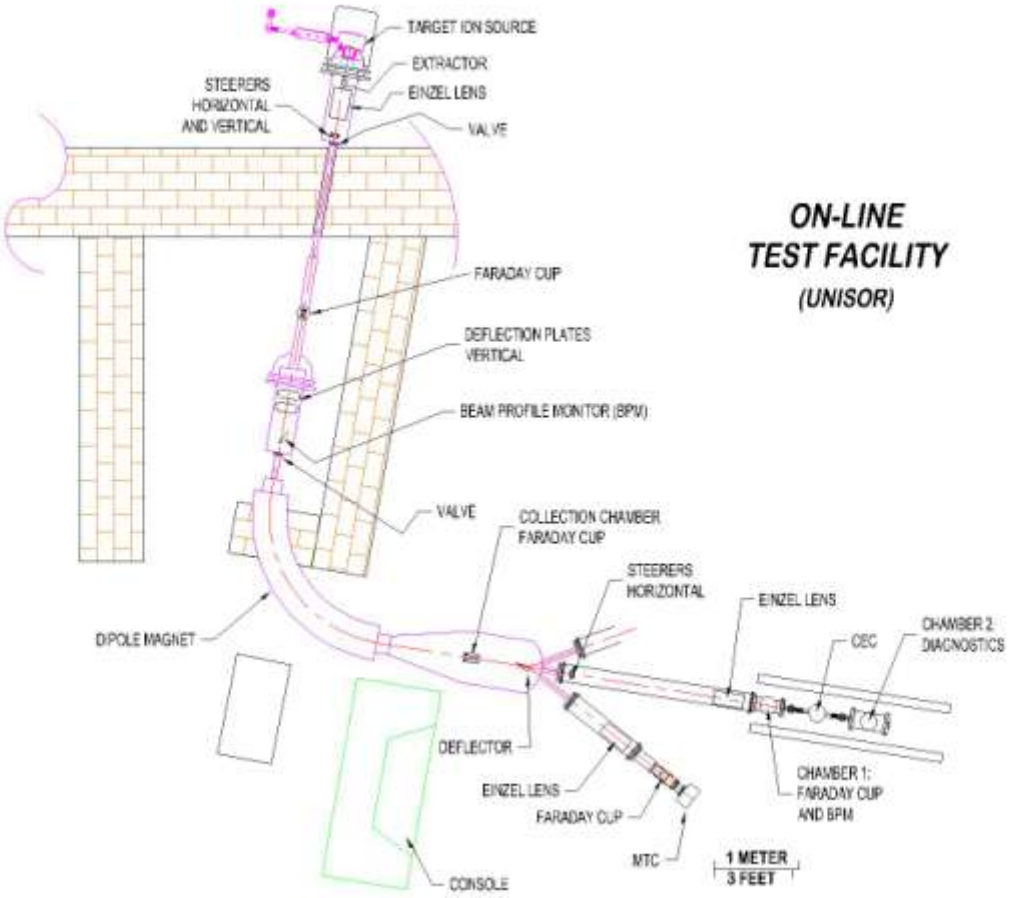

Fig. 2.12: Layout of the OLTF at the HRIBF

2.4 Adsorption

Adsorption processes play a crucial role in the transport of reaction products from the target to the ion source. In the strictest sense, adsorption is an accumulation of material on a surface, not involving the bulk of the adsorbing material. It can be differentiated between physisorption, also called Van der Waals adsorption, and chemisorption.

Physisorption describes attraction between atoms or molecules due to electrical dipole and quadrupole interaction. Enthalpies are in the range of -10 to -40 kJ/mol. Physisorption generally only exists close to the boiling point of the adsorbate and is usually quite unspecific.

Chemisorption describes a process caused by actual rearrangement of electrons; enthalpies are frequently larger than -80kJ/mol, sometimes as high as -400kJ/mol. It is not limited to temperatures close to the boiling point. In general, chemisorption is more selective than physisorption; however, it frequently is also irreversible (Thomas, 1997).

Most processes in the TIS will fall under these categories. In a few cases there might also be true absorption, involving diffusion into the bulk volume of a given material. This behavior will not appear very different from an irreversible adsorption process, though there will be no saturation of the surface.
The exact nature of the interaction will depend on the combination of adsorbate and adsorbent as well as their structure, temperature and the nature of the chemical atmosphere.

2.4.1 Ta

The “baseline” surface material that is used in standard TIS transfer lines is Ta metal. It is very refractory (melting point of 3017°C) making it a good material for the high temperature environment of the TIS. It has a body-centered cubic structure, with Ta-Ta distances of 286 pm. Under atmospheric conditions its surface is covered with a thin oxide layer that will be slowly removed by heating under vacuum. It is also reactive with sulfur and halogens at elevated temperatures.

2.4.2 Quartz glass

The first “trapping” material used in an ISOL transfer line was quartz glass. It has been used as early as 1973 (Rudstam, 1973) to remove alkali contaminations from ISOL beams. It was used again in 1984 for purification of neutron-rich Cd beams by Kratz et al. (Kratz, 1986) at the new ISOLDE and has been reintroduced as a standard method of beam purification in the last years (Bouquerel, 2008). Its application for various beams is still being investigated.

Quartz glass or fused silica (SiO_2), like crystalline quartz, consists of Si-O tetrahedra linked through their vertices. Unlike crystalline quartz it has a very low long-range order

(see fig. 2.13), creating an amorphous, and more porous, structure with larger distances between atoms: Si-Si: 320 pm, Si-O: 162 pm, O-O: 265 pm or 450 pm for atoms from adjacent tetrahedra. Its density is 2.2g/cm^3 as opposed to 2.6g/cm^3 for crystalline quartz (Inst., 1996).

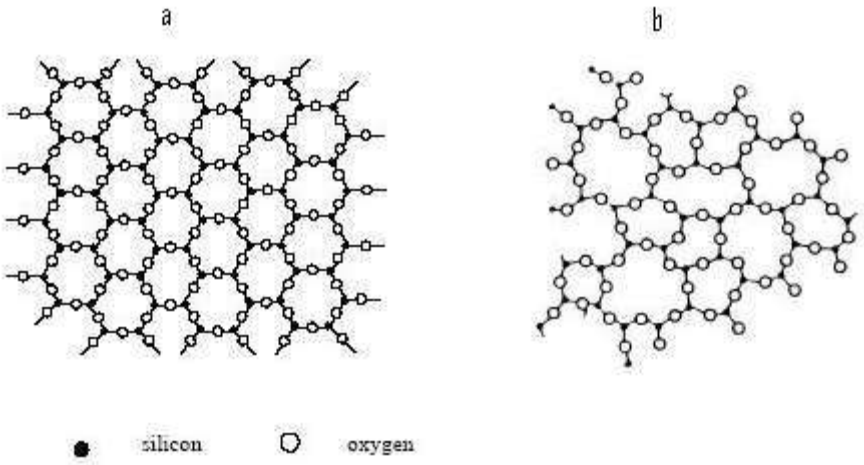

Fig. 2.13: 2D depiction of the structure of crystalline quartz (a) and fused silica (b)

Because of this reduced long-range order the structure contains a number of cavities or pores that can accommodate foreign atoms. In particular smaller alkali metals (Li, Na, K, Rb) are very likely to be absorbed by quartz glass since their small ionic radii allow fast diffusion into the bulk structure (see fig. 2.14, a). At elevated temperatures, the alkali metals will react with the SiO_2 lattice, breaking the Si-O bonds. This will open up pathways in the structure, leading to an even faster diffusion (Ingram, 1992).

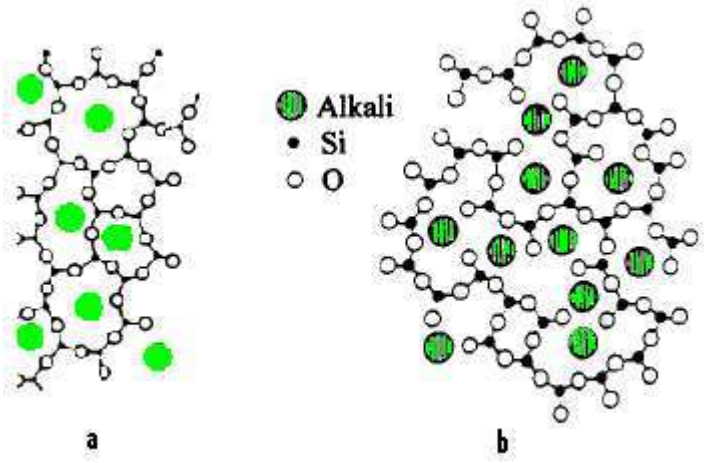

Fig. 2.14: Alkali atoms in a fused silica structure, before (a) and after annealing (b)

Because of its amorphous structure quartz glass does not have a specific melting point. The structure starts to weaken and deform at temperatures above 1200°C.
Under atmospheric conditions at room temperature, a silica surface will be partly hydroxylated; with different types of Si-OH species existing: isolated (a), geminal (b) or hydrogen-bonded (c) in fig. 2.15. The hydroxyl groups reduce the activity of the quartz surface by blocking active sites. When heated under vacuum below 730°C, the number of associated hydroxyl groups is reduced through elimination of water, leading to isolated hydroxyl groups. When heated above 730°C the isolated hydroxyl groups are eliminated as well, leading to strained Si-O-Si bridges on the surface. Due to these strained bonds the silica surface has more active sites for adsorption (Wovchko, 1995).

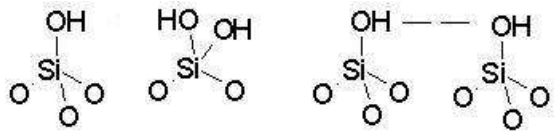

(a) (b) (c)

Fig. 2.15: Hydroxyl groups on silica surfaces

2.4.3 Sapphire

Another material that has been used in the transfer line is crystalline alumina (α-Al_2O_3) or corundum / sapphire. Unlike SiO_2 it is an ionic compound with the oxygen ions forming a hexagonal close-packed structure and aluminum ions occupying two thirds of the octahedral interstices. O-O distances are 250 pm, O-Al distances 199 pm and 185 pm respectively (Pauling, 1925). The density of sapphire is 3.95 g/cm^3, its melting point 2072°C. Under atmospheric conditions its surface is partially hydroxylated as well, although no literature data could be found on the loss of those groups when heating under vacuum.

2.5 Thermochromatography

Thermochromatography (TC) is a gas-phase adsorption chromatographic method often used to determine adsorption enthalpies of elements and their compounds on different surfaces. As in every chromatographic method an adsorbent (or stationary phase) is used to separate the constituents of a sample according to the strength of their interaction with this adsorbent, often employing a carrier medium to increase the speed

of the mobile phase. Samples usually contain radioactive tracers so that the deposition area of each element or compound can be determined by use of γ-detectors.

Isothermal TC uses a uniformly heated column. The detector is placed at the end of the tube to determine the retention times of the various sample constituents. Another method is the use of a negative temperature gradient along the chromatographic column. When the sample species go below the temperature zone where the energy needed for desorption from the surface is easily provided their retention time will increase considerably and the resulting peak is practically immobile. After a given experiment time the column is cooled down to freeze the achieved element distribution in place and the column is scanned in small sections. A plot of the relative intensities versus the distance from the temperature maximum will yield a thermochromatogram.

The method of TC has been successfully used to separate mixtures of radioactive samples for a long time. Amongst others it was employed by Marie and Pierre Curie after the discovery of the elements Po and Ra. Beginning in the 1970s the method was used to investigate the chemical properties of super-heavy elements, *e.g.* (Zvara, 1972). This initiated a rapid enhancement of both theory and practice of TC, led by groups in Dubna and at the Paul Scherrer Institute in Switzerland (Vertes, 2003). Another field of application was the rapid chemical separation of fission products for determination of fission yields as carried out at the TRIGA reactor in Mainz (Hickmann, 1993).

2.5.1 Theoretical description of TC

There are several models for the analysis of thermochromatographic data (Schaedel, 2003) to determine adsorption enthalpies and entropies.

The Thermodynamic Model assumes a simple adsorption-desorption equilibrium with no chemical reactions. In this case the following equation is valid:

$$\Delta G^0_{ads} = -RT \ln K = \Delta H^0_{ads} - T\Delta S^0_{ads} \qquad (2.15)$$

with ΔG^0_{ads} the free standard enthalpy of adsorption (J/mol); K the equilibrium constant of adsorption; ΔH^0_{ads} the standard adsorption enthalpy at zero surface coverage (J/mol) and ΔS^0_{ads} the standard entropy of adsorption at zero surface coverage (J/molK).

The basis of this model is the differential equation for the transport velocity of a substance in the ideal linear gas chromatography (Schaedel, 2003):

$$\frac{dy}{dt} = \frac{u}{1+k_i} \tag{2.16}$$

with y the coordinate longitudinal to the column and u the carrier gas velocity; the corrected partition coefficient $k_i = \frac{s}{v} K_{ads}$ with K_{ads} being the distribution constant.

$\frac{s}{v}$ corresponds to the ratio of solid and gaseous phase, with s being the inner surface area of the column per 1m length, v the gaseous volume per 1m length.

For the formulation of a dimensionless adsorption equilibrium constant the definition of a standard state is crucial. The standard state can be freely chosen, regardless of its physical realization. The standard state of adsorption is assumed to be the ratio of a standard molar volume to the standard molar surface (Eichler, 1982):

$$\frac{V}{A} = \frac{c^0_{ads}}{c^0_{gas}} = 1cm \rightarrow \frac{V}{100A} = \frac{c^0_{ads}}{c^0_{gas}} = 1m \tag{2.17}$$

$$K = K_{ads}\frac{100A}{V} = \frac{c_{ads}}{c_{gas}}\frac{c^0_{ads}}{c^0_{gas}} \tag{2.18}$$

where V is the inner volume of column (m^3); A the inner surface of column per 1m length (m^2); c^0_{ads} the standard surface concentration of the adsorbate, 2.679*10^{25} per m^3 (ideal gas at STP); c^0_{gas} the standard gas concentration of the adsorbate, 2.679*10^{25} per m^3 (ideal gas at STP); c_{ads} the surface concentration of the adsorbate (particles/m^3); c_{gas} the gas concentration of the adsorbate (particles/m^3).
Including the concentration of adsorption sites and a reversible change of chemical state (Eichler, 1982), eq. (2.15) can be written as:

$$\Delta G^0_{r,ads} = -RT\ lnK = (\Delta H^0_r + \Delta H^0_{ads}) - T(\Delta S^0_r + \Delta S^0_{ads}) \tag{2.19}$$

with $\Delta G^0_{r,ads}$ being the free standard adsorption enthalpy with chemical reaction (J/mol); ΔH^0_r the standard reaction enthalpy (J/mol); ΔS^0_r the standard reaction entropy (J/mol K).

The entropy of a mobile adsorption process can be described by another model. It is based on the assumption that during the adsorption process a species in the gas phase, where it has three degrees of freedom (translation) is transferred into the adsorbed state with two translational degrees of freedom parallel to the surface and one vibrational degree of freedom vertical to the surface. From statistical thermodynamics the following equation for the calculation of the adsorption entropy is derived (Schaedel, 2003):

$$\Delta S^0_{ads} = R\left(\ln\left(\frac{100A}{Vv_b}\right)\sqrt{\frac{RT}{2\pi M_a}} + \frac{1}{2}\right) \quad (2.20)$$

M_a: molar weight of adsorbate (kg/mol)
For gas thermochromatography (TC with temperature gradient) a linear temperature gradient is assumed:

$$T = T_s - a\,y \quad (2.21)$$

with T_s being the starting temperature of gradient (K); a, a negative temperature gradient (K/m).

Substitution of the corrected partition coefficient and introduction of the standard state (eq. 2.20) lead to:

$$t_r = -\frac{1}{a}\int_{T_s}^{T_{dep}} \frac{\left(1 + \frac{s}{V}\frac{V}{100\,A}K(T)\right)}{u(T)}\,dT \quad (2.22)$$

with t_r the retention time (s); T_{dep} the deposition temperature (K);

Substituting $u(T) = \frac{u_0 T}{T_0}$ and $\bar{V}_0 = u_0 O$

with u_0: gas velocity at STP (m/s); T_0: standard temperature, 298.16K; $\bar{V}$: carrier gas flow, (m^3/s); O: free open cross section area of the column (m^2); $\bar{V}_0$: carrier gas flow at STP (m^3/s),

integration yields:

$$t_r = -\frac{T_0}{a * u_0}\ln\left(\frac{T_{dep}}{T_s}\right) + \frac{sOT_0\frac{V}{100A}\exp\left(\frac{\Delta S^0_{ads}}{R}\right)}{\bar{V}_0 av}\left[Ei'\left(-\frac{\Delta H^0_{ads}}{RT_{dep}}\right) - Ei'\left(-\frac{\Delta H^0_{ads}}{RT_s}\right)\right] \quad (2.23)$$

Ei*(x) is the exponential integral function of x. For x»1 this function is approximated by:

$$Ei^*(x) = \frac{\exp(x)}{x} \quad (2.24)$$

Since in most cases $T_{dep} \ll T_s$ and $Ei'\left(-\frac{\Delta H^0_{ads}}{RT_{dep}}\right) \gg Ei'\left(-\frac{\Delta H^0_{ads}}{RT_s}\right)$, eq. (2.23) can be written as follows (Schaedel, 2003):

$$\frac{a t_r \bar{V}_0}{sT_{dep}\frac{V}{100A}} = \left(\frac{RT_0}{-\Delta H^0_{ads}}\right)\exp\left(-\frac{\Delta H^0_{ads}}{RT_{dep}}\right)\exp\left(\frac{\Delta S^0_{ads}}{R}\right) \quad (2.25)$$

This equation connects the deposition temperature with the thermodynamic state function of adsorption, so one can be determined if the other is known. In this equation the retention time t_r equals the half-life for short-lived nuclides or the duration of the experiment for long-lived nuclides.

The Kinetic Model (Schaedel, 2003) describes the adsorption-desorption processes of a single atom, on the basis of microscopic rather than macroscopic properties.
To determine the adsorption enthalpy of a given adsorbate on a surface, experimental parameters and physical properties are fed into the model. An assumed value of enthalpy yields, by way of a Monte Carlo simulation (see below), a theoretical chromatogram that is checked against experimental results. The ΔH_{ads} value is obtained from the best agreement between model and experiment.

A Monte Carlo simulation is a method in which random numbers are employed to simulate statistical processes. In these simulations random numbers between 0 and 1 are used to simulate several parameters:

a) life time of radio nuclide: $t_\lambda = \frac{\ln 2}{T_{1/2}} \ln(1 - \text{random})$ (2.26)

with t_λ: life time (s); $T_{1/2}$: half life (s); random: random number 0 ≤ x < 1

b) mean free path and time of flight in the gas phase: The mean free path of the adsorbate is approximately:

$$Y_{jm} = \frac{11\bar{v}(p,T)}{48\pi D(p,T)} \quad (2.27)$$

with Y_{jm}: mean free path of the adsorbate (m); D: diffusion coefficient of adsorbate in carrier gas (m^2/s).
The pressure- and temperature-dependent diffusion coefficient D can be described (Gilliland, 1934) as follows:

$$D = 0.01378 * 10^{-7} (T_0)^{1,5} \sqrt{\frac{1}{M_g} + \frac{1}{M_a}} p^{-1} \left(\sqrt[3]{\frac{d_g}{M_g}} + \sqrt[3]{\frac{d_a}{M_a}} \right)^{-2} \left(\frac{T}{T_0} \right)^{1,75} \quad (2.28)$$

with M_a and M_g : molar mass of adsorbate and carrier gas (kg/mol) respectively; p: pressure (Pa); d_a and d_g: density of adsorbate and carrier gas at melting point (kg/m^2) respectively.

The gas flow is pressure- and temperature-dependent as well and can be described, under the assumption of ideal behavior:

$$\bar{V}(p,T) = \bar{V}_0 \frac{TP_0}{T_0 p} \quad (2.29)$$

with P_0: standard pressure, 101325 Pa

The mean free path is used to determine the random free path of a particle according to a logarithmic distribution:

$$y_j = -Y_{jm} \ln(1 - random) \quad (2.30)$$

with y_i: random free path (m).
This yields the time the atom spends in flight:

$$t_j = \frac{y_j \pi d_i^2}{4\bar{V}(p,T)} \quad (2.31)$$

with t_j: transport time (s); d_i: inner diameter of column (m).

c) residence time on surface: the average number of wall collisions during $Y_{j,m}$ is:

$$N_m = Y_{jm} \frac{d_i}{2\bar{V}(p,T)} \sqrt{\frac{2\pi RT}{M_a}} \quad (2.32)$$

From this we obtain for the random number of wall collisions N_a:

$$N_a = -N_m \ln(1 - random) \quad (2.33)$$

and the average residence time on the surface from a Frenkel type equation:

$$t_{am} = \frac{1}{v_b} \exp\left(-\frac{\Delta H^0_{ads}}{RT}\right) \quad (2.34)$$

with v_b: phonon frequency of adsorber material (s^{-1}).

Finally we can determine the random residence time with:

$$t_a = -N_a \, t_{am} \ln(1 - random) \quad (2.35)$$

By simulating the diffusion paths of a large number of particles the statistical distribution of a thermochromatographic experiment can be obtained.

2.6 Nuclear Structure

2.6.1 Beta decay

Beta decay is a radioactive decay mode of nuclei by which a nucleus made of Z protons and N neutrons decays to a nucleus of the same nucleon number A but with (Z±1, N±1). A beta particle, either an electron or a positron, and a neutrino are ejected by the nucleus. They are generated by the decay of a W boson produced in the conversion of a neutron to a proton or vice versa (see fig 2.16).

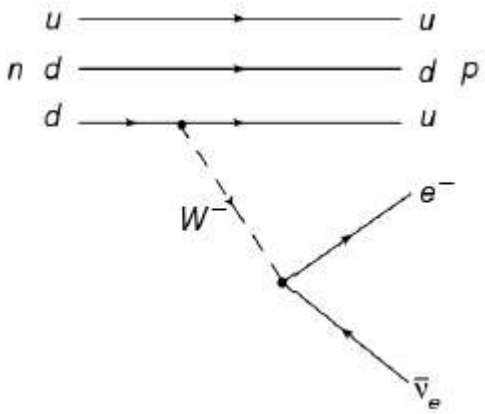

Fig. 2.16: Transformation of a neutron into a proton by emission of a W^- boson

There are 3 different known modes of beta decay which can be distinguished by the particles emitted in the decay: In a β^--decay, an electron and an anti electron neutrino are emitted, in a β^+-decay a positron and an electron neutrino. The third mode is electron capture, in which an electron from a low-lying shell is transferred into the nucleus to change a proton into a neutron.
The energy released by beta decays is distributed over the emitted particles. Therefore beta spectra have a continuous energy distribution. Extrapolation of the energy curve to zero yields the maximum energy, called the Q_β value.

2.6.1.1 Fermi theory

The probability of an electron to be emitted in the momentum interval p to p+dp can be described by Fermi's "Golden Rule":

$$N(p_e)\mathrm{d}p_e = \frac{2\pi}{\hbar}\left|\left\langle \Psi_f \middle| \hat{\mathrm{H}} \middle| \Psi_i \right\rangle\right|^2 \frac{\mathrm{d}n}{\mathrm{d}E_0} \qquad (2.36)$$

The matrix element with the Hamiltonian and wave functions for the initial and final state contains the nuclear matrix element **M** which describes the transition probability and is correlated with the beta half-life of the nucleus.

$$\left|\left\langle \Psi_f \left| \widehat{\mathrm{H}} \right| \Psi_i \right\rangle\right|^2 = \left|\widehat{\mathrm{H}}_{f\to i}\right|^2 = \left[g\left|\psi_e(0)\right\|\psi_{\bar{\nu}}(0)\right\|\mathbf{M}\right|]^2 \qquad (2.37)$$

$\left[\left|\psi_e(0)\right\|\psi_{\bar{\nu}}(0)\right|]^2$ describes the probability of the beta particle and neutrino being in the nucleus at the time of their creation (t=0). Since this probability is very close to unity, eq. 2.37 can be simplified thus:

$$\left|\widehat{\mathrm{H}}_{f\to i}\right|^2 = g^2\mathbf{M}^2 \qquad (2.38)$$

There are two possible matrix elements **M**, one each for Gamow-Teller and Fermi transitions (see chapter 2.6.1.2):

$$\left|\widehat{\mathrm{H}}_{f\to i}\right|^2 = g_V^2\mathbf{M}_F^2 + g_A^2\mathbf{M}_{GT}^2 \qquad (2.39)$$

with $\mathbf{M}_F = \int g_V\left(\overline{\Psi}_p 1 \Psi_n\right)\mathrm{d}\tau$ (2.40)

and $\mathbf{M}_{GT} = \int g_A\left(\overline{\Psi}_p \vec{\sigma} \Psi_n\right)\mathrm{d}\tau$ (2.41)

Assuming $\mathbf{M}_{GT}$ and $\mathbf{M}_F$ to be constant, the shape of the electron spectra is determined only by the statistical factor $\mathrm{d}n/\mathrm{d}E_0$.

With $\mathrm{d}n = p^2\,\mathrm{d}p\,\frac{1}{2\pi^2\hbar^3}$ (2.42)

it follows for the probability for a simultaneous transition of electron and neutrino:

$$\frac{\mathrm{d}n}{\mathrm{d}E_0} = \frac{\mathrm{d}n_\nu \cdot \mathrm{d}n_e}{\mathrm{d}E_0} = \left(p_e^2\,\mathrm{d}p_e\right)\left(p_\nu^2\,\mathrm{d}p_\nu\right)\frac{1}{4\pi^4\hbar^6}\frac{1}{\mathrm{d}E_0} \qquad (2.43)$$

With $p_\nu = \frac{E_0 - E}{c}$ for the neutrino momentum and $\frac{\mathrm{d}p_\nu}{\mathrm{d}E_0} = \frac{1}{c}$, eq. 2.43 yields:

$$\frac{\mathrm{d}n}{\mathrm{d}E_0} = p_e^2\left(E_0 - E\right)^2\,\mathrm{d}p_e\,\frac{1}{4\pi^4\hbar^6c^3}\frac{1}{\mathrm{d}E_0} \qquad (2.44)$$

Substitution in eq. 2.36 leads to the following equation for the momentum spectrum:

$$N(p)\mathrm{d}p = \frac{g_V^2\mathbf{M}_F^2 + g_A^2\mathbf{M}_{GT}^2}{2\pi^3\hbar^7c^3}\,p^2\left(E_0 - E\right)^2\,\mathrm{d}p \qquad (2.45)$$

Actual electron spectra will deviate from this function since they are deformed by Coulomb forces; electrons must overcome the attraction of the protons while positrons are repelled. The Fermi function $f_{Z,p}$ corrects for these effects:

$$N(p)\mathrm{d}p = \frac{g_V^2\mathbf{M}_F^2 + g_A^2\mathbf{M}_{GT}^2}{2\pi^3\hbar^7c^3}\mathrm{f}(Z,p)p^2(E_0 - E)^2\,\mathrm{d}p \qquad (2.46)$$

Integration over momentum and substituting the Fermi function yields the total decay constant λ:

$$\lambda = \int_0^{p_0} \mathrm{N}(p)\mathrm{d}p = \frac{\ln 2}{t_{1/2}} \qquad (2.47)$$

Multiplication of $f_{Z,p}$ and the half-life leads to the "log ft" value:

$$\mathrm{f}(Z,E)t_{1/2} = \frac{2\pi^2\hbar^7c^3\ln 2}{g_V^2\mathbf{M}_F^2 + g_A^2\mathbf{M}_{GT}^2} = \frac{2\pi^2\hbar^7c^3\ln 2}{\left|\mathbf{M}_{fi}\right|^2} \qquad (2.48)$$

with the matrix element $\left|\mathbf{M}_{fi}\right|^2$ defining the "beta strength function":

$$S_\beta(E) = \left|\mathbf{M}_{fi}\right|^2 = \frac{2\pi^2\hbar^7c^3}{\mathrm{f}(Z,E)t_{1/2}} \qquad (2.49)$$

The log ft value is a direct measure of the matrix elements M_F and M_{GT} and their coupling constants and therefore also for the transition probability of a beta decay (see table 2.1).

Table 2.1: Beta decay types and their log ft values

Beta decay type	ΔI	Parity	Log ft
Super allowed	0 ±1	+	2,7 – 3,7
allowed	0 ±1	+	4 – 6
First forbidden	0 ±1	-	6 – 10
First forbidden ("unique")	±2	-	7 – 10
Second forbidden	±2	+	11 - 14
Third forbidden	±3	-	17 – 19
Fourth forbidden	±4	+	≈ 19

2.6.1.2 Fermi and Gamow-Teller transitions

The nuclear matrix elements M_F and M_{GT} describe two different modes of beta decays, Fermi transitions and Gamow-Teller transitions. If the spins of the decaying neutron and created proton are parallel, the transition is a Fermi transition:

$$n(\uparrow) \rightarrow p(\uparrow) + e^{-}(\uparrow) + \bar{\nu}_e(\downarrow) \qquad (2.50)$$

It follows the selection rule ΔI=0 and Δπ=0.
In a Gamow-Teller transition:

$$n(\uparrow) \rightarrow p(\downarrow) + e^{-}(\uparrow) + \bar{\nu}_e(\uparrow) \qquad (2.51)$$

and ΔI = 0, 1 und Δπ = 0. Gamow-Teller transitions are frequently observed in the decay of very neutron rich nuclei.

2.6.2 γ-decay

Gamma rays are electromagnetic waves that are emitted from an excited nucleus when dropping to a lower-lying energy state:

$E_\gamma = h\nu = E_i - E_f \qquad (2.52)$

Therefore the energy of the gamma ray corresponds to the difference in energy of the nuclear levels and is characteristic for a given decay.
Gamma rays are also created in annihilation processes.

2.6.2.1 Order of multipoles

Classical electrodynamics describes a radiation source as oscillating electric or magnetic moments. The charge or current distribution is described by spherical functions of the order ℓ = 1,2,… Thus the moments and the resulting radiation are called dipole, quadrupole, octupole etc.
Quantum mechanics analogously classifies radiation by the angular momentum it carries:
ℓ = 1 Dipole (e.g. $1^+ \rightarrow 0^+$)
ℓ = 2 Quadrupole (e.g. $2^+ \rightarrow 0^+$)
ℓ = 3 Octupole (e.g. $3^+ \rightarrow 0^+$)

2.6.2.2 Electric and magnetic multipoles

For each order ℓ there is both electric and magnetic multipole radiation with opposite parity:

$\pi = (-1)^{\ell}$ electric multipole radiation

$\pi = (-1)^{\ell+1}$ magnetic multipole radiation

The usual denotation is “Eℓ” for electric multipole radiation and “Mℓ” for magnetic multipole radiation. Therefore multipole radiation of even parity will be described as M1, E2, M3,…; multipoles of odd parity are E1, M2, E3,…
Usually only the lowest allowed order of each multipole radiation has a marked effect on transition probabilities.

2.6.3 Nuclear structure models

In trying to understand nuclear structure, models have been designed to recreate known nuclear properties and predict properties of exotic nuclei like half-life, neutron separation energy or reaction cross sections. As of now, because of the complex interactions of nucleons, no comprehensive model exists for nuclear structure; a number of different models are used for different problems. Some of these models are described below.

2.6.3.1 The shell model

A simple microscopic model is the shell model. It assumes that fermions can move inside a potential well without mutual interaction. The potential is created by the nucleons and, in first approximation, is spherically symmetric. The shape of the potential can be described by the Woods-Saxon potential, a combination of the harmonic oscillator and the infinite well potential (see fig. 2.17):

$$V(r) = -\frac{V_0}{1 - e^{\frac{r-R}{a}}} \qquad (2.53)$$

with V_0 the constant potential inside the nucleus, R the mean radius (where the potential has dropped to half its original value) and a the “skin thickness”.

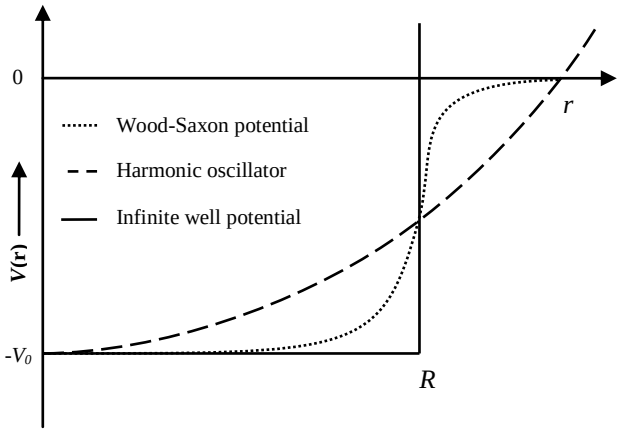

Fig. 2.17: Different potential gradients to describe the nuclear potential

From this potential, energy levels can be calculated and filled with nucleons according to their degree of degeneracy and the Pauli principle. Since the resulting shell structure does not correspond to the “magic numbers” observed in nuclei, the potential must be modified by the addition of terms.

Due to their different charge states neutrons and protons experience different potentials in the nucleus. The potential well for neutrons is deeper than that for protons which create an additional Coulomb potential (see fig. 2.18).
Applying this basic idea to the three-dimensional potential well and solving the Schroedinger equation results in energy levels $E_{n,l}$ depending on the radial quantum number n and the angular momentum l. Each level is 2(2l+1)-fold degenerate.

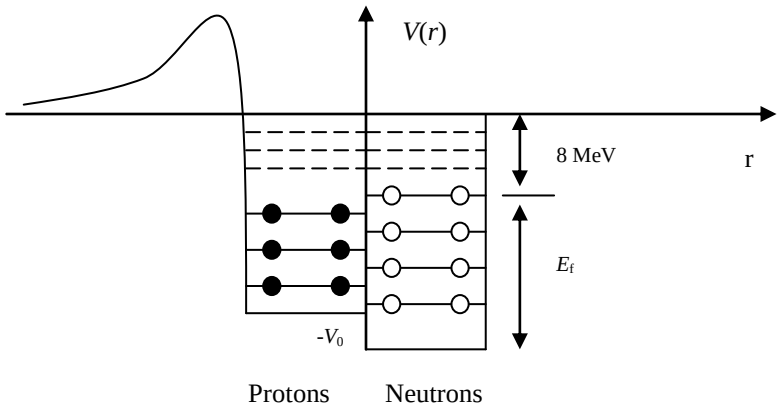

Fig. 2.18: Depth of potential well for protons and neutrons

There is also an interaction of the spin s and the angular momentum l as is known from atomic physics but has a much greater effect in nuclear physics. The modified potential can be written as follows:

$$V_i = V(r) + V_{ls}(r)\left(\vec{l}\cdot\vec{s}\right) \tag{2.54}$$

For the determination of $\langle \vec{l}\cdot\vec{s} \rangle$, $\vec{j} = \vec{l} + \vec{s}$ must be squared:

$$\left\langle \vec{l}\cdot\vec{s} \right\rangle = \frac{1}{2}\left(\left\langle j^2 \right\rangle - \left\langle l^2 \right\rangle - \left\langle s^2 \right\rangle \right) = \frac{1}{2}\left(j(j+1) - l(l+1) - \frac{3}{4} \right) \tag{2.55}$$

With $s = \pm ½$ it follows:

$$\vec{j} = \vec{l} \pm \frac{1}{2} \tag{2.56}$$

and the expectation value $\langle \vec{l}\cdot\vec{s} \rangle$ becomes:

$$\left\langle \vec{l}\cdot\vec{s} \right\rangle = \frac{1}{2} l \tag{2.57}$$

for $s = ½$ and

$$\left\langle \vec{l} \cdot \vec{s} \right\rangle = -\frac{1}{2}(l+1) \qquad (2.58)$$

for $s = -½$ (2.59)

The difference in potential energy for the different spins then is:

$$\Delta E = \frac{1}{2} V_{ls}(2l+1) \qquad (2.60)$$

Thus the spin-orbit coupling leads to an energy splitting of each level proportional to the angular momentum l.

Through the addition of these and other modifications to the nuclear potential the shell model can be made to closely approach observed nuclear properties near the line of beta stability.

2.6.3.2 Current models

Models currently used in nuclear astrophysics are mostly combinations of macroscopic and microscopic approaches.

One of these is the *Q*uasi Particle *R*andom *P*hase *A*pproximation (QRPA) model which is based on a microscopic spherical one-particle model and taking into account pair interaction and residual Gamow-Teller interaction. It employs different forms of nuclear potentials, e.g. Woods-Saxon or Folded-Yukawa and is quite successful in describing the majority of nuclear properties.

Other models using the macroscopic-microscopic approach are the *F*inite *R*ange *D*roplet *Model* (FRDM) or the *E*xtended *T*homas *F*ermi plus *S*trutinski *I*ntegral – *Q*uenched (ETFSI-Q) model.

3 METHODS

3.1 Thermochromatography

TC is a powerful means for investigating transport phenomena in the transfer line. It provides precise adsorption enthalpies and models allow simulation of transport rates under different conditions (flow rates / pressure, temperature). Thus we can learn about the process of adsorption while excluding influences of ion source or target parameters.

3.1.1 Experimental procedures at CERN

The TC experiments performed at ISOLDE were designed as gas TC, using an Ar inert gas flow to introduce a preferred direction of travel for the sample. The Ar was run though a dry-ice trap and a Ti getter oven for purification before entering the TC column (see fig 3.1).

The oven was a 10-zone gradient oven with a maximum temperature of 1200°C (see fig. 3.2). The zones can be controlled separately to introduce user-defined temperature gradients along the heated length (1m). For these experiments the gradient was set up to decrease from 1200°C to room temperature. The adsorption surface used for the experiments was quartz glass. Sample elements were Cs, Cd, Ag, In, Rb and Zn implanted on Ta foils. The inert gas flow was varied from 20 to 100 cm^3/min.

More detailed description of the set-up and experimental conditions can be found in (Jost, 2005).

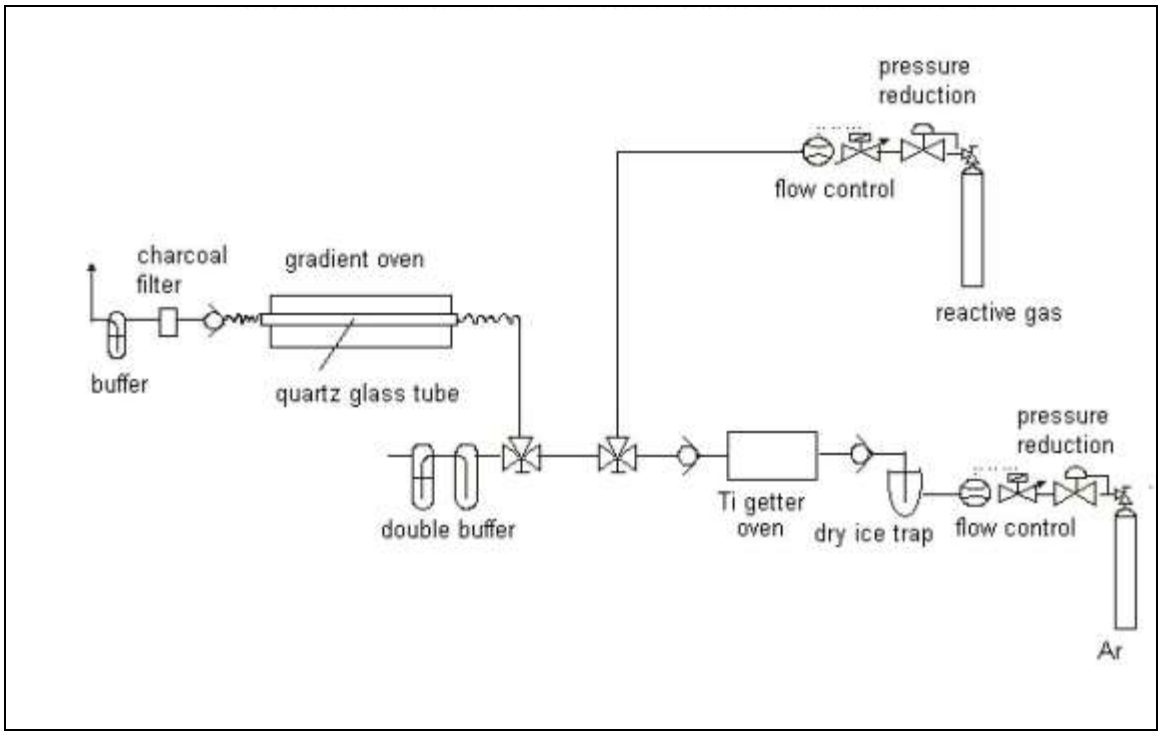

Fig. 3.1: Schematic of TC experiment setup

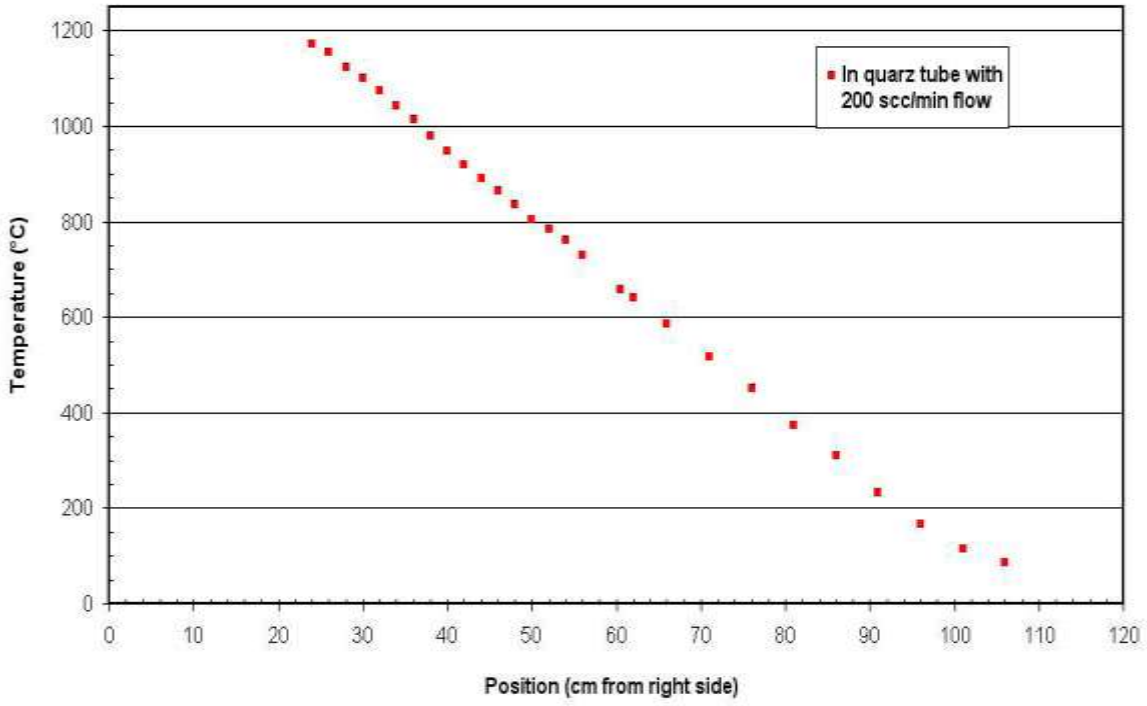

Fig 3.2: Temperature gradient of ISOLDE 10-zone oven

3.1.2 Experimental procedures at TRIGA Mainz

The experimental arrangement assembled at the TRIGA reactor Mainz (Eberhart, 2000) was also designed for gas TC and thus features the same purification devices for the inert gas flow as at CERN (see fig 3.1). In some of the experiments, unpurified He (with O_2, H_2O contaminants) or a He / H_2 mixture was used.

The oven was designed to reach temperatures up to 1700°C to allow for testing of materials other than quartz glass. The heated length is 80 cm, which leads to a steeper temperature gradient (see fig. 3.3). This in turn allows a more precise determination of adsorption enthalpies. Unlike the one used at ISOLDE this oven does not have separately controlled zones but a temperature gradient dependent on the set maximum temperature.

The adsorption surface used was quartz glass. The sample elements were Cs, Cd, K and Ag. Salts of these elements were activated at the TRIGA reactor at the Institute for Nuclear Chemistry, Mainz. The activated samples were transferred on Ta foils and placed at the temperature maximum of the column.

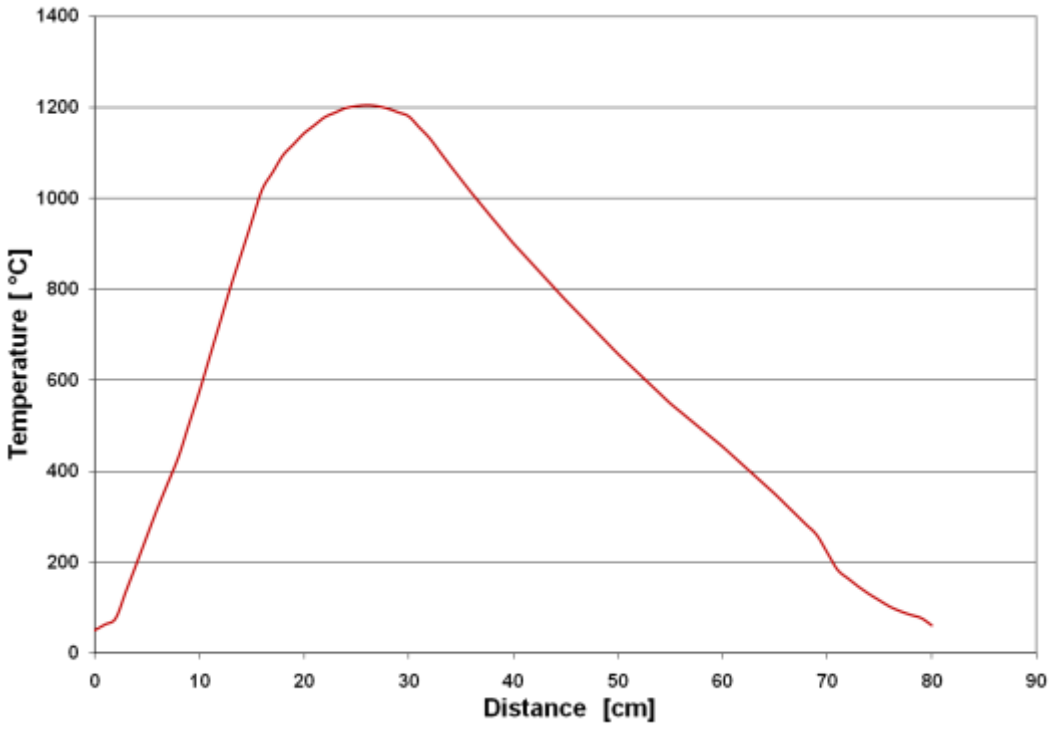

Fig. 3.3: Temperature gradient of the Mainz TC oven

3.1.3 Analysis

After a one-hour experiment time the columns were cooled down rapidly to “freeze” the distribution of elements. Then the activity in the column was measured with a γ-detector in small increments, using a collimator of 2 cm width (see fig. 3.4). Analysis was done using the program Genie2000.

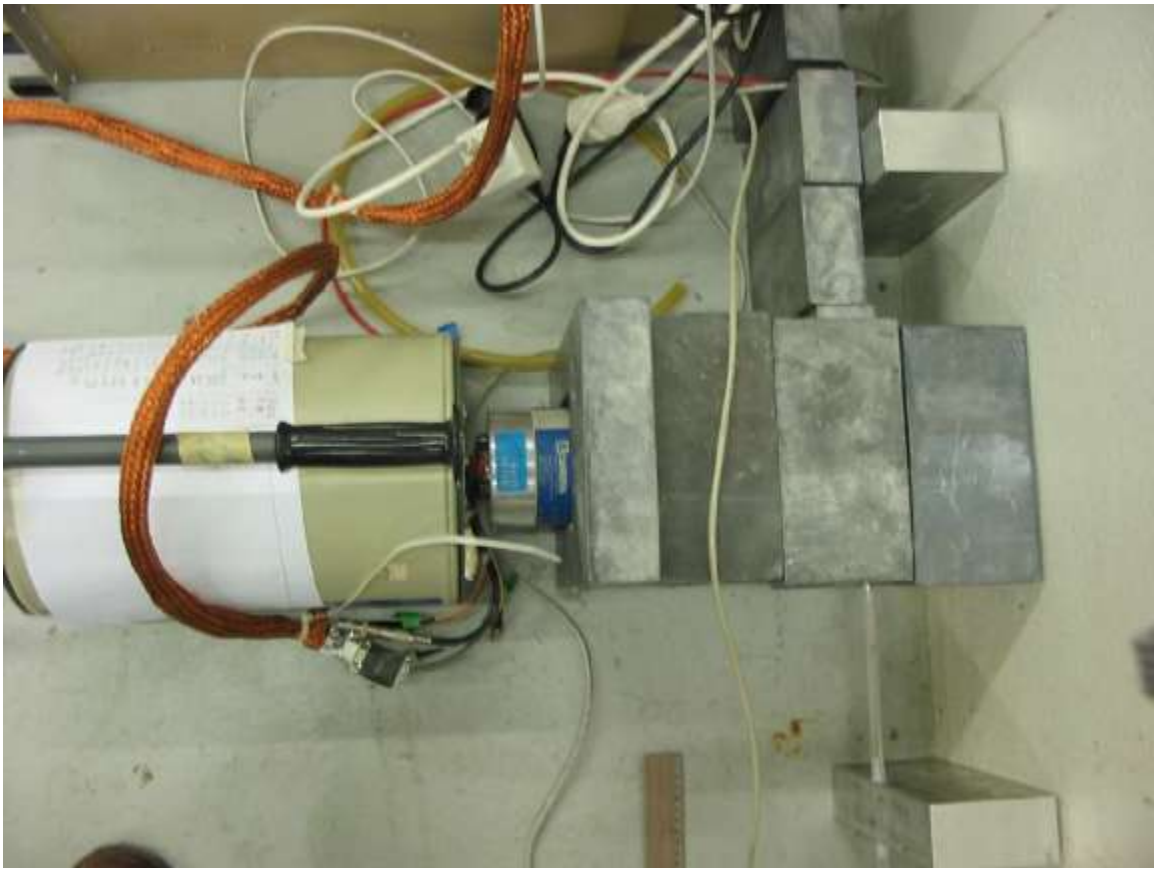

Fig. 3.4: γ-setup with 2cm collimator (not visible) and quartz tube

3.1.4 Adsorption enthalpies

The deposition peaks obtained by plotting the relative activity against the temperature gradient were fitted to a Gaussian function with Origin7.5 to determine the temperature at the deposition maximum. These temperatures were fed into the Mobile Adsorption code by Eichler (Schaedel, 2003) to determine the adsorption enthalpies.

3.2 On-line experiments

All on-line experiments were conducted at the Online Test Facility (OLTF) (Carter 2008) at the Holifield Radioactive Ion Beam Facility, ORNL (see chapter 2.3.2). All nuclides used and the experiments done with them are given in table 3.1.

The primary beam was delivered by the tandem accelerator, using a maximum of 50nA of 40MeV protons and 15-27nA of low-energy stable beams. Energies and intensities for protons and stable heavy ion beams used for hold-up time measurements are given in table 3.2, as well as charge states after stripping. Energies for the heavy ion beams were kept well below the Coulomb barrier so as not to cause any nuclear reactions.

Table 3.1: List of all nuclides used in thesis experiments

Element	Nuclides	Exp.	Element	Nuclide	Exp.
Zn	77g, 77m, 78, 80	Yields	Cd	119g, 119m, 121g, 121m, 123g, 123m, 124, 125g, 125m, 126, 127, 129	Yields
Ga	77-81	Yields	In	120g, 120m, 120m2, 121g, 121m, 122g, 122m, 122m2, 123g, 123m, 124g, 124m, 125g, 125m, 126, 127g, 127m 115	Yields Hold-up
Ge	77m, 79g, 79m, 80, 81g, 81m	Yields	Sn	123m, 124, 125g, 125m 120	Yields Hold-up
Br	88,89, 91 79	Yields Hold-up	I	138, 139	Yields
Kr	89, 91-95 89, 90	Yields Hold-up	Xe	138-142	Yields
Rb	89, 90g, 90m, 91-95 89	Yields Hold-up	Cs	138g, 138m, 139, 140, 141, 142	Yields
Sr	91-95	Yields			
Ag	116g, 166m, 117g, 117m, 119, 120g, 120m 107	Yields Hold-up			

Table 3.2: Energies, charge states and max. current on target for tandem beams used

Beam	Energy (MeV)	Charge state	Max. current (nA)
p	40	+1	50
^{107}Ag	220	+13	19
^{115}In	223	+13	27
^{79}Br	200	+12	15

3.2.1 Oak Ridge TIS

Ion source

The ion source used for these experiments was constructed like a standard Oak Ridge Electron Beam Plasma Ion Source (EBPIS) (Carter 1997). Cathode currents applied were in the range of 335 to 355 A, generating anode currents of 150 to 160 mA, with the anode kept at +150 V. Stable noble gas efficiencies were generally slightly lower than the average extracted from EBPIS sources, about 7% for Kr and 10% for Xe.

Transfer line

All yield measurements discussed were performed using the modified TIS with a variable-temperature transfer line (see fig. 3.5). It is based on the prototype #1 designed at ISOLDE (Bouquerel, 2007) and was modified for the Oak Ridge TIS and to allow the exchange of adsorption materials. The transfer-line is angled to avoid a direct view of the heat radiation from the ion source and to create a greater distance between target and ion source (~2100° C). Four discs of tantalum (Fig. 3.5, 2) are attached to the line above the target to dissipate heat transferred from the target. Also, the ion source's cathode current feed (Fig. 3.5, 8) is connected at the end of the transfer-line to avoid the heating effect of this current. Adsorption materials in the shape of a tube are placed in the horizontal part of the transfer-line (Fig. 3.5, 6). An opening in the line (Fig. 3.5, 3) allows for changes of tubes, thus keeping the production system identical in all parameters but the adsorption surface.

An additional heating system is attached to the section of the transfer-line containing the adsorption material (Fig. 3.5, 6), to permit investigation of temperature dependence of the adsorption effects. The heater consists of Ta wire (Ø: 1mm) in alumina insulator tubes. Three type B thermo-couples (Fig. 3.5, 13) are permanently attached to the transfer line to determine the temperature gradient along the line. The lowest line temperature possible with this setup was measured to be 780° C at thermocouple position 2. The maximum temperature applied (due to the melting point of fused silica) was 1140° C. This required the transfer line heater to be run with a current of 10.5 A, which corresponds to 55 W. Temperature gradients of the line are shown in figure 3.6. For all experiments conducted with this TIS, the "low temperature" setting (LT) refers to no additional heating current while the "high temperature" setting (HT) refers to the maximum heater current.

Target and transfer-line are kept in place by an insulating support (Fig. 3.5, 5). A gas feed line (Fig. 3.1, 7), to introduce stable Kr / Xe into the system is connected at the end of the transfer-line. The connection to the ion source (cathode, Fig. 3.5, 10; anode, Fig. 3.5, 11; anode wire, Fig. 3.5, 12) is made by a piece of molybdenum tubing (Fig. 3.5, 9) to allow separation of transfer-line and ion source even after extensive heating.

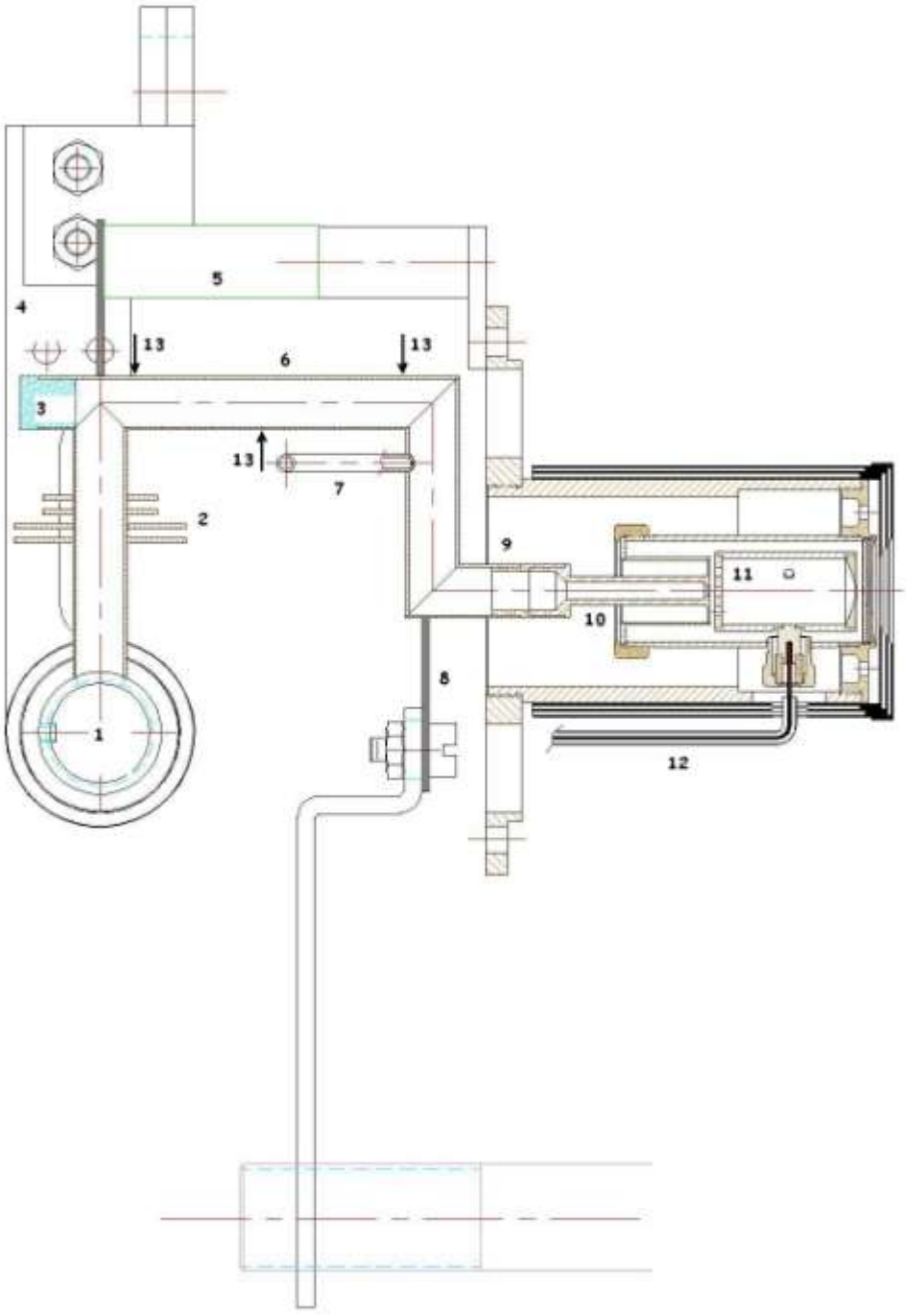

Fig. 3.5: Modified target ion source used for selective adsorption tests. In the text, reference is made to the numbered parts.

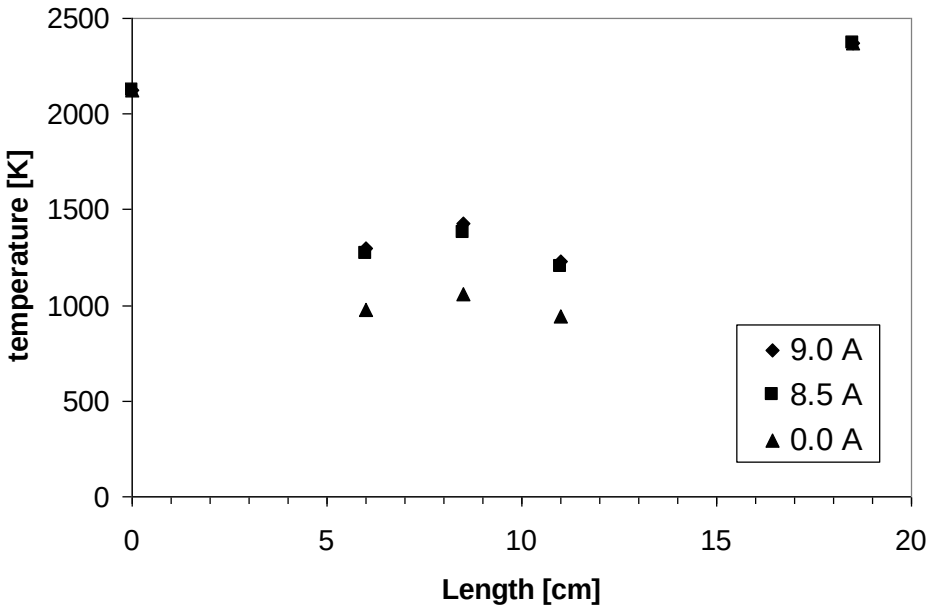

Fig. 3.6: Temperature gradient from the target (0cm) along the transfer line to the ion source (19cm) for different line heater currents. The heated part of the transfer line is at 6 to 11 cm.

Targets

For the measurement of radioactive yields uranium carbide was chosen as the production target because of the wide variety of elements produced in fission. Two different types of uranium carbide targets were used. Both sets were contained within an all-graphite target holder (Fig. 3.5, 1).

The first set of targets ("pressed powder") was used for all yield measurements except the repeat measurements of Kr, Rb and Sr. The targets were produced at ORNL in the Chemical and Material Sciences Facility, using a procedure to obtain UC_x with a grain size of 3 µm or smaller. The grains were mixed with graphite powder and pressed into pellets of 1.48 cm diameter, 0.17 cm thickness and a density of 2.28 g/cm^3.

The second set of targets ("graphite fiber") was used for repeat measurements of Kr, Rb and Sr yields, as well as for Kr and Rb hold-up times. The targets were expected to reduce the yields of Kr and therefore allow more precise measurements of direct Rb and Sr production. They were produced by Babcock and Wilcox, using a reticulated vitreous carbon (RVC) matrix (Cowlard, 1967). This graphite "foam" has an open pore structure with high surface area (23.8 cm^2/cm^3). The graphite fibers have a thickness of 60 µm. They were coated with 10 µm of Ir to keep fission products from diffusing into the fibers. A layer of UC_2 (14 µm) was deposited on top of the Ir layer by dipping the targets in a slurry containing stoichiometric amounts of colloidal carbon and UO_3 and

then dried at low-temperature. The disks were then heated under vacuum at 1750° C to form UC_2 (Alton 1998). The disks are 1.46 cm in diameter, have a thickness of 0.18 cm and a density of 1.83 g/cm^3.

Fig. 3.7: Photograph of pressed-powder UC_x target

Fig. 3.8: Photograph of UC2 coated RVC fiber target

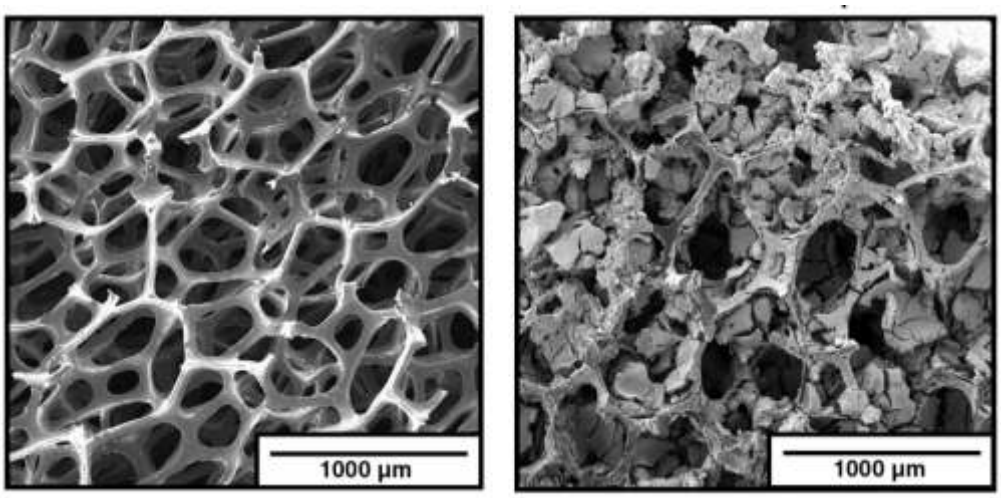

Fig. 3.9: SEM picture of uncoated and UC_2 coated RVC fibers

For the hold-up time measurements with stable beams, uncoated RVC was used as a catcher. It was cut to a diameter of 1.4cm and a thickness of 1cm, to completely block the hole leading to the transfer line. The entry window for the heavy ion beams consisted of a 1.654 mg/cm^2 Mo foil.
For all measurements done with this TIS the target / catcher was kept at a temperature of 1910° C (± 20° C).

3.2.2 Yield measurements

The yield Y of a given nuclide from an ISOL TIS is defined as the number of atoms released per second per primary beam current at equilibrium. To measure this quantity a radioactive ion beam of a given mass is deposited on a movable tape. After a given collection time the collection spot is moved in front of a γ-detector. The γ-rays emitted from nuclides deposited on the movable tape are then measured during the counting time, which generally is the same as the collection time unless a delay needs to be introduced. Tape cycles are adjusted to half-lives of the nuclide of interest.
Yields are calculated according to:

$$Y = \frac{N_\gamma \lambda}{b_\gamma \varepsilon_\gamma I\, n_{cyc} (1-\exp(-\lambda t_{coll}))(1-\exp(-\lambda t_{ct}))\exp(-\lambda t_d)} \qquad (3.1)$$

With N_γ: Number of γ rays detected
λ: decay constant (s^{-1})
b_γ: branching ratio
ε_γ: gamma detection efficiency
I: tandem current (µA)

n_{cyc}: number of measurement cycles
t_{coll}: collection time (s)
t_{ct}: counting time (s)
t_d: delay time (tape move time plus delay, s)

All yields given are in units of number of atoms per second per μA of proton beam on target.
The γ-detector used in this experiment is a High Purity Ge(Li) detector. Data acquisition for the yield measurements employed a Canberra MCA and the program Genie2000. For all measurements (yields and hold-up times) done with the fiber target, the ORNL physics division acquisition system ORPHAS was used. Efficiency and energy calibrations were done using a mixed calibration source containing ^{154}Eu, ^{155}Eu and ^{125}Sb.

3.2.3 Hold-up times

Hold-up time measurements determine the release time of particles by observing the decrease in yield after production / deposition in the target has stopped. Alternatively, the increase after starting production / deposition in the target can be observed as well. Since the release process from a target ion source is rather complex and must include delay distributions caused by diffusion, desorption from the target surface, effusion through the transfer line and ionization, it has not been attempted to fit all those parameters to the experimentally obtained curves. Instead, since in most cases the hold-up curves can be described by a two component exponential decay (eq. 3.2), a phenomenological approach has been chosen and leads to satisfactory results in the description and prediction of release behavior. The simple model proposed by Spejewski (Spejewski E.H., 2008) includes the production target, having a delay constant μ, a ‘‘delayer” representing transport through most of the system having a delay constant ν and an ion source having an efficiency ε for a stable isotope of that element (see fig. 3.10).
It is assumed that a fraction f of the products is delayed in the ‘‘delayer” while the fraction (1-f) proceeds directly to the ion source.

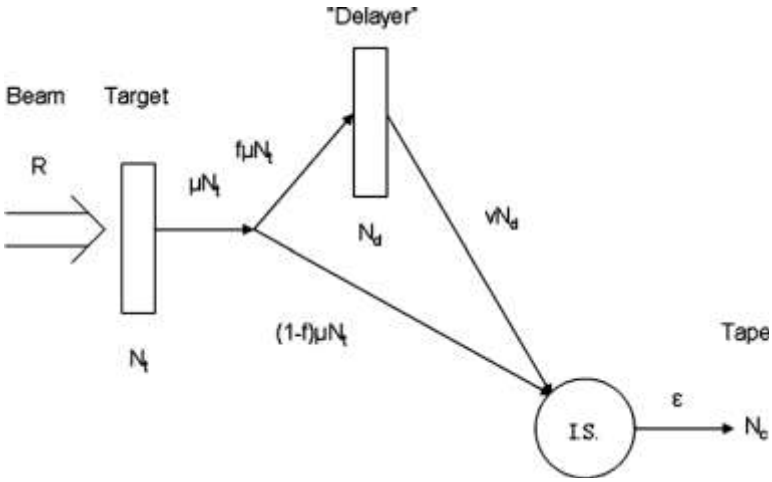

Fig. 3.10: Schematic of the two component release model

The experimental hold-up behavior for most elements is described by the following function:

$$\eta(t) = N_\mu \exp(-(\mu + \lambda)t) + N_\nu \exp(-\nu + \lambda)\, t) \tag{3.2}$$

λ is the radioactive decay constant, N_μ, N_ν, μ and λ are the hold-up parameters describing the release behavior. In analogy to a radioactive half-life, hold-up times can be calculated from μ and λ according to:

$$T_1 = \frac{\ln 2}{\mu} \quad \text{and} \quad T_2 = \frac{\ln 2}{\nu} \tag{3.3}$$

Average release times t_r can be calculated by integrating:

$$t_r = \int_0^\infty t\, \eta(t) dt = \frac{N_\mu\, \nu + N_\nu\, \mu}{\mu\, \nu\, (N_\mu + N_\nu)} \tag{3.4}$$

The model can also be used to predict yields of other nuclides of the same element Z, according to:

$$Y(Z,N) = \frac{\mu_Z[(1-f_Z)\lambda_{Z,N} + \nu_Z]}{(\mu_Z + \lambda_{Z,N})(\nu_Z + \lambda_{Z,N})} \varepsilon_Z R_{Z,N} \tag{3.5}$$

with $f = \frac{(\nu+\lambda)(\mu-\nu)}{\Lambda(\mu+\lambda)\mu + (\nu+\lambda)\mu}$ and $\Lambda = \frac{N_\mu\,[\exp(-\nu t_g) - 1]}{N_\nu\,[\exp(-\mu t_g) - 1]}$, t_g being the collection time, ε the efficiency of the system and R the production rate in the target.

Equation 3.5 has been used to calculate suppression factors (yield ratios) from hold-up parameters obtained under different transfer line conditions to compare with experimental yield ratios. This eliminates the efficiency and production parameters (ε,

R) since they are identical for the same nuclide and target. The predicted suppression factor S between yields measured with different materials (m) and at different temperatures (T) can be calculated according to:

$$S = \frac{Y_1(m_1,T_1)}{Y_2(m_2,T_2)} = \frac{\frac{\mu_1[(1-f_1)\lambda+\nu_1]}{(\mu_1+\lambda)(\nu_1+\lambda)}}{\frac{\mu_2[(1-f_2)\lambda+\nu_2]}{(\mu_2+\lambda)(\nu_2+\lambda)}} \quad (3.6)$$

Conversely, hold-up parameters can be determined from a fit of measured yields. Eq. 3.5 can be rewritten into:

$$\frac{R}{Y} = \frac{1}{\epsilon}\left[1+\lambda\left(\frac{\Lambda+1}{\Lambda\mu+\nu}\right)\right] = \left[\frac{(\mu+\lambda)Z(exp(\nu t)-1)+(\nu+\lambda)(exp(\mu t)-1)}{Z(exp(\nu t)-1)\mu+(exp(\mu t)-1)\nu}\right] \quad (3.7)$$

with $Z = \frac{N\mu}{N\nu}$.

This can be used for fitting, with R/Y the dependent variable and λ the independent variable and ε, μ, ν and Z the obtained parameters. A minimum of 5 yield measurements for the same element is required for this method.

Hold-up time parameters were measured using both radioactive and stable beams. Stable hold-up time measurements were performed by observing the beam current over time (see fig. 3.11), using a Faraday cup connected to a WinDAQ data logger for detection. The data logger was calibrated using a Keithley 6220 DC current source, in the range of 0.1 pA to 1 μA. Logging intervals were set at 0.1 s; this number was also used for collection times t_g in eq. 3.5.
For most currents the response time was below 0.1 s; however it was found to increase dramatically when currents dropped below 10pA. Therefore no measurements were done below this threshold.

For radioactive hold-up time measurements, tape cycles were adjusted to match the half-life (see table 3.3) and projected hold-up times and cycles continued until little activity could be seen. Gamma data were taken in list mode; for analysis, time bins were adjusted to cycle times to plot counts from each tape movement (see fig. 3.12). Hold-up curves obtained with either method were then fitted to a 2 component exponential, according to Spejewski et al. (Spejewski E.H., 2008)(see fig. 3.13)

Table 3.3: Cycle times used for measurements of hold-up times with radioactive nuclides

Nuclide	Half-life	Cycle time
^{90}Kr	32.32s	2s
^{89}Kr	189s	60s
^{89}Rb	909s	60s

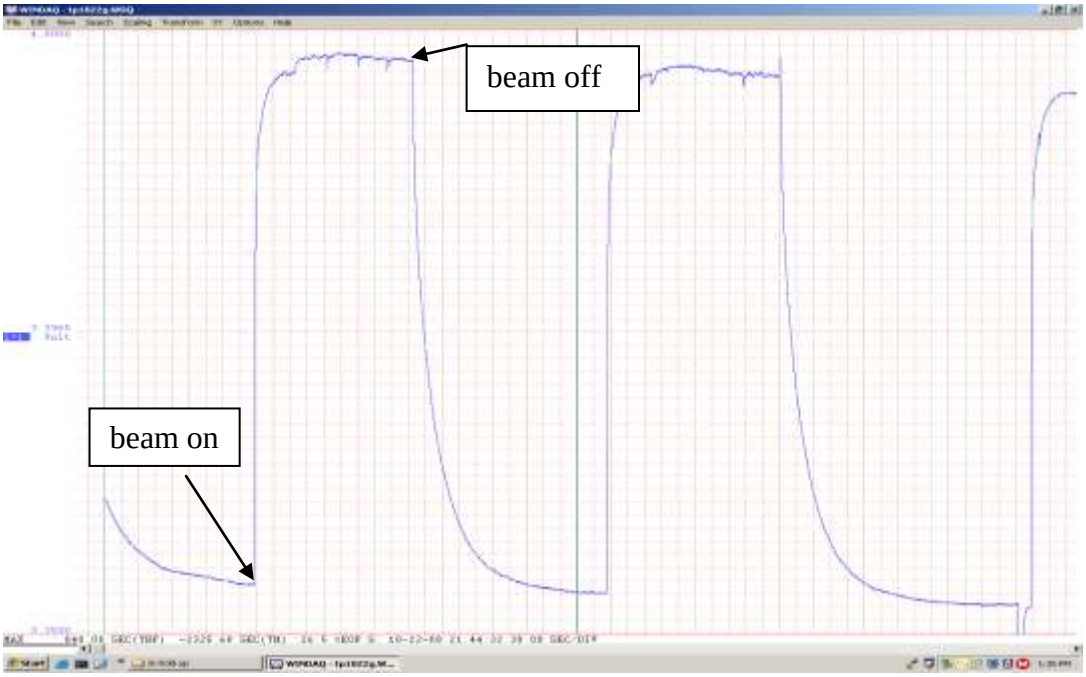

Fig. 3.11: Beam current plotted continuously by WinDAQ data logger

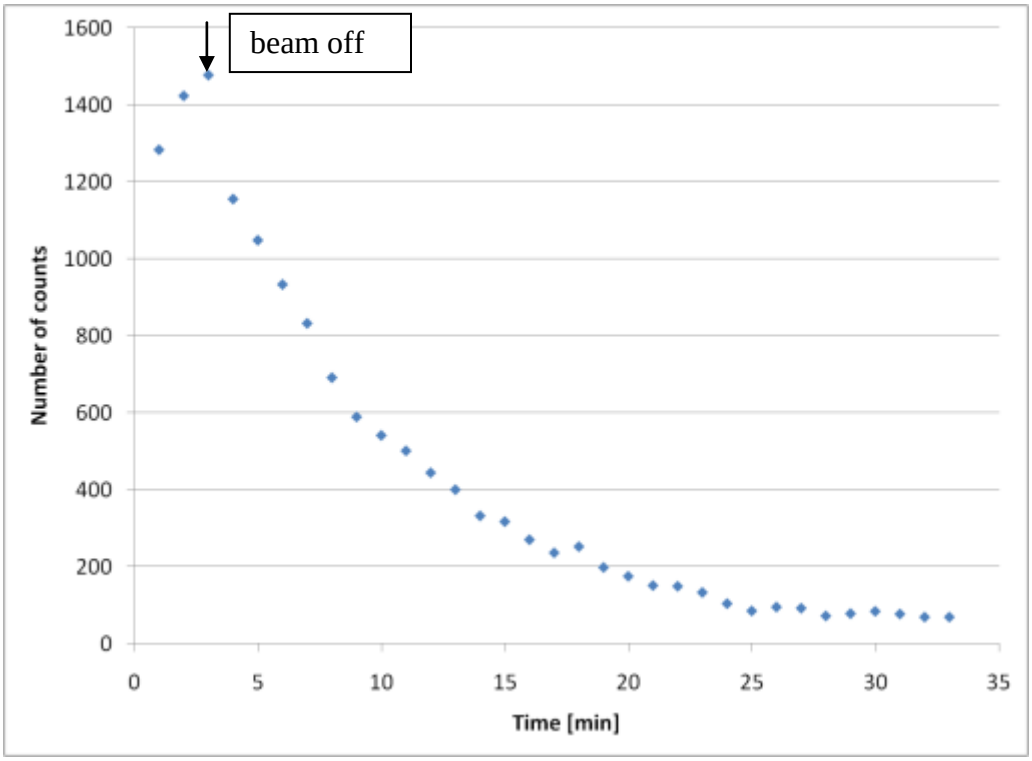

Fig. 3.12: Hold-up measurement on ^{89}Rb with 1023 keV line

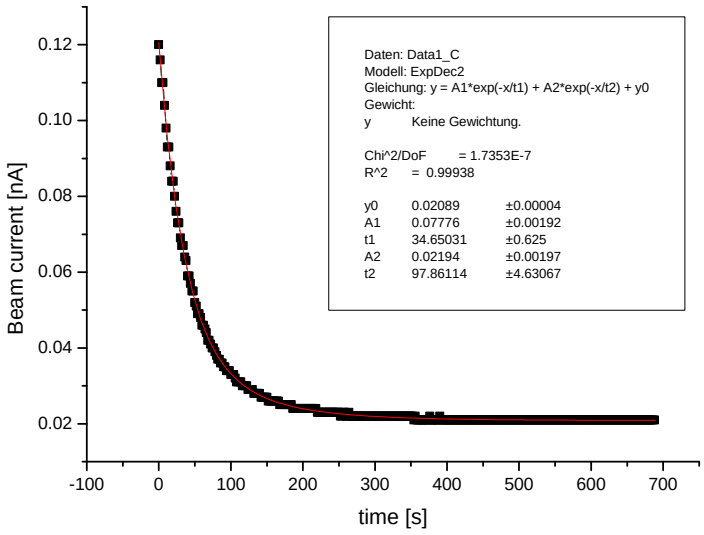

Fig. 3.13: Fit of hold-up curve for Ag, quartz low temperature

The hold-up parameters and deduced average release times can be used to calculate adsorption enthalpies. The difference Δt between the average release times t_r (from eq. 3.4) under two different transfer line conditions (materials and/or temperature) is only due to changes in sticking time t_s:

$$\Delta t = t_{r,1} - t_{r,2} = n_{col,1} t_{s,1} - n_{col,2} t_{s,2} \quad (3.8)$$

with n_{col} the number of collisions in the horizontal part of the transfer line and the sticking time being given by the Frenkel equation:

$$t_s = t_0 \exp\left(-\frac{\Delta H_{ads}}{kT}\right) \quad (3.9)$$

t_0 is the inverse of the Debye frequency, ΔH_{ads} the adsorption enthalpy, k the Boltzmann constant and T the line temperature. Since there is a temperature gradient T(x) along the relevant part of the transfer line eq. (3.9) should be substituted with:

$$t_s = t_0 \int_0^x \exp\left(-\frac{\Delta H_{ads}}{kT(x)}\right) dx \quad (3.10)$$

This can be approximated by dividing the length of the transfer line L in n isothermal sections of the length l, with the complete equation for one transfer line material:

$$\Delta t = n_{col,1} t_o \sum_{i=1}^{n} exp\left(-\frac{\Delta H_{ads}}{kT_{i,1}}\right) - \left[n_{col,2} t_o \sum_{i=1}^{n} exp\left(-\frac{\Delta H_{ads}}{kT_{i,2}}\right)\right] \quad (3.11)$$

In practice, ΔH_{ads} will not be changed significantly by increasing n to more than 5. Even with a tube of some adsorption material m inserted in the transfer line, atoms still collide with the Ta wall (travelling between the outer and the inner tube). There is, thus, some contribution from the sticking time on Ta, which for most elements cannot be neglected. Therefore it becomes necessary to extend eq. (3.11) to include this:

$$\Delta t = n_{col,1}^{Ta} t_o^{Ta} \sum_{i=1}^{n} \exp\left(-\frac{\Delta H_{ads}^{Ta}}{kT_{i,1}}\right) + n_{col,1}^{m} t_o{}^{m} \sum_{i=1}^{n} \exp\left(-\frac{\Delta H_{ads}^{m}}{kT_{i,1}}\right)$$
$$- \left[n_{col,2}^{Ta} t_o^{Ta} \sum_{i=1}^{n} \exp\left(-\frac{\Delta H_{ads}^{Ta}}{kT_{i,2}}\right) + n_{col,2}^{m} t_o{}^{m} \sum_{i=1}^{n} \exp\left(-\frac{\Delta H_{ads}^{m}}{kT_{i,2}}\right)\right] \quad (3.12)$$

Since eq. (3.12) contains two unknown parameters, it was necessary to extract the adsorption enthalpy on Ta surfaces first, using eq. (3.11), then use this result in eq. (3.12).

3.2.4 Adsorption materials

The “standard” material of the transfer line is a Ta tube, outer diameter (OD) 9.525 mm, wall thickness (WT) 0.508 mm and inner diameter (ID) 9.017 mm.
The tubes inserted for adsorption were made from quartz glass and sapphire. In the case of the quartz tube, there were two different configurations in order to investigate whether the fraction of atoms travelling straight through the tube without hitting the walls was relevant to the results. Therefore, along with a straight quartz tube (see fig. 3.14), a partially blocked one was fabricated with no direct view through the tube (see fig. 3.14). Dimensions of the tubes are given in table 3.4.

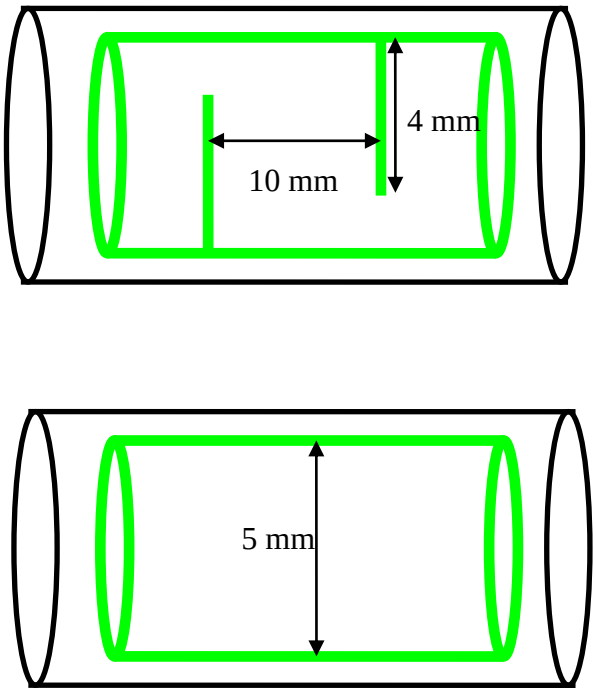

Fig. 3.14: Straight (lower) and partially blocked (upper) quartz tube

The sapphire tubes were manufactured by the company Saint Gobain. Monocrystalline tubes are grown by solidifying melted ultra pure raw materials under strict control of thermal conditions (Gobain, 2009). Therefore only straight tubes could be produced. Dimensions of the tubes are given in table 3.4.

Table 3.4: Dimensions of tubes used for adsorption materials

Material/ geometry	Outer diameter (mm)	Inner diameter (mm)	Wall thickness (mm)	Length (mm)
Quartz /straight	8.1	6.05	1.0	49.0
Quartz / blocked	8.1	6.05	1.0	49.0
sapphire	8.0	6.0	1.0	48.0

3.3 RIBO

The Monte Carlo code RIBO (*R*adioactive *I*on *B*eam *O*ptimizer) (Santana-Leitner, 2005) has been used to calculate the number of collisions of atoms in the transfer line. RIBO tracks each test particle from generation to extraction, modeling diffusion in slabs, fibers and powders, effusion from containers and porous media, both under molecular flow conditions and in the intermediate regime, adsorption and desorption on walls and ionization.
In this case it was used to create a model of the modified transfer line (see fig. 3.15) starting from the connection to the target container and ending at the entrance to the ion source. Models were created for the bare transfer line as well as the line containing a straight tube and a partially blocked tube. Since in the real TIS the inserted tube had to be slightly smaller than the inner diameter of the transfer line (due to deviation from the cylindrical shape in both tubes), simulations were run both with the inner tube centered in and “resting” on the outer tube. No significant differences could be detected in the results. Simulations were done using 50,000 particles for good statistics.

Fig. 3.15: Visualization of the RIBO model for the modified transfer line containing a straight tube

The number of collisions on all surfaces in the horizontal part of the transfer line (see fig. 3.15, between arrows) was determined for all three models and number of collisions on the same material (Ta or inserted tube) were summed up. Table 3.5 shows the results of those simulations.

Table 3.5: Number of collisions on line surfaces with and without tubes inserted

Number of collisions on surface /cm	Ta	Inserted tube
Bare line	367	0
Line with straight tube	397	602
Line with blocked tube	444	726

When plotting the probability of a particle to be released after a certain number of collisions the obtained curves show an exponential behavior (see fig 3.16). If assuming the same sticking time for every collision, the curve will translate directly into a release time probability curve. All curves can be fitted with good agreement to the following function:

$$P(x) = [1 - \exp(-\lambda_1 x)][A_1 \exp(-\lambda_2 x) + A_2 \exp(-\lambda_3)].$$

Interestingly, this has also been reported by Lettry et al. (Lettry, 1997) as a fit function for the release probability from an ISOLDE TIS, even though the online release is influenced by diffusion as well as effusion.
It can also be seen that the introduction of a straight (quartz 1, fig. 3.16) or partially blocked (quartz 2, fig. 3.16) tube leads to a broader distribution and therefore (assuming constant sticking times) a longer release time for particles.

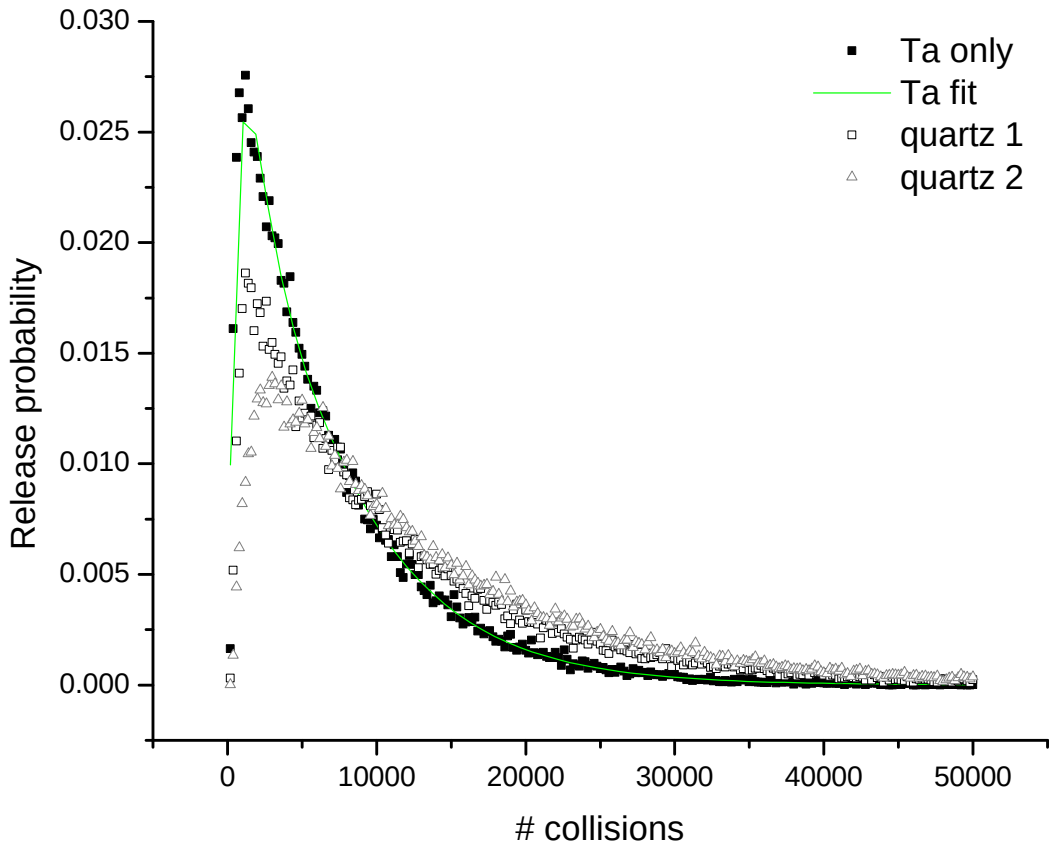

Fig. 3.16: Release probabilities for particles in the bare Ta line, with a straight tube inserted (quartz 1) and with a partially blocked tube inserted (quartz 2)

3.4 Spectroscopy

The spectroscopy data discussed here were taken at CERN-ISOLDE.
The target was pressed UC_x powder; the proton beam was focused on a W converter rod to avoid spallation and increase fission reactions in the target. This leads to a higher yield of neutron-rich reaction products and decreases contaminations closer to stability.
The transfer line was the medium-temperature prototype #1 with a quartz insert, run at 680° C (Bouquerel, 2007). It was used to remove In and Cs contaminations from neutron-rich Cd beams.
The ISOLDE laser ion source system RILIS was used to ionize Cd.

The experiment was located at beam line LA2 (see fig 3.17). The beam was implanted in a ½ inch movable tape that was synchronized with the signal from the PS booster, so that the tape could only be moved during a proton pulse. 4 HP Ge γ-detectors were used for measurements. Because of a failure in the data acquisition system, only single spectrum data were taken. The program InterWinner (InterWinner) was used for data analysis.

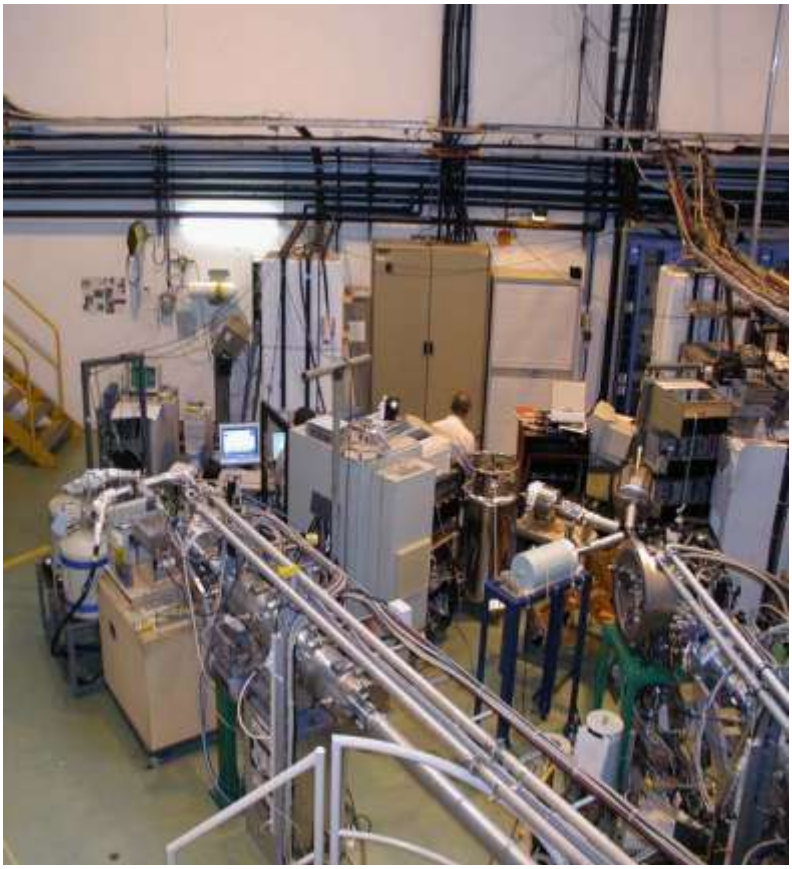

Fig. 3.17: Beam line LA1 (left) with tape station and γ-detectors

4 RESULTS & DISCUSSION

4.1 Target-ion source development

4.1.1 Selective adsorption experiments

This chapter presents and discusses the results of the adsorption experiments conducted. The results are organized by chemical element, discussing results obtained with different methods separately for elements of each group.
Plots of all yield results are shown in the subchapters for the various elements. In these plots, errors are plotted only for the shortest and longest half-life measured under all conditions for better clarity, but are generally in the range of 15%.

4.1.1.1 Results & Discussion: Selective Adsorption - Ag

The chemical behavior of Ag on Ta, quartz and sapphire surfaces has been determined using thermochromatography, yield, and hold-up time measurements.

Hold-up times

In general Ag has good production efficiencies from a standard ISOL system. This is possible only with both fast diffusion out of the graphite target system and little interaction with high temperature surfaces. Therefore Ag proved to be very well suited for testing the stable beam hold-up method; the short diffusion times allow extremely precise determination of release time variations because of changes of transfer line material.

As expected the hold-up times determined for stable Ag at high line temperatures are quite short, with a fast component of 2.8 to 3 s and average release times below 10 s (see table 4.1). Even with the inherent high precision, average hold-up times on the three different materials tested are the same within the uncertainties of the data fit, proving that there is no selective interaction of Ag with any of the tested surfaces at high temperatures.

However, there is a pronounced temperature dependence. At lower temperatures Ag exhibits strong interaction with quartz, sapphire and tantalum. The Ag release is slowed by quartz surfaces, as could be expected from the amorphous structure and thus higher surface activity of this material. Interestingly, the average hold-up times show the fastest release when using a sapphire surface, even though the chemical interaction could be expected to be stronger than an average metal-on-metal

adsorption. However, since Ag exhibits a much stronger interaction with Ta than most other metals (Rossbach 1984), this behavior is not inconsistent. The strong interaction of Ag with low temperature Ta surfaces should be considered whenever designing systems for the production of this element, to avoid Ta “cold spots” slowing down the release.

Table 4.1: Average Ag hold-up times

Average Ag holdup time (s) on	Ta	sapphire	quartz
High temp. line	7.9 ± 1.0	8.2 ± 1.2	8.6 ± 1.5
Low temp. line	51.0 ± 1.5	29.8 ± 1.5	49.1 ± 1.7

Adsorption enthalpies and Thermochromatography (TC)

The observed strong dependence of hold-up times on transfer line temperature results in high adsorption enthalpies (see table 4.3), with only small variations for the three materials used. The result for quartz is consistent with the average enthalpy of adsorption for Ag derived from the TC experiments both at Mainz and CERN-ISOLDE (see table 4.2).

It could be observed in the offline experiments that the behavior of Ag on quartz varies slightly with oxygen and water content of the surrounding atmosphere. Without a reducing atmosphere the obtained adsorption enthalpy of -214 ± 12 kJ/mol is in good agreement with results from experiments based on the same evaluation model (Hohn, 2004). In He/H_2 atmosphere the peak shifts entirely to lower temperatures, and no second peak is found. The results obtained at CERN, with a cleaner inert-gas flow, yield the same adsorption enthalpy (-191 ± 11 kJ/mol) as found at Mainz with addition of H_2. This change of adsorption behavior may be explained by the formation of a silver oxide or, more probable, changes in the quartz surface activity with the concentration of impurities (see chapter 2.4.2, surface hydroxylation).

Table 4.2: Adsorption enthalpies and deposition temperatures of Ag on quartz glass

Mainz			CERN		
carrier gas	deposition temperature T (K)	adsorption enthalpy -ΔH (kJ/mol)	carrier gas	deposition temperature T (K)	adsorption enthalpy -ΔH (kJ/mol)
He He/H_2	1085 823	214 192	Ar	805	191

Since in the offline experiments the adsorption behavior of Ag on quartz seems to vary slightly with oxygen and water content of the surrounding atmosphere, the retention in the transfer line is likely to change with the amount of those substances present in the system, *e.g.* when switching from a carbide to an oxide target. However, the variations are not very large and might not be noticed when performing the less sensitive yield measurements.

The obtained adsorption enthalpies of Ag on Ta are considerably lower than that predicted by the Eichler-Miedema model (Rossbach 1984) for adsorption of metals on metal surfaces (-315.8 kJ/mol). An enthalpy as high as the one calculated with this semi-empirical model would not allow Ag to be released from the standard Ta TIS system at all. Therefore the value given by the Eichler-Miedema model, though showing the general trend of a strong interaction of those metals, does not explain the behavior, in this case at least.

The observed strong interaction of Ag with Ta also proves that when investigating new adsorption materials, the interaction with the Ta surface cannot be neglected for all elements since it will contribute significantly to the release time, especially at lower temperatures. This justifies the addition of terms for adsorption on Ta in the equations for the determination of adsorption enthalpies from hold-up parameters (eq. 3.12 in chapter 3.2.3).

Table 4.3: Adsorption enthalpies of Ag on different surfaces, from hold-up time measurements and TC

experiment	Hold-up times on Ta	Hold-up times on quartz	Hold-up times on sapphire	TC on quartz
ΔH_{ads} (kJ/mol)	-203	-202	-200	-198

Yields

The Ag yield measurements are also affected by changes in transfer line material and temperature. Results gained with the high temperature quartz are slightly lower than the high temperature Ta yields (see fig. 4.1a). Lowering the temperature of the quartz reduces the yields even further. A stronger suppression was observed at shorter half-lives (see fig. 4.1b). This is consistent with a reversible adsorption-desorption equilibrium causing an increase of release time.

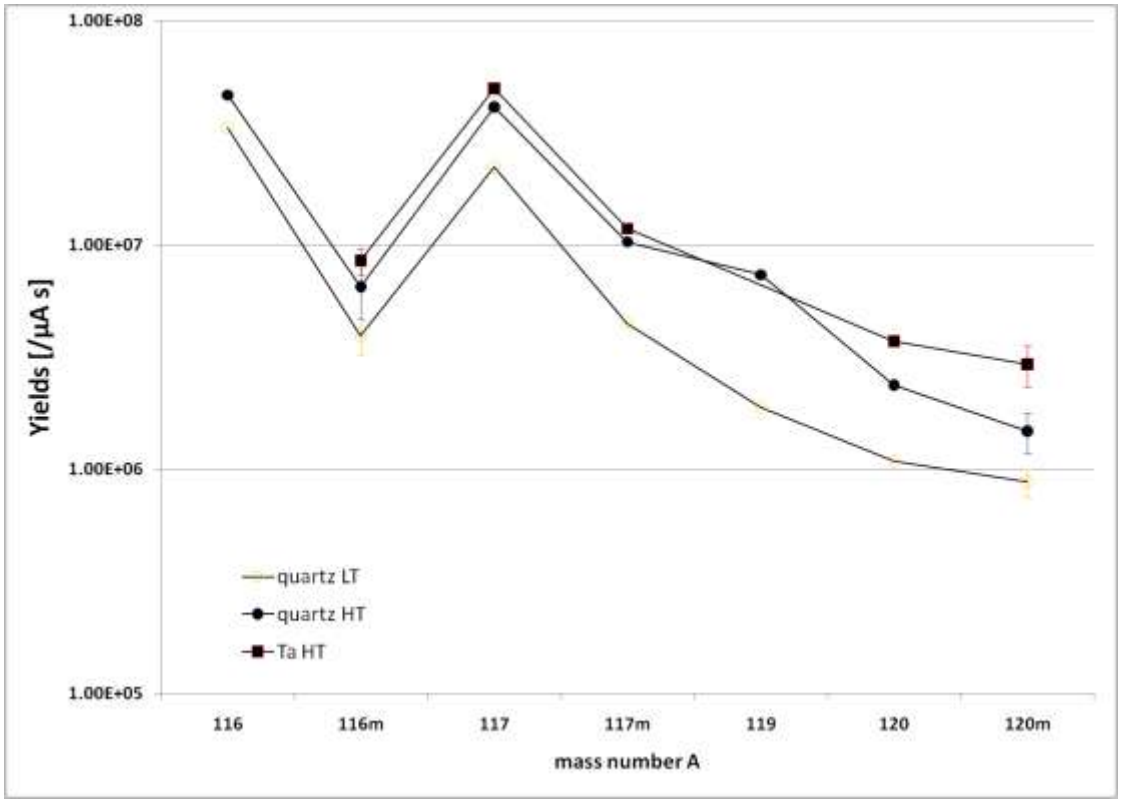

Fig. 4.1a: Ag yields from pressed-powder target

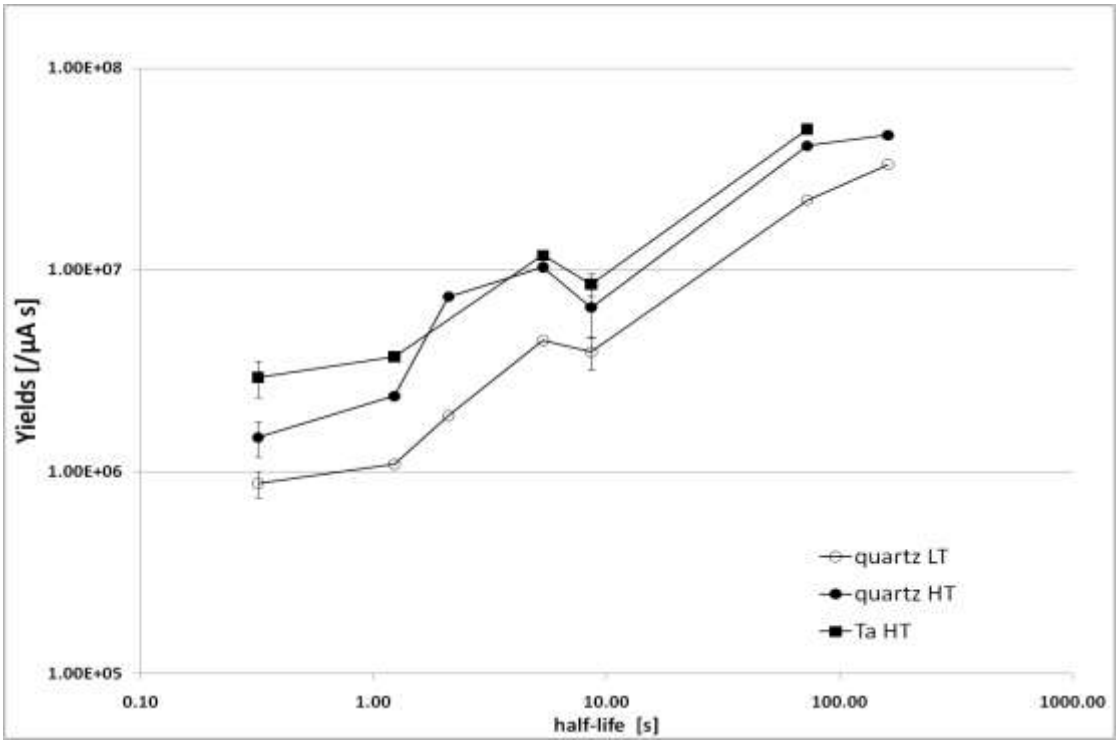

Fig. 4.1b: Half-life dependence of Ag yields from pressed-powder target

Yield ratio predictions

Using the hold-up parameters obtained from stable beams, the yields for radioactive nuclides can be predicted as described in chapter 3.2.3, eq. 3.5 (see table 4.4). For Ag, the results of the yield measurements and hold-up times are generally consistent. In the case of the ratio of the yields measured with a high temperature Ta surface and a low temperature quartz surface (see table 4.4, fig. 4.2), the values are very close to the predicted values, even though the uncertainties are quite high. The agreement of the quartz high temperature / quartz low temperature yield ratios is not as good. For the long -lived ^{117}Ag ($t_{1/2}$ = 73 s), both experimental values for the Ta HT/q LT ratio and the q HT/q LT ratio are too high. This is most likely due to an incorrect (too low) yield value for the ^{117}Ag “q LT” measurement, possibly caused by a drop in ion source or tandem beam intensity during the measurement. Theoretically the yield ratio should be approaching 1 for longer half-lives. This is not consistent with the very high experimental yield ratio shown here.

Table 4.4: Ag yield ratios – predictions and experimental results

Isotope	Half-life (s)	Yield ratio Ta HT/ q LT			Yield ratio q HT/ q LT		
		calculated	measured	error	calculated	measured	error
120m	0.32	3.78	3.35	0.58	3.27	2.81	0.34
120	1.23	3.44	3.40	0.45	3.01	2.17	0.45
117	5.34	2.61	2.64	0.46	2.31	2.30	0.31
116m	8.6	2.28	2.17	0.45	2.02	1.66	0.41
117m	72.6	1.29	2.24	0.51	1.04	1.86	0.35

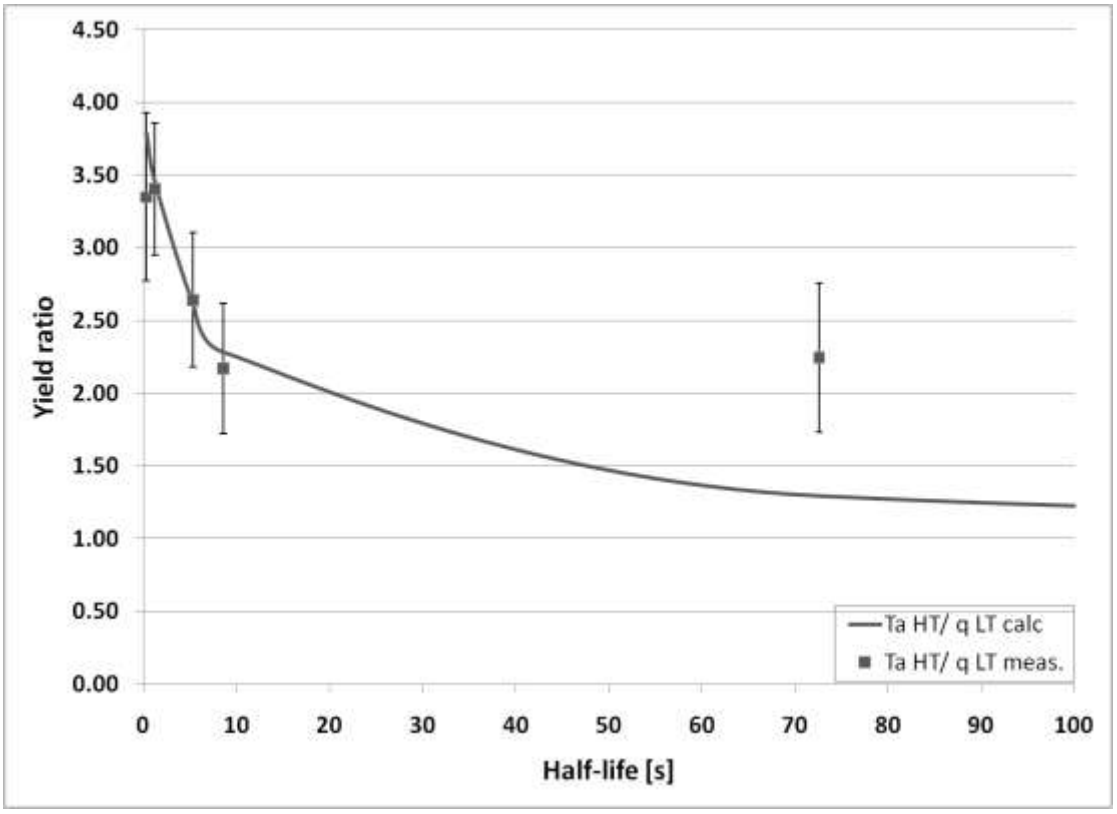

Fig. 4.2: Comparison of Ag yield ratios with prediction from hold-up measurements (Ta HT/ q LT)

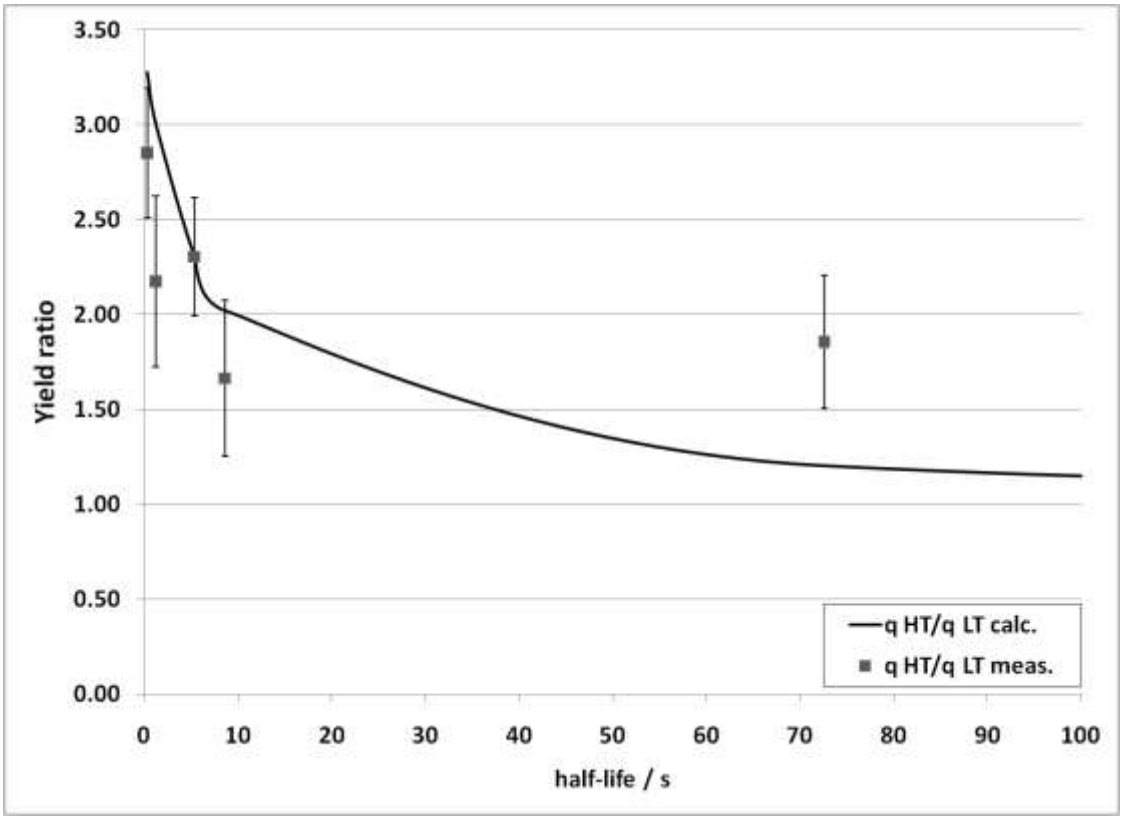

Fig. 4.3: Comparison of Ag yield ratios with prediction from hold-up measurements (qHT/qLT)

Summary

All results obtained for the adsorption behavior of Ag with different methods are consistent. This suggests that the models (see chapter 3.1 and 3.2) for the mechanisms controlling this behavior are applicable.

These results indicate that the interaction of Ag with all surfaces investigated is a good example of a reversible adsorption behavior. There are no irreversible chemical reactions causing a direct loss of atoms through absorption. The only losses are through radioactive decay. Therefore the effect of the surfaces on the adsorption times is only moderate; nevertheless it is influenced by both temperature and surface applied.

For application in an ISOL system, the strong interaction of Ag with Ta surfaces is noteworthy. It could be used to reduce Ag as a contaminant by purposely introducing a “cold spot” in the system. For optimization of Ag release, keeping all Ta surfaces at high temperatures will lead to shorter transport times. Recent tests run at the OLTF also indicate that replacing Ta surfaces in cool regions of the TIS system with graphite will improve the release of short-lived nuclides.

4.1.1.2 Results and Discussion: Selective Adsorption – Group 12

For the group 12 elements Zn and Cd, only yield measurements have been performed online, since no stable beams of those elements can be produced with the tandem accelerator. Thermochromatography data are also available and are very consistent with the online data, although enthalpies of adsorption could not be extracted from the yield measurements.

Table 4.5: TC results for group 12 elements

	Mainz			CERN		
elements	carrier gas	deposition temperature T (K)	adsorption enthalpy - ΔH (kJ/mol)	carrier gas	deposition temperature T (K)	adsorption enthalpy - ΔH (kJ/mol)
Zn	-	-	-	Ar	604	142
Cd	He He/H_2	<522 <522	<113 <113	Ar	345	80

For Zn, thermochromatography did not show a very strong interaction with the quartz surface. The single deposition peak was narrow and found at 604° C, corresponding to an adsorption enthalpy of -142 kJ/mol. No prior measurements of this constant could be found in the literature. Since the deposition temperature is lower than the minimum transfer line temperature achieved online, no strong suppression online was expected. At ISOLDE no reduction of Zn yields down to a temperature of 680° C has been observed. In our experiments all yields measured are also equal within their uncertainties. However, the results obtained with the quartz transfer line at low temperatures are always the lowest values. This indicates that a slight increase of release time occurs, because the temperature regime is close to the determined deposition temperature and, at the coldest spot, slightly cooler than the minimum temperature of the ISOLDE prototype #1 (Bouquerel, 2007). Unfortunately, no hold-up measurements could be run to confirm this.

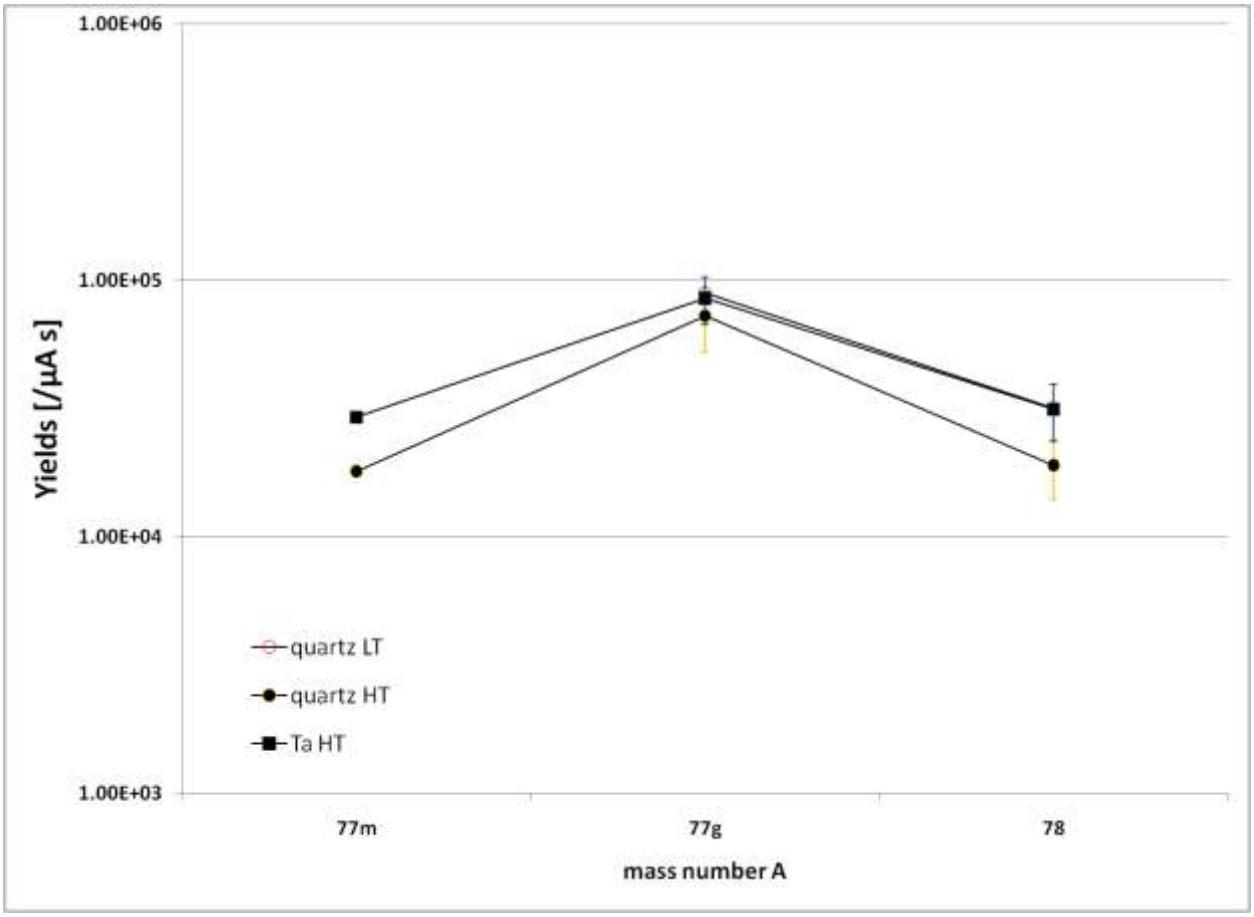

Fig. 4.4: Zn yields

Cd displayed a high volatility in both offline and online experiments, consistent with its low boiling point (767° C). This has been documented before, *e.g.* when using a water-cooled transfer line to purify Cd beams at ISOLDE (Koester, 2001). In TC it is

deposited at 345° C (ΔH_{ads} = 80 kJ/mol). In yield measurements, no consistent suppression can be observed under the experimental conditions applied. These results are also consistent with the current results from ISOLDE, using the same type of transfer line to purify Cd beams (Bouquerel, 2007).

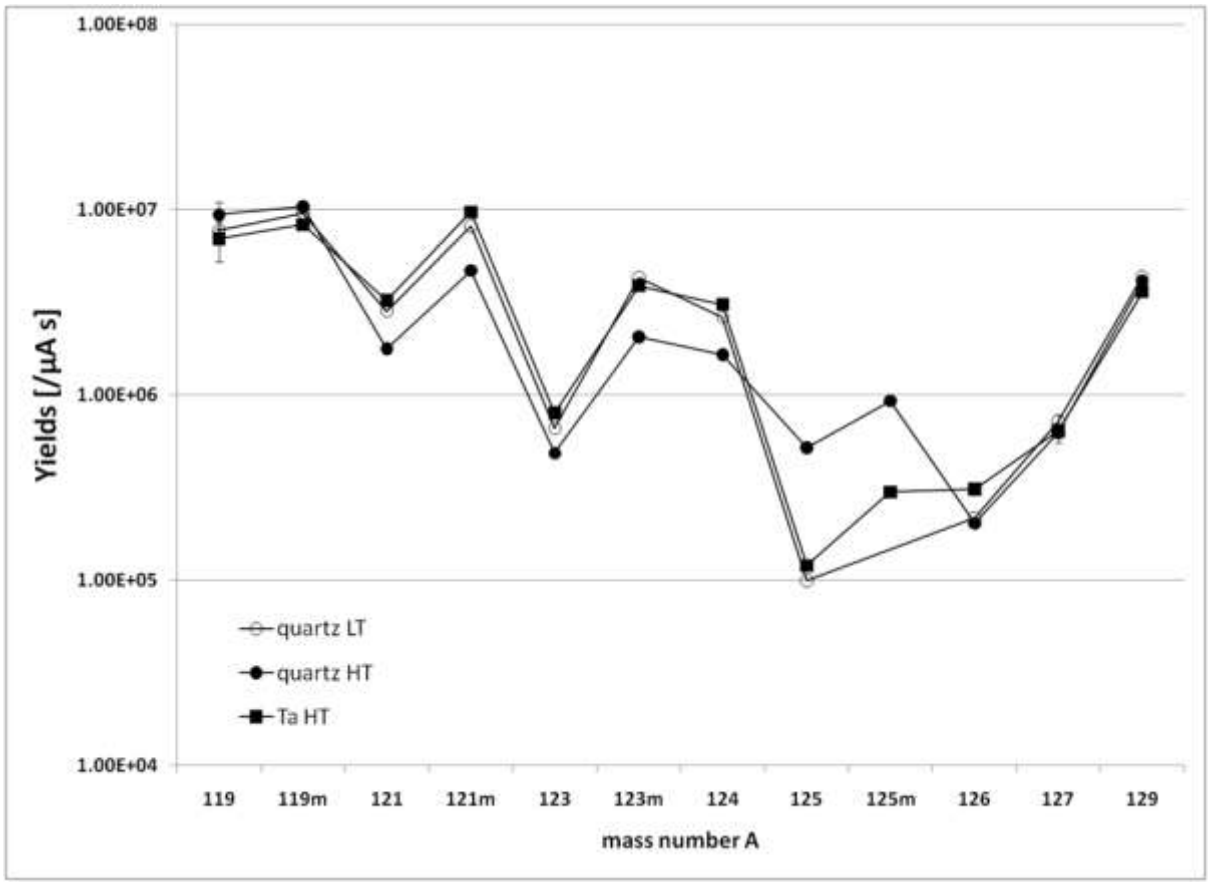

Fig. 4.5: Cd yields from pressed-powder target

Summary

Zn and Cd exhibit very similar behavior in both offline and online experiments and results from the different methods are very consistent. There are no indications of a strong chemical interaction with quartz or Ta surfaces. Zn, being the smaller homologue, follows the general trend seen in TC and is deposited at higher temperatures than Cd.
As a result of their high volatility and low reactivity towards the surfaces tested, Zn and Cd beams can easily be purified by reduction of temperature and introduction of a quartz glass surface.

4.1.1.3 Results and Discussion: Selective Adsorption - Group 13

The adsorption behavior of the group 13 elements Ga and In has been surveyed. For Ga, only yield measurements have been performed; In was investigated using TC, stable beam hold-up time measurements and determination of radioactive yields. ISOLDE reports a slight suppression of Ga yields when reducing the transfer line temperature from 900 to 700° C. They also observed a reduction of In by a factor 4 when changing from 1100 to 700° C (Bouquerel, 2007).

The Ga yields do not show any suppression either by material or temperature (see fig. 4.6), except for the quartz high temperature measurement at mass 78; this is probably because of a brief drop of the ion source or tandem beam intensity. Apart from this data point the results agree very well within their uncertainties. This is not consistent with results obtained at ISOLDE. The reason for this may lie in the use of a plasma ion source instead of the Resonance Ionization Laser Ion Source (RILIS) (see discussion of effects on surface ionization, chapter 4.1.3).

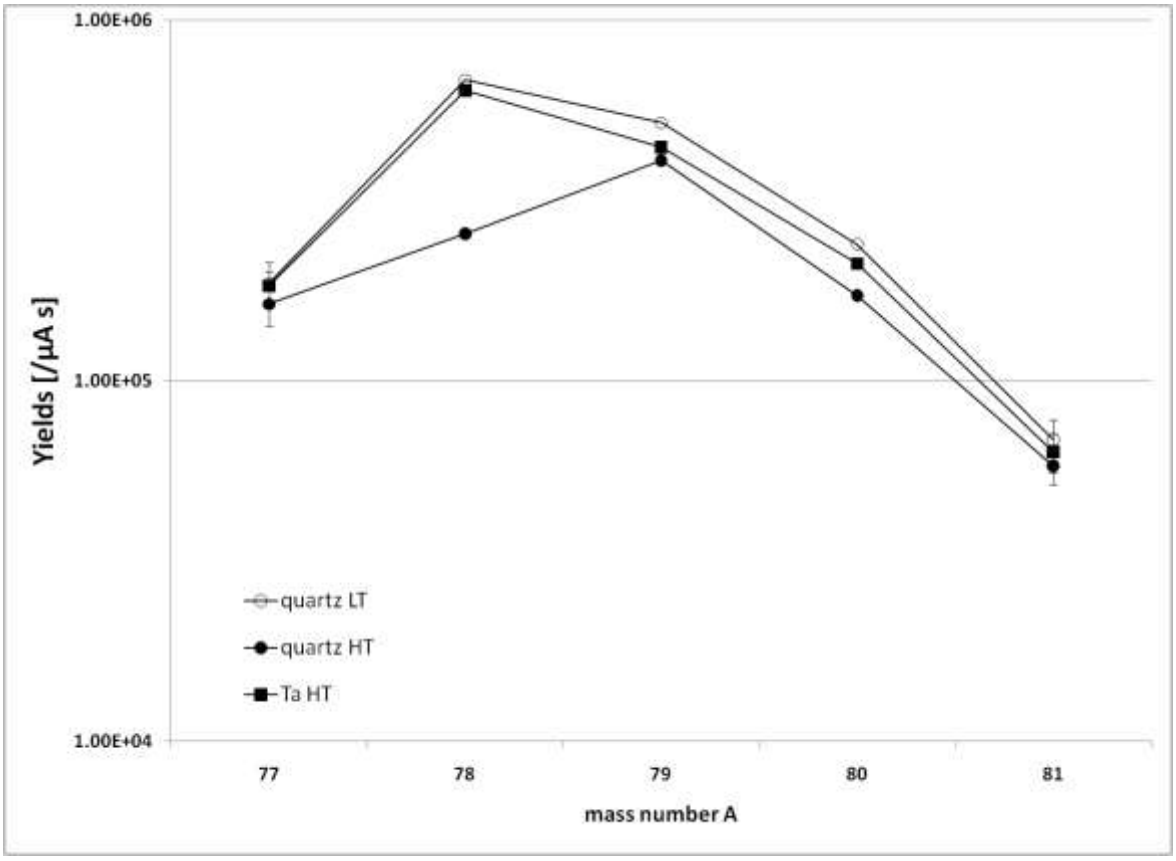

Fig. 4.6: Ga yields from pressed-powder target

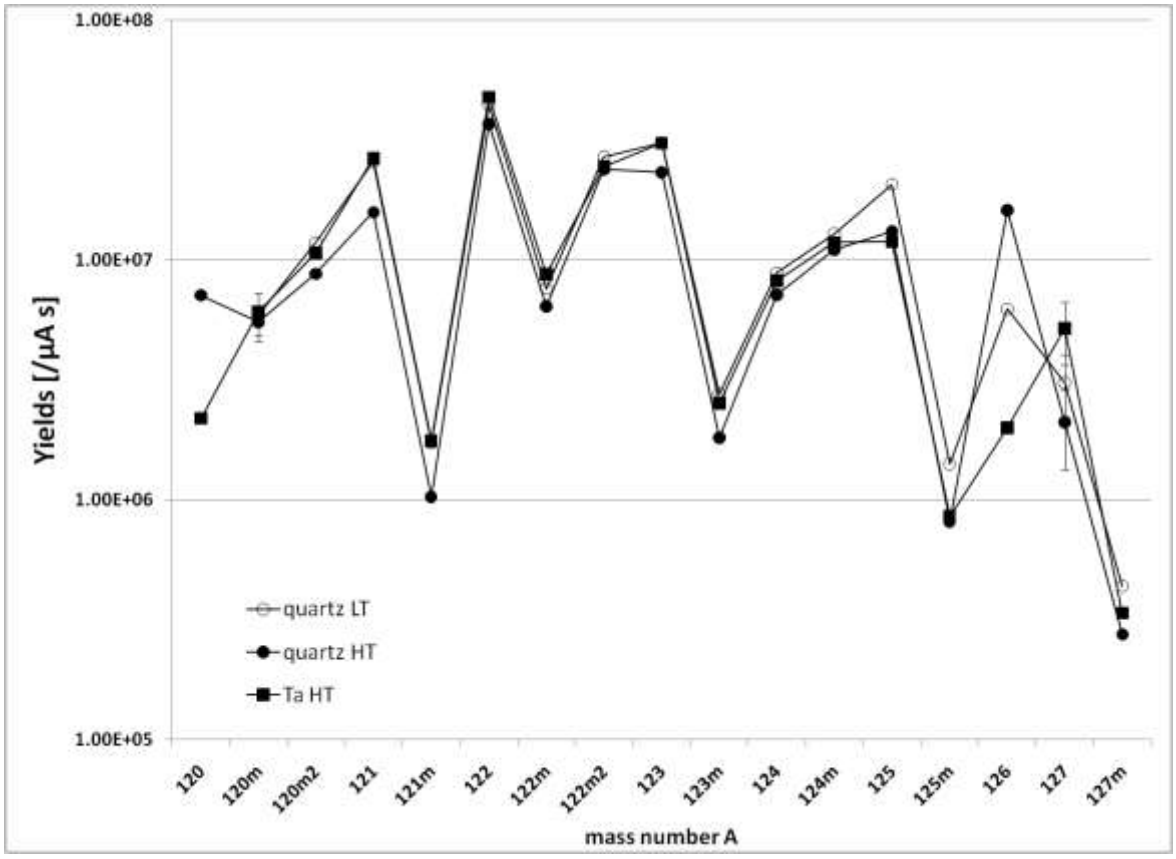

Fig. 4.7: In yields from pressed-powder target

For In as well, no suppression was detected in the yield measurements (see fig. 4.7), even though the low temperature is comparable with the one reported by ISOLDE.

The more sensitive hold-up data measured with stable In beams indicate that a slight change of release times does indeed take place. Both lower temperature and the introduction of quartz and sapphire surfaces result in a slight increase of transport time (see table 4.6). The maximum difference in transport time, between Ta at high line temperature and quartz at low line temperature, amounts to 4 s. However, when using these hold-up time results to predict a suppression in yields (see chapter 3.2.3, eq. 3.6), the differences between those predicted yield ratios are smaller than the experimental uncertainties for almost all masses measured (see table 4.7). Therefore no suppression should be observed. This is very consistent with the yield data taken at Oak Ridge.

In general, hold-up times for In are very short (3.7 – 7.8 s), indicating very fast diffusion of In in the graphite fiber catcher. This is consistent with high yields produced online, even for very short half-lives.

Table 4.6: In holdup times

Average In holdup time (s) on	Ta	sapphire	quartz
High temp. line	3.72 ± 0.11	6.29 ± 0.13	4.48 ± 0.13
Low temp. line	4.58 ± 0.12	5.63 ± 0.13	7.78 ± 0.12

Table 4.7: Comparison of experimental and calculated yield ratios for measured In masses

In nuclide	Half-life [s]	Yield ratio Ta HT / q LT	
		experimental	calculated
120m	46.2	0.10 ± 0.17	1.06
120m2	47.3	0.91 ± 0.23	1.06
121	23.1	1.03 ± 0.26	1.11
121m	234	1.02 ± 0.35	1.01
122	1.5	1.07 ± 0.36	1.68
122m	10.3	1.15 ± 0.27	1.22
122m2	10.8	0.91 ± 0.29	1.21
123	5.98	0.99 ± 0.22	1.33
123m	47.8	0.91 ± 0.28	1.06
124	3.11	0.93 ± 0.30	1.49
124m	3.7	0.92 ± 0.24	1.45
125	2.36	0.58 ± 0.23	1.57
125m	12.2	0.60 ± 0.19	1.19
126	1.6	0.32 ± 0.22	1.96
127	1.09	1.68 ± 0.13	1.76
127m	3.67	0.77 ± 0.52	1.45

The TC data clearly show that the deposition temperature and adsorption enthalpy of In on quartz depend on the concentration of oxidizing agents in the atmosphere (see table 4.8). With higher concentrations of oxygen and water, the deposition peak is shifted from 357 to 638° C. The adsorption enthalpies gained from the hold-up data are very similar to the TC results obtained with oxidizing agents present (see table 4.8). Since in a normal target-ion source a beam of several hundred nA of oxygen can usually be found in the mass spectra, this result is not inconsistent.
The effect of oxygen or water in the system is a possible explanation of the differences in adsorption behavior observed at ISOLDE and Oak Ridge, although the effect should not be as large. Another explanation for the different results may lie in

the different ion source employed (see discussion of effects on surface ionization, chapter 4.1.3).
The adsorption enthalpy derived for In on Ta surfaces does not agree with the rather high value given by Eichler et al. (-330 kJ/mol) (H. Rossbach, 1984).

Table 4.8: Comparison of In adsorption enthalpies from different methods

ΔH_{ads} from TC (kJ/mol)		ΔH_{ads} from hold-up times (kJ/mol)	
Quartz, He/H_2	Quartz, He only	Quartz	Ta
-88	-150	-151.4	-147.7

Summary

Neither Ga nor In exhibit a strong interaction with quartz or Ta surfaces in any of the methods used. A chemical reaction with quartz as a reason for the suppression observed at ISOLDE, therefore, does not seem likely. The reason for this could lie in reduced surface ionization (see chapter 4.1.3).

4.1.1.4 Results and Discussion: Selective Adsorption - Group 14

Of the group 14 elements, yield measurements have been performed for Ge. It was also attempted to collect yield and hold-up data for Sn but no release was observed except for hold-up measurements done with a hot Ta transfer line.

The yield measurements for Ge do not show any differences in response to changing temperature and transfer line materials (see fig. 4.8). No values for adsorption enthalpies to compare this behavior with could be found in the literature.

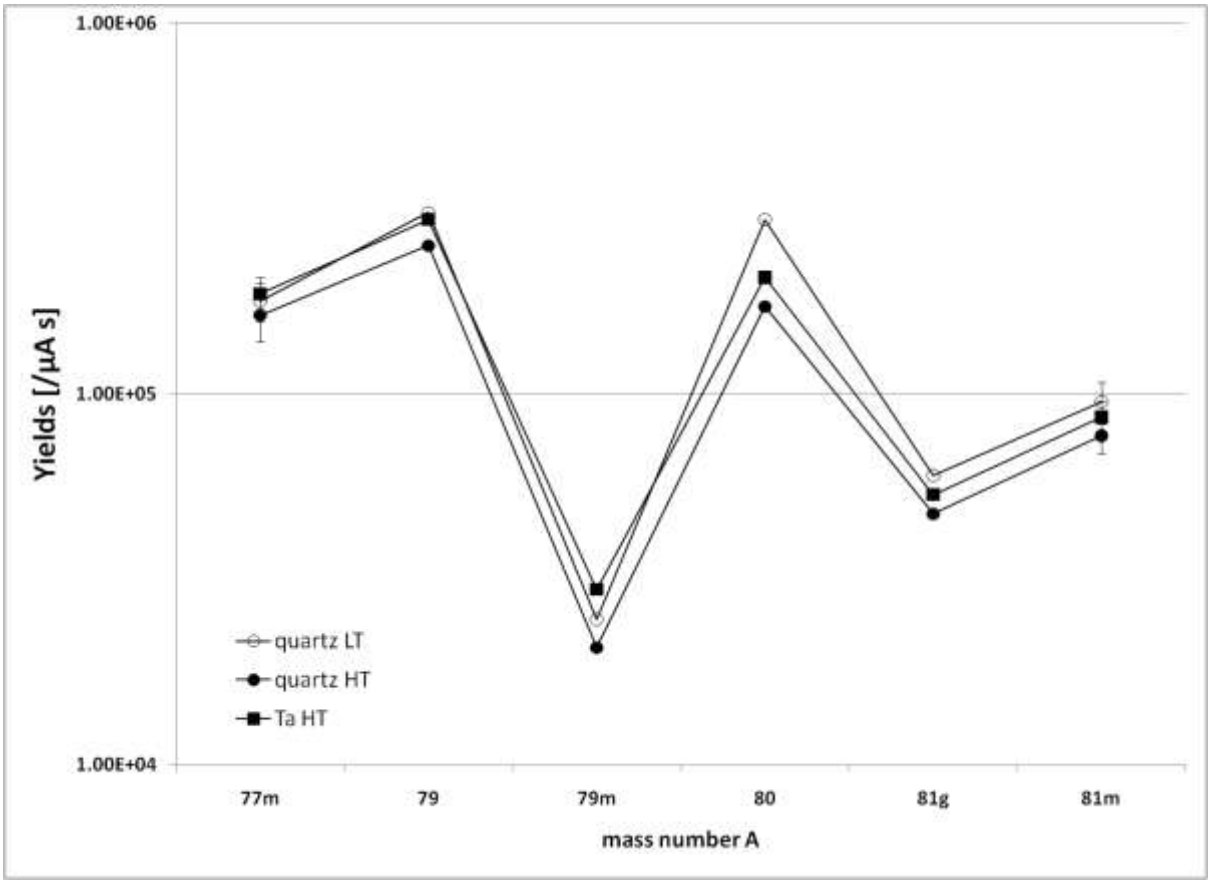

Fig 4.8: Ge yields from pressed-powder target

Sn was not detected in any of the yield measurements even though its production rates are up to 10^8 /s μA. This can only be explained by a greatly increased transport time at the lower transfer line temperatures employed.

When attempting to measure hold-up times with a stable beam, no Sn was observed with the sapphire tube inserted even at the maximum temperature (1150° C). Repeating the experiment with the bare Ta line, a ^{120}Sn current of 0.028 nA was detected on the Faraday cup. This corresponds to a system efficiency of 0.2%. The current was observed for 17 minutes with beam on target and continued to grow slightly. After the beam was removed the current dropped very slowly (see fig. 4.9). However, since the response of the system was very slow and the efficiency too low, no hold-up times could be extracted from this experiment. It can only be stated that the transport time in the Ta “high temperature” system, which is the only one that allows any release within an observable timescale, is very long. Any radioactive nuclides with half-lives shorter than an hour are not likely to be released.

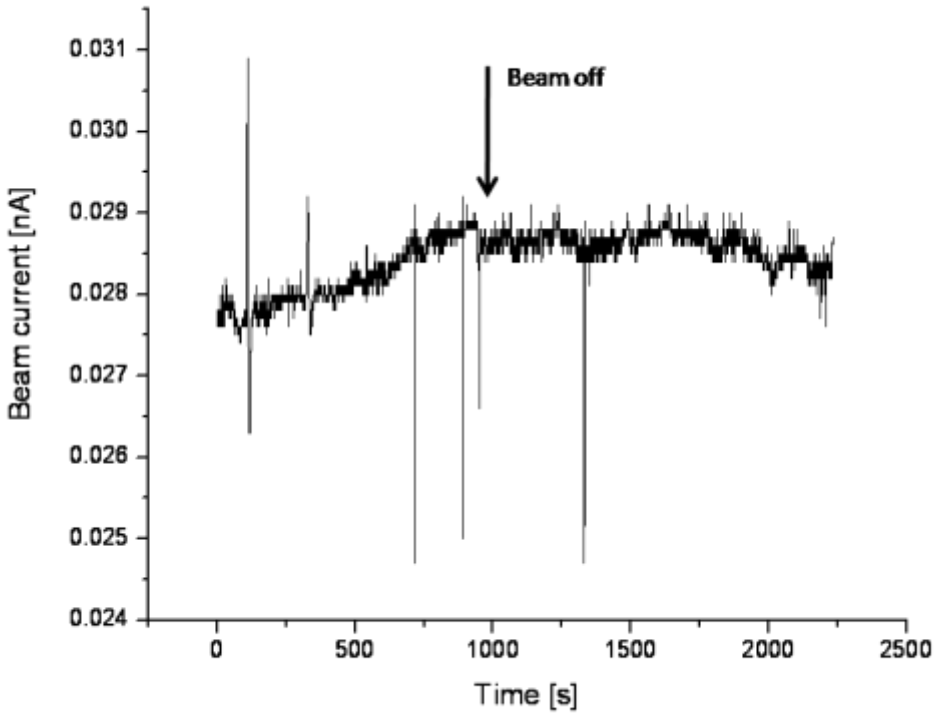

Fig. 4.9: Hold-up behavior of ^{120}Sn on high temperature Ta

Summary

The two measured group 14 homologues do not show similar behavior. Ge is not influenced by the changes in temperature or material. Sn, on the other hand, is very sensitive to both the change in temperature (since it is not seen in yield measurements on high temperature Ta) and material (since it was not released at all in hold-up experiments with tubes inserted). At this point no explanation for these differences in adsorption behavior can be found.

Ge beams could be purified by reduction of transfer line temperatures or introduction of a quartz surface.

The strong dependence of Sn release on surface temperatures must be kept in mind whenever designing TIS systems for beams of this element; if necessary, Sn contaminants could easily be removed by a reduction of temperature and/or change of surface material.

4.1.1.5 Results and Discussions: Selective Adsorption – Halogens

Of the halogen group, yield measurements were performed for Br and I. Stable beam hold-up times were measured for Br.

Br could not be detected in the yield measurements under any of the applied conditions. Since it is released easily under normal transfer line conditions, it can be speculated that a Ta bromide compound is formed at lower temperatures which dissociates in the normal setup. The HSC Chemistry 5.1 code (HSC chemistry) shows only the existence of gaseous $TaBr_5$ at a pressure of 10^{-8} bar up to 700° C (see fig. 4.10). This could be formed in a cold area of the transfer line although it should break up when reaching the ion source region. Since it is gaseous, it would not slow the release *per se*, but if the molecule does not completely break up in the ion source the Br would be found at a different mass (A_{sep} = A(Ta) + xA(Br)). It is not known whether there are other Ta bromide compounds existing under those conditions that could explain the slow release even at the maximum line temperature applied.

The hold-up data for stable Br confirm the very slow release out of this TIS (see table 4.9). Only with the transfer line at maximum temperature could any release of Br be detected. Unfortunately, due to degradation of the stripper foil in the tandem, the Br beam could not be kept at a stable intensity long enough for the release to reach equilibrium (see fig. 4.11). Therefore the numbers extracted from these measurements are only approximations and could not be used to extract adsorption enthalpies. It does appear that there is an additional chemical interaction between Br and quartz, since it considerably slows down the average release time compared to Ta.

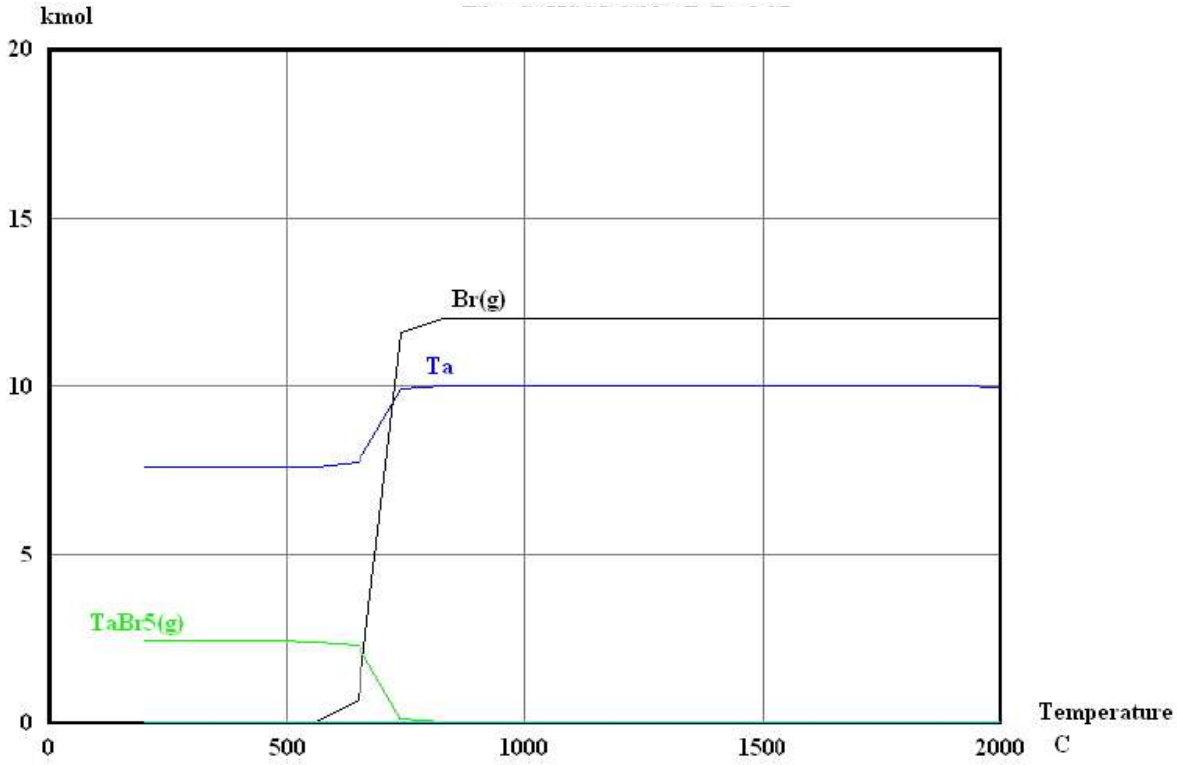

Fig. 4.10: Equilibrium composition of the Ta-Br system at 10^{-5}mbar, from 200 to 2000° C

Table 4.9: Average hold-up time behavior of Br on Ta and quartz

Line conditions	Ta HT	Quartz HT
Hold-up time (s)	4894.9 ± 6.3	9249.1 ± 73.9

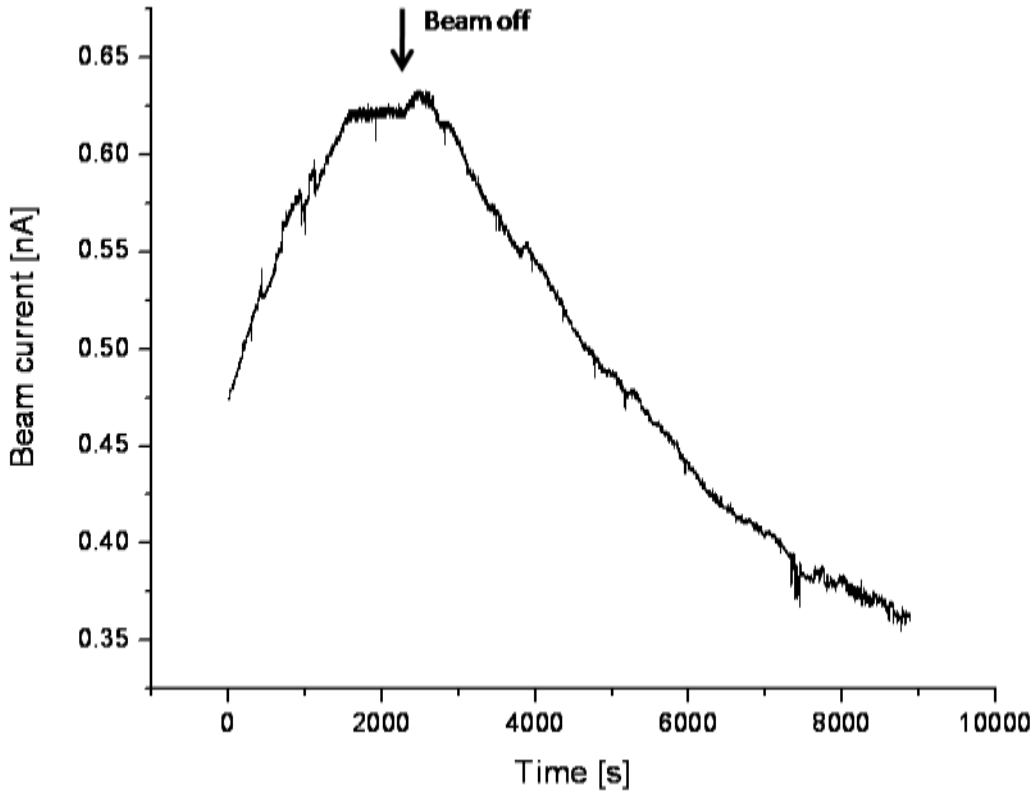

Fig. 4.11: Hold-up behavior of ^{79}Br on high temperature Ta

For I, yield measurements were conducted for two masses, 138 and 139. On mass 138 ($t_{1/2}$=6.5s) all yield measurements are identical within their uncertainties and in a normal range for yields from UC_x targets. On mass 139 ($t_{1/2}$ = 2.3s), no I was detected at all. These results are inconsistent since some suppression at the longer half-life should be visible if the interaction was strong enough to completely suppress the 2.3 s half-life. The HSC code shows only a narrow temperature range (200-400° C) for the existence of TaI_5 (see fig. 4.12). Therefore the faster release of I as compared to Br, shown by the observation of ^{138}I, is consistent.

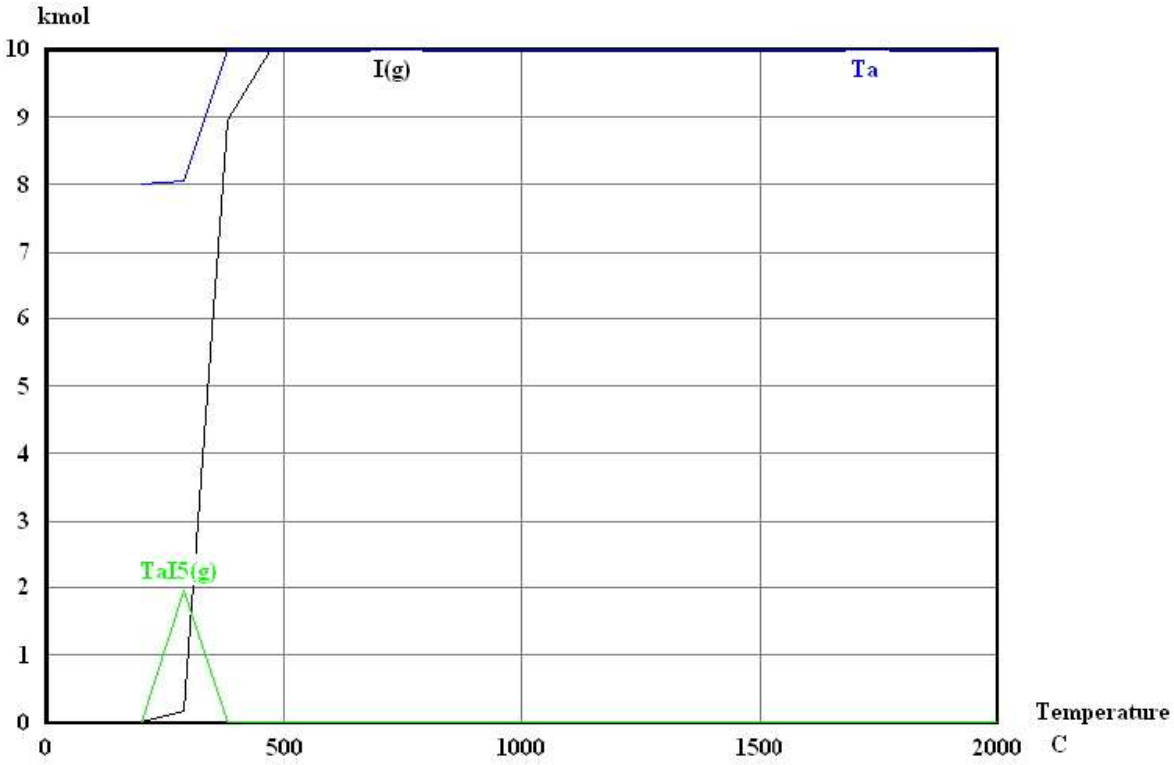

Fig. 4.12: Equilibrium composition of the Ta-I-system at 10^{-5}mbar, from 0 to 2000°C

Summary

Br exhibits a very strong temperature dependence in its interactions with Ta surfaces, hinting at a chemical reaction rather than a simple adsorption-desorption equilibrium. The interaction with quartz seems to be even stronger than the one with Ta, although the temperature dependence of this could not be investigated. Both these facts could be used to remove Br contaminations from other beams. The unusually strong effect of cool Ta surfaces must also be kept in mind when optimizing systems for Br release.

The results obtained for I are very inconsistent and no explanation has been found. Further investigation is needed to determine whether I shows a similar behavior as its homologue.

4.1.1.6 Results and Discussion: Selective Adsorption - Noble gases

Noble gases are not suited for TC since they do not interact with surfaces within the temperature range investigated here. Also, a well-defined sample could only be prepared by implantation of a noble gas beam in a sample foil. Therefore no measurements have been done with this method. For both Kr and Xe, radioactive yields were determined, in the case of Kr both from a pressed-powder and a graphite fiber target. For Kr, hold-up data with a radioactive beam were collected as well, since no stable beam can be delivered from the tandem accelerator. The noble gases' yields can be used as a benchmark, since they do not interact chemically and therefore should not be influenced by temperature and/or material changes in the transfer line. Thus the noble gases show the most extreme example of diffusion-controlled release time.

As expected, Xe yields are the same for all transfer line conditions applied (see fig. 4.13). Therefore it can be assumed that, on average, the efficiency of the TIS did not change while these experiments were run.

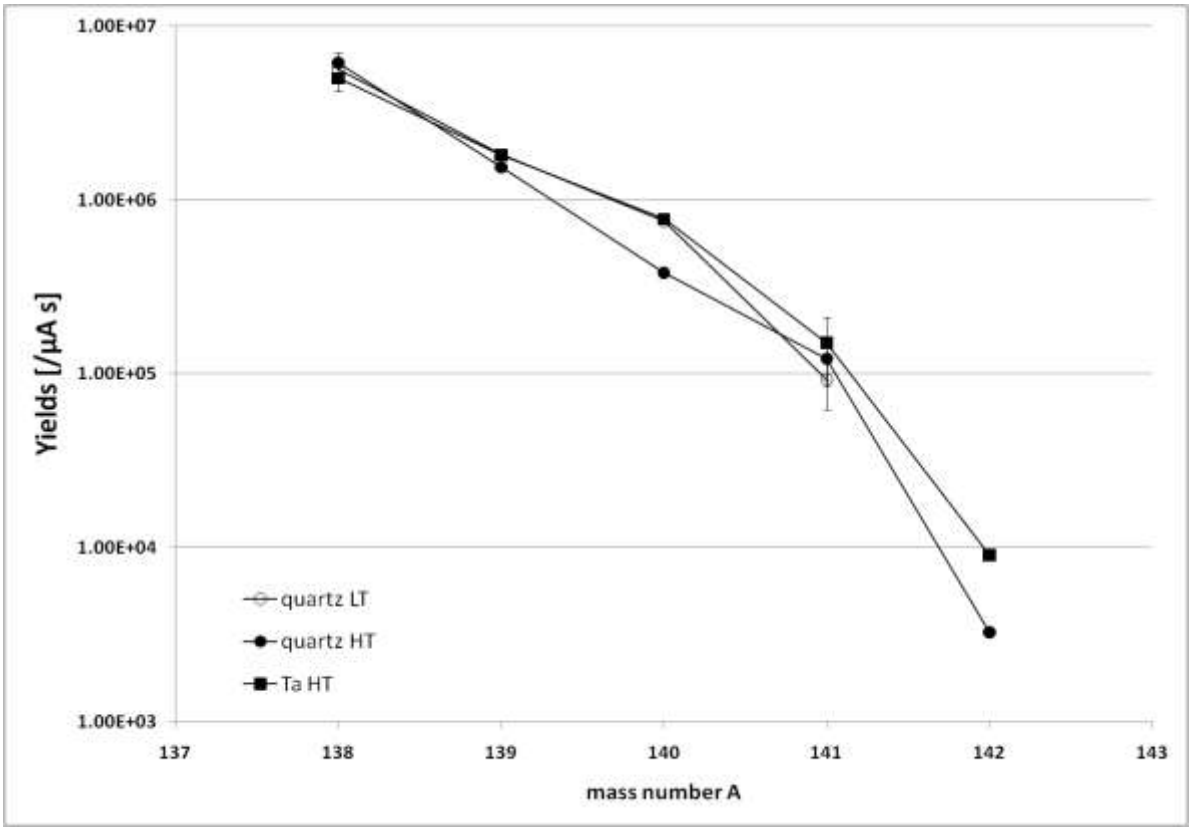

Fig. 4.13: Xe yields from pressed-powder target

Kr yields are also not influenced by the transfer line conditions; all results being identical within the uncertainties (see fig. 4.14). However, these values were

changed significantly when changing to UC_x/Ir coated graphite fiber targets (see fig. 4.14). Yields were reduced by a factor of approximately 10 for the longest half-life (189s), up to a factor of 20 for the shortest half-life measured (1.29s). However, because of the different concentration of materials used in the target, it is not certain that the production rates in the target are identical. The contribution of the Ir layer in the fiber target to the stopping power is likely to lead to a reduction of uranium fission products. Therefore only the relative suppression ratio from the longest to the shortest half-life measured (factor 2) was used in the analysis. This dependence of the yield reduction on the half-life strongly suggests an increased release time in the fiber target. This can be explained by longer diffusion times in the 60 µm diameter graphite fibers as opposed to the approximately 3 µm diameter grains of the pressed-powder target. Since Kr release is completely diffusion-controlled, the additional surface area present in the pressed-powder target should not contribute noticeably to the release time.

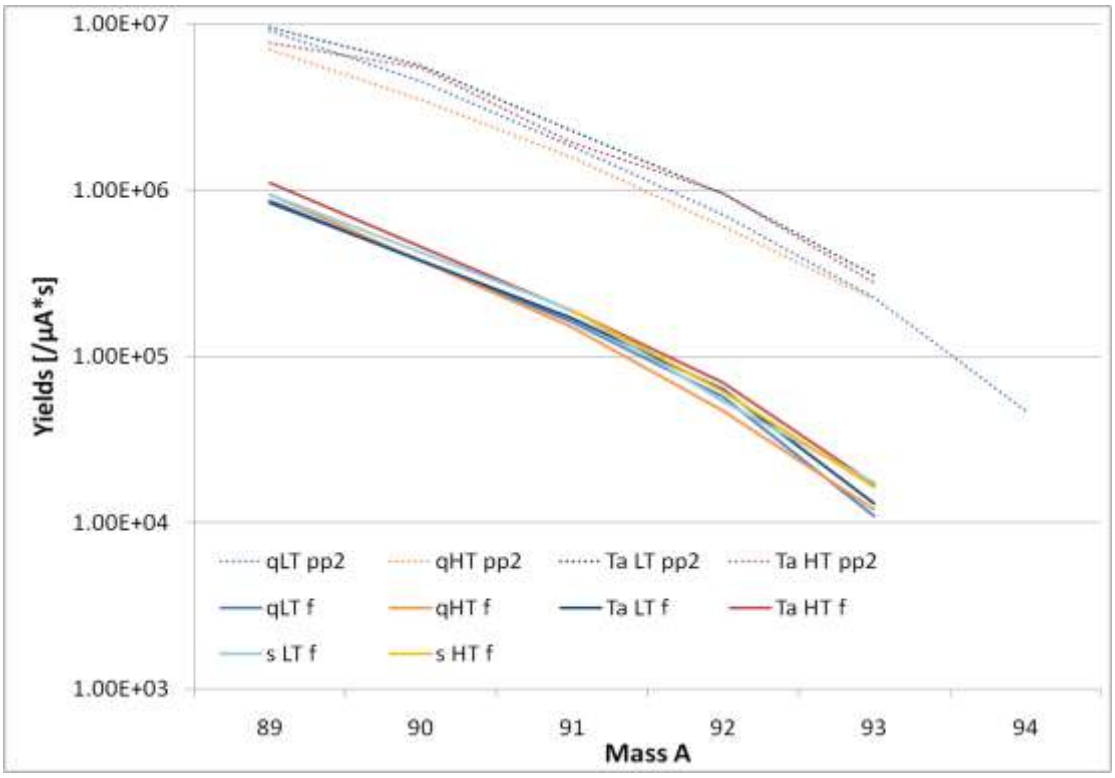

Fig. 4.14: Kr yields from pressed-powder and graphite fiber targets under different transfer line conditions

To investigate the pronounced difference of yields, hold-up time measurements were done with radioactive Kr from both the pressed-powder and the graphite fiber targets (see table 4.10, fig. 4.15). The short component (T_1) is considerably shorter for the

pressed-powder target; however, it was not immediately clear whether the average release time for the pressed-powder targets was shorter as well, since in the case of the hold-up time measured with the pressed-powder targets a second component could not be determined directly. Therefore an attempt was made to determine hold-up parameters via a second method, namely by fitting the yields obtained according to the model by Spejewski (see chapter 3.2.3). These fits all yielded a very high A_1/A_2 ratio, indicating that the second component has virtually no influence on the release times; this yields an average hold-up time $T_{average}$ equal to the short component T_1.

Table 4.10: Direct hold-up time measurements of Kr from pressed-powder and fiber targets

Target material	T_1 (s)	T_2 (s)	$T_{average}$ (s)
UC_2/C pressed powder	2.67 ± 0.36	N/A	2.67 ± 0.36
UC_x/Ir coated graphite fiber	37.79 ± 0.04	169.86 ± 0.05s	70.09 ± 0.07

Therefore it can be stated that the average release time of Kr is substantially increased when using graphite fiber targets instead of pressed-powder targets.

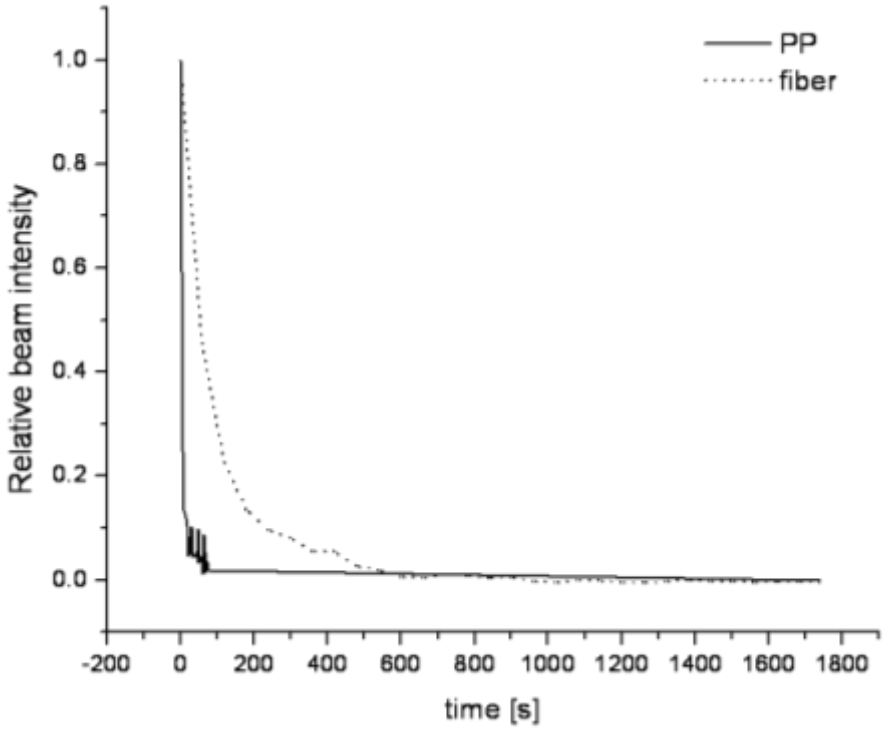

Fig. 4.15: Comparison of Kr hold-up times from pressed-powder and fiber targets

Summary

As expected the noble gases' interaction with the surfaces are very weak and no dependence on temperature or material could be detected.

For Kr, a strong dependence of the release time on the target material was found. Diffusion is considerably faster in the small grains of the pressed-powder target. Therefore the shape of the target material can be used to increase or decrease Kr production yields, depending on the experimental needs.

4.1.1.7 Results and Discussion: Selective Adsorption - Alkali metals

It has been reported by the ISOLDE group that quartz surfaces lead to a strong suppression of surface-ionized alkali metals out of a laser ion source, reaching suppression ratios of up to 50,000 for Rb, 600 for Cs, 230 for Li and 80 for K (Bouquerel, 2008). The fast diffusion of alkalis in quartz glass by breaking up the amorphous network is well documented in the literature (Ingram, 1992) (see chapter 2.4).

The elements K, Rb and Cs were investigated with the TC method. Yields and hold-up parameters were determined for Rb. Since the hold-up times extracted for Rb for a given material are the same within their uncertainties, no adsorption enthalpies could be determined.

Thermochromatography

The TC experiments on Rb were done with a carrier-free sample (implanted at ISOLDE), Cs both with a carrier (produced at the TRIGA reactor) and carrier-free and K with a carrier only. For the experiments with alkali samples containing a carrier, the distribution on the column was typically very broad, not allowing the extraction of a precise adsorption enthalpy.

Carrier-free Cs is deposited in several peaks along the line (see fig. 4.16a), the first one slightly below the sample foil. The deposition temperatures and peak widths are influenced by the inert gas flow. When adding a carrier, Cs is distributed very broadly along the thermochromatographic column at temperatures below 650° C (see fig. 4.16b). There seems to be a surface saturation effect that decreases the interaction of Cs with the quartz surface and leads to its deposition at lower temperatures.

a)

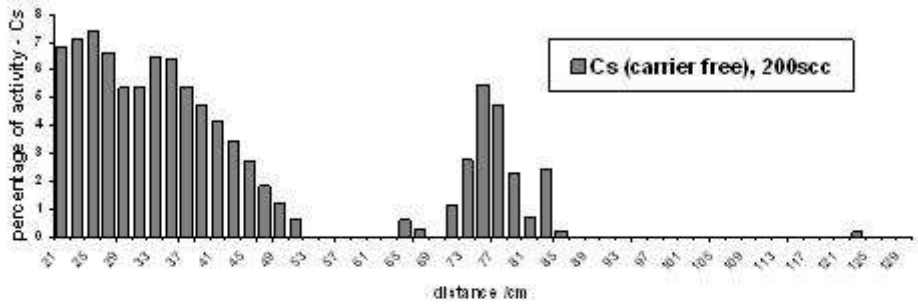

b)

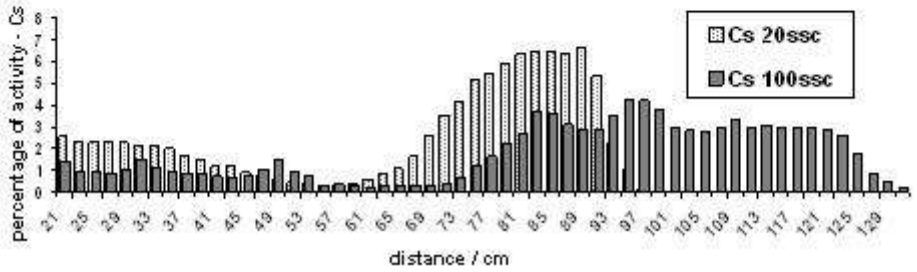

Fig. 4.16: Carrier-free Cs (a) and Cs containing a carrier on a quartz column

K (with carrier) forms a broad peak from the sample foil down to 700°C, with a tail down to 100°C (see fig. 4.17). In these experiments the gas flow was not varied. It can be assumed that a saturation effect similar to Cs is taking place but, because of the smaller atomic radius and stronger interaction of K, the deposition zone is shifted to higher temperatures.

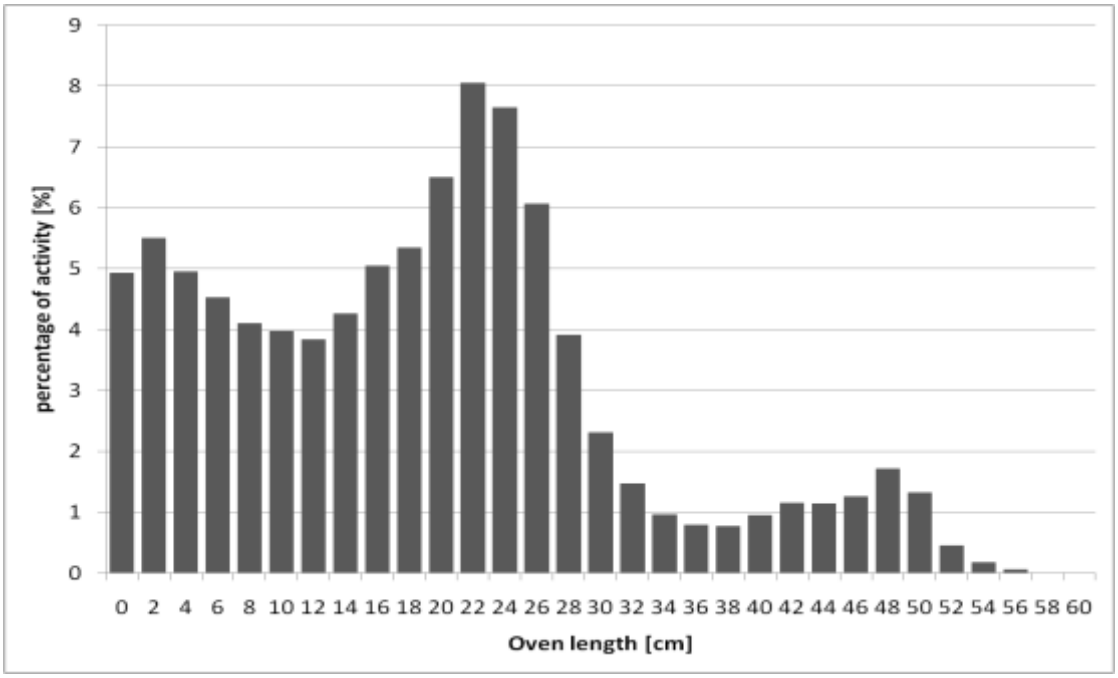

Fig. 4.17: Thermochromatogram of K on quartz with Mainz gradient oven

The carrier-free Rb shows the strongest interaction with the quartz surface, immediately sticking to the quartz surface at the maximum temperature with only a slight tail towards lower temperatures. The width of this tail is influenced by the inert gas flow. The calculations according to Eichler (see chapter 3.1, Schaedel, 2003) yield a lower limit for the adsorption enthalpy of -284 kJ/mol, assuming that the Rb peak did travel an infinitely small distance. This strong interaction even at higher temperatures (1200° C) does not seem to be consistent with any release online; however, assuming a similar behavior as that exhibited by its homologues K and Cs in the presence of a carrier, it seems possible that a saturation effect would take place. This would lead to a distribution of Rb along the transfer line, with sufficient mobility of the atoms even in the temperature range between 500 and 700° C. The number of atoms necessary to saturate the surface cannot be determined but must lie somewhere between the numbers used in carrier-free and carrier-containing samples. The actual values for these numbers are given in table 4.11, along with the sum of produced Rb atoms per second per 50 nA from a UC_x target. Since the number of produced atoms is higher than the number of carrier-free Rb in the TC experiments but lower than the number of K or Cs in the carrier-containing samples, a (partial) saturation of the surface may occur. Another reason for a faster distribution of the Rb online can be found in the absence of a carrier gas as used in the TC experiments. Atoms diffusing in vacuum have a much longer mean free path and thus experience fewer interactions with the wall surface.

Table 4.11: Number of alkali atoms introduced to quartz line in TC and online

Element, form	K, with carrier	Cs, with carrier	Rb, no carrier	Rb, online (per sec)
Number of atoms	1.54E18	9.08E15	7.25E05	1.75E08

Yields

Yield measurements on Rb and Cs were attempted, using the pressed-powder targets. Unfortunately, due to the high production of Kr and Xe, most yield values, after correction for the parent decay, were zero within their uncertainties. Therefore, measurements of Rb yields and hold-up times were repeated using a graphite fiber target (see table 4.12). For the yields measured at mass 89, the uncertainties in the data are still very large, resulting from a high yield of ^{89}Kr. Only the upper half of the error bars could be shown since the lower half extends below zero, which cannot be plotted in Excel.

After correction for the decay of Kr, the Rb yields show considerable dependence on the transfer line temperature and material (see fig. 4.18). The Rb yields are strongly suppressed by the quartz surface, both for high and low temperatures, reducing the yields by factors of 12 and 19, respectively, compared to the high temperature Ta data.

These results are not entirely consistent with the ones obtained at ISOLDE. Assuming an exponential behavior of the yields with the inverse of the transfer line temperature as has been documented at ISOLDE for Rb, extrapolation to 300° C predicts a suppression factor of 1745 relative to Rb yields from a standard TIS. The reason for the difference in the reduction of yields may lie in the fact that at ISOLDE a laser ion source was used instead of a plasma ion source (see chapter 4.1.3 for discussion of effects on surface ionization). Another reason might be differences in the quartz material used (see chapter 4.1.3).

Both on Ta and sapphire there is a temperature dependence of the yields as well. The sapphire yields are lower than the Ta yields by a factor of 2-3. The sapphire low temperature results are very similar to the ones taken with quartz at high temperature. These results show that the interaction of Rb with Ta at lower temperatures is not negligible, *e.g.* in cooler regions of the TIS. The interaction strength of Rb with sapphire can be explained by a reaction similar to that believed to occur in quartz, *i.e.* a break-up of the aluminum-oxygen bonds. Because of the crystalline structure of sapphire as opposed to the amorphous quartz glass, diffusion into the structure is hindered. Therefore the Rb will mostly stay at the surface of the

sapphire, leading to a stronger saturation effect and thus a weaker interaction of the sapphire with Rb in general.

Except for Ta, the data do not show an effect of the half-lives of the nuclides measured, that is, no stronger suppression at shorter half-lives (see fig. 4.18b). This is not consistent with a reversible adsorption-desorption equilibrium leading to a longer transport time and thus higher suppression at shorter half-lives. It does support the theory of an irreversible reaction on the surface or diffusion into the bulk, with a saturation effect to allow for the release of a fraction of the Rb produced.

Table 4.12: Yields of Rb from fiber target

Nuclide	Half-life (s)	Yields (/s μA)					
		Ta HT	Ta LT	quartz HT	quartz LT	sapphire HT	sapphire LT
^{89}Rb	909	5.61E+05	3.11E+05	8.64E+04	0.00E+00	0.00E+00	3.10E+04
^{91}Rb	58.6	5.44E+05	7.68E+05	6.48E+04	1.09E+04	1.32E+06	1.33E+05
^{93}Rb	5.84	1.52E+05	3.77E+04	6.49E+03	2.88E+03	7.74E+04	1.27E+04
^{94}Rb	2.7	4.17E+04	8.82E+03	3.58E+03	2.20E+03	1.96E+04	4.46E+03

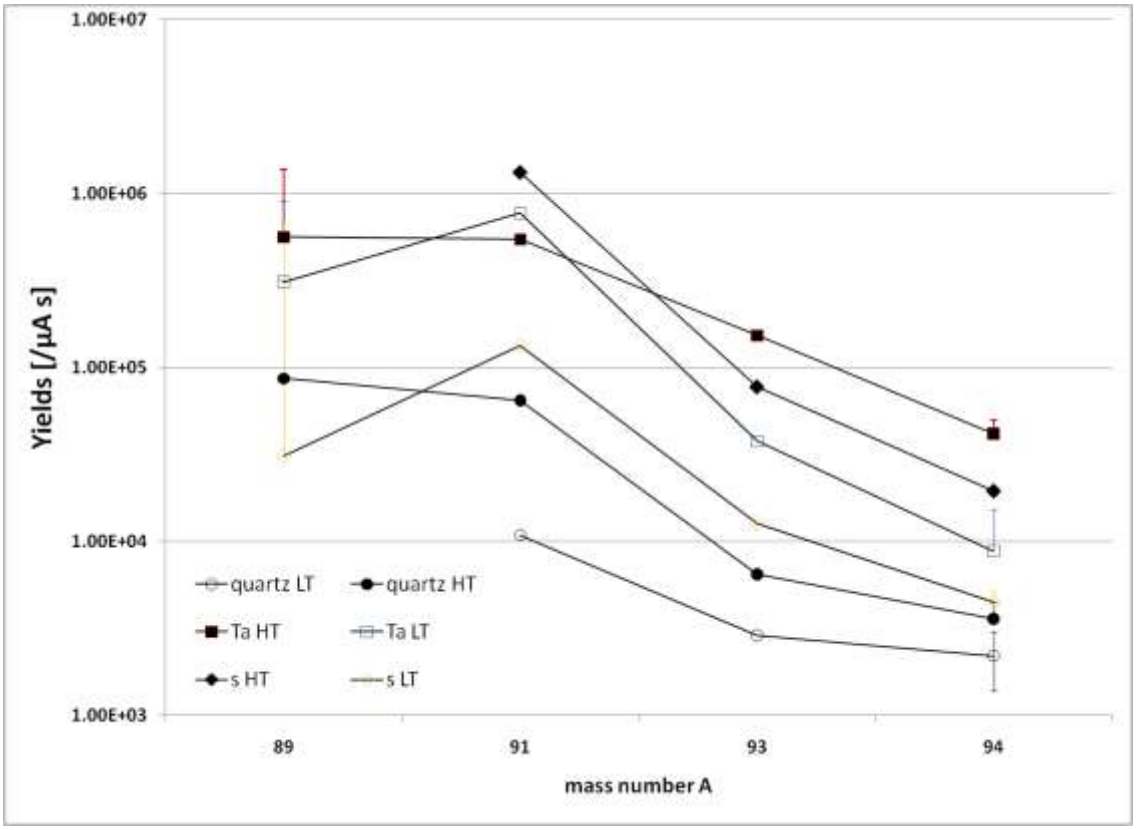

Fig. 4.18a: Rb yields from graphite fiber target. Only the upper half of the error bars are shown since the lower half extends below zero.

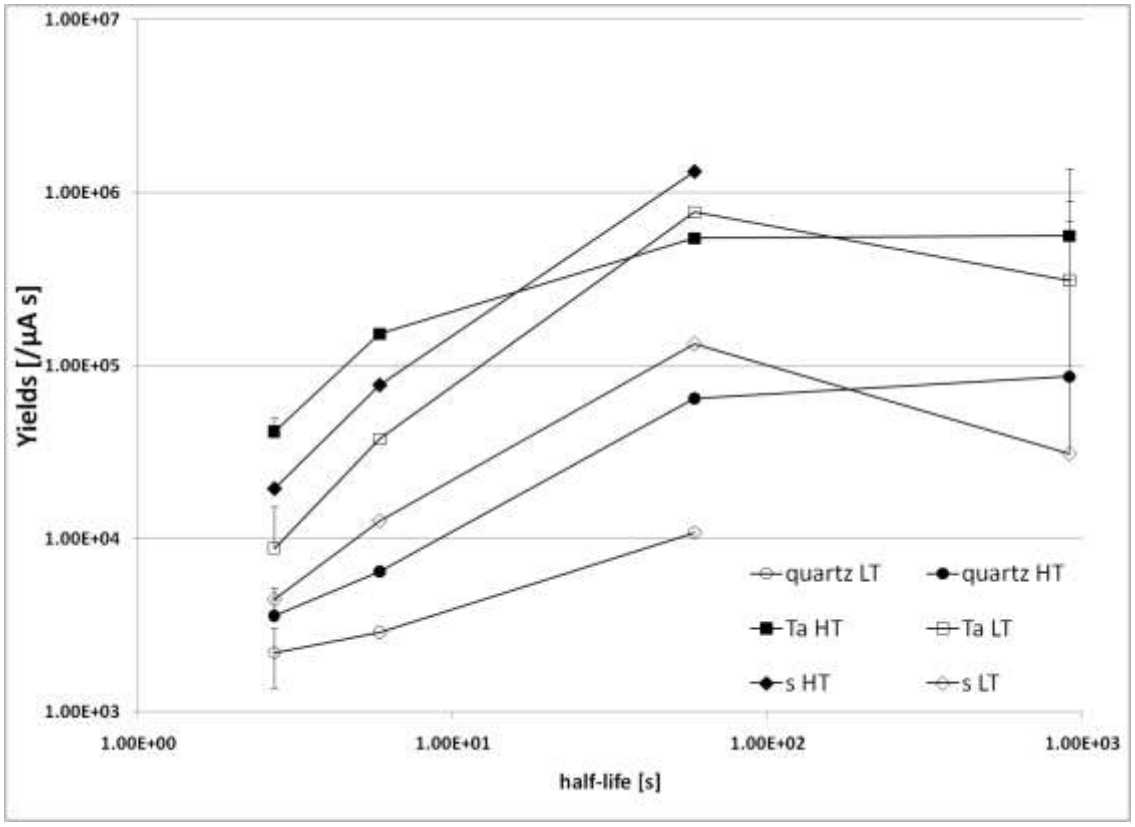

Fig. 4.18b: Half-life dependence of Rb yields from fiber target

Hold-up times

To investigate further into the mechanism of Rb suppression, hold-up times of radioactive Rb out of the graphite fiber target have been measured (see fig. 4.19). These are very long (see table 4.13), although whether this is due to long diffusion times or strong interaction with the surface material cannot be determined from the data. Unfortunately, due to the high amount of Kr present, especially with beam on target and shortly after turning off the beam (see fig. 4.19), the uncertainties in the hold-up times are very large (see table 4.13), ranging from 27 to 74%. Therefore, it is not possible to determine the effects of the transfer line temperature and material, and no adsorption enthalpies for Rb could be extracted. It can be stated, however, that, even allowing for the maximum error, the differences in hold-up times are not sufficient to explain the suppression of Rb observed in the yield measurements (see table 4.14). This again hints at an irreversible chemical effect as opposed to an adsorption-desorption equilibrium, since atoms that are not released (before their decay) will not show up in the release curves at all and will therefore have no influence on the hold-up times thus determined. This supports the theory of a chemical reaction of Rb with the quartz surface, eventually diffusing into the volume. A fraction of the Rb atoms will not react, only impinge on a non-reactive location or be blocked by other atoms already adsorbed on the surface. These atoms will be released from the line and observed.

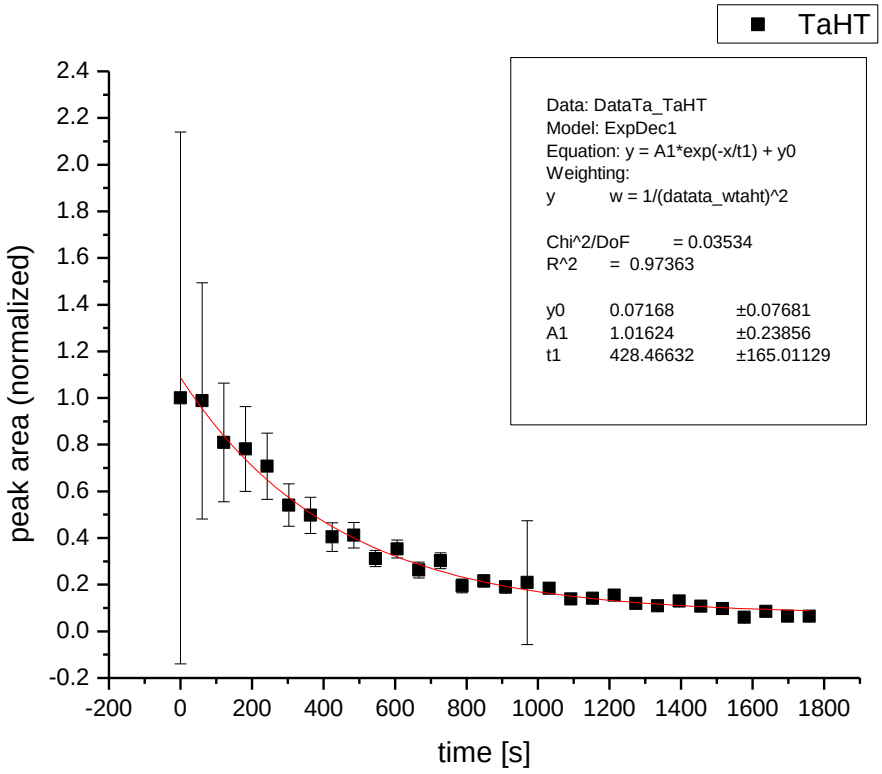

Fig. 4.19: Hold-up curve of Rb on Ta, high temperature

Table 4.13: Hold-up parameter for ^{89}Rb

conditions	A_1	error	T_1 (s)	error	**Holdup time T (s)**	**error**
Ta LT	1.45	0.28	432	131	**446**	**203**
Ta HT	1.02	0.24	428	165	**441**	**252**
s LT	1.49	0.23	562	239	**682**	**508**
s HT	1.17	0.12	374	72	**363**	**98**
q LT	3.98	0.33	546	90	**648**	**183**
q HT	1.01	0.05	557	91	**671**	**191**

Table 4.14: Comparison of yield ratios for ^{93}Rb, experimental and predicted from hold-up times

^{93}Rb	experimental	Predicted from HU time	Predicted from HU time (using maximum error)
Yield ratio TaHT/qLT	22.12 ± 0.03	1.47 ± 0.05	3.72 ± 0.10

Summary

All alkali metals exhibit a strong interaction with quartz although it appears to decrease with atomic mass / size. This interaction is no simple adsorption-desorption equilibrium since the behavior in TC experiments does not correspond to the model: they are not deposited in discrete peaks and the influence of the gas flow on the deposition temperature is too strong, resulting in different adsorption enthalpies for varying gas flows. Also, the yield suppression is not half-life dependent, as would be expected for a simple increase of effusion time.

There is also a saturation effect of the quartz surface that leads to a broad distribution of the alkalis over the quartz surface. This effect explains why the lighter alkalis can be released from a quartz transfer line, even at low temperatures.
The results gained from the Rb hold-up time measurements are consistent with an irreversible chemical reaction or adsorption on quartz surfaces that leads to the complete loss of a fraction of the Rb produced. The yield suppression, however, is not as big as the one observed at ISOLDE, suggesting some other effect in addition to the chemical reaction.

Rb shows a similar behavior on sapphire, although the interaction is not as strong. This is consistent with the less open structure of the alumina compound.
The behavior of Rb on Ta corresponds to that expected of a reversible interaction since there is a half-life dependence of the adsorption. However, because of the high uncertainties in the data, no information on the temperature dependence of this interaction could be extracted.

The strong interaction of alkali metals with quartz surfaces can be used to reduce them as a contaminant in other beams. The relatively long sticking times of Rb on low-temperature Ta must be kept in mind when trying to design systems for fast Rb release.

4.1.1.8 Results and Discussion: Selective Adsorption - Sr

There could be no information found in the literature about adsorption enthalpies of Sr on high-temperature quartz or sapphire surfaces. ISOLDE reports a suppression factor of 250 for ^{96}Sr ($t_{1/2}$ = 1070 s) when changing from a standard line to the water-cooled line (300° C) (Bouquerel, 2008).

Attempts were made to measure yields and their dependence on transfer line temperature and materials. After correcting for both Kr and Rb decay, the experimental uncertainties in the data are very high. For some measurements, yields

after correction are negative or zero. Therefore it cannot be determined whether the suppression factor agrees with results at ISOLDE. However, the fact that no Sr could be detected for the shorter lived nuclides measured with a quartz line seems to agree with a strong interaction of Sr with quartz surfaces.

4.1.2 Discussion of methods

The adsorption behavior of a number of elements has been investigated using three different methods: Thermochromatography, yield and hold-up time measurements.

Thermochromatography is an offline method and allows for more control of parameters than can be achieved online, especially the number of elements present and their amounts. Therefore it has been very useful to investigate the influence of reactants in the atmosphere (O_2, H_2O) and to learn about saturation effects of the surface.

Models (thermodynamic and Monte Carlo) assuming simple adsorption-desorption equilibrium can be used to determine adsorption enthalpies from deposition temperatures (see chapter 3.2.3). For elements that fulfill this condition, adsorption enthalpies have been determined very precisely and show good agreement with values given in the literature and derived from hold-up time measurements. TC is also a good method to determine if an element shows a different adsorption behavior, since the dependence of deposition temperature and gas flow will not correspond to that given by the models.

For target-ion source development, TC is a good method to predict behavior of elements in the transfer line. However, it must be kept in mind that the absence of a gas flow, contaminations coming off the target, and the less precise temperature control online may change the results observed in offline experiments.

Yield measurements are the least time-consuming way of investigating the behavior of a number of elements on a given surface. They have been performed for all elements investigated herein (see table 4.15). These values directly show the yield suppression caused by change of temperature or material. The half-life dependence of the yield suppression contains information on the reversibility of the adsorption process.

Unfortunately, no enthalpies of adsorption can be extracted from yield measurements. Also, the method is less sensitive to changes in release times than hold-up measurements. This last point could be somewhat improved by using a TIS with a wider temperature range to increase the differences between high and low temperature measurements.

Table 4.17: Yields of the shortest-lived nuclide measured for each element on Ta and quartz surfaces

Nuclide	Half-life (s)	Yield Ta HT (/s μA)	Yield Ta LT (/s μA)	Yield quartz HT (/s μA)	Yield quartz LT (/s μA)
^{93}Kr	1.29	2.76E+05 ± 3.1E+04	3.07E+05 ± 3.8E+04	2.21E+05 ± 4.9E+04	2.25E+05 ± 7.6E+04
^{141}Xe	1.73	1.51E+05 ± 2.0E+04	n/a	1.22E+05 ± 7.3E+03	9.26E+04 ± 7.9E+03
^{78}Zn	1.47	3.03E+04 ± 5.0E+03	n/a	1.21E+04 ± 8.1E+03	3.19E+04 ± 5.2E+03
^{127}Cd	0.37	6.42E+05 ± 5.1E+04	n/a	6.25E+05 ± 7.1E+04	7.22E+05 ± 6.3E+04
^{81m}Ge	7.6	8.67E+04 ± 8.9E+03	n/a	7.71E+04 ± 8.2E+03	9.52E+04 ± 1.6E+04
^{81}Ga	1.22	6.34E+04 ± 7.9E+03	n/a	5.81E+04 ± 6.6E+03	6.87E+04 ± 9.1E+03
^{127}In	1.09	5.17E+06 ± 9.8E+05	n/a	2.11E+06 ± 5.5E+05	3.08E+06 ± 7.2E+05
^{120m}Ag	0.32	2.94E+06 ± 6.1E+05	n/a	1.48E+06 ± 3.0E+05	8.78E+05 ± 1.2E+04

Hold-up time measurements require either a stable beam of the element of interest or a way to produce sufficiently long-lived isotopes in the target, preferably with no or only short-lived parents feeding them, since corrections for parent decay introduce larger uncertainties.

Although more time-consuming than yield measurements they are more precise. Differences in release times down to a second or possibly shorter can be determined. Using the method of Spejewski (Spejewski E.H., 2008), measured hold-up parameters have been used to predict suppression in yields and the results are in good agreement with experimental findings. From the difference in release times under two different line conditions, adsorption enthalpies have been determined. The obtained results are very consistent with the values obtained from offline experiments.

In the case of elements being irreversibly adsorbed, hold-up time measurements alone are less useful, since this method only determines the release time distribution but not the absolute amounts of particles released. In the case of a material simply adsorbing a fraction of the atoms but not changing the release of the remaining

ones, hold-up time measurements would not show any effect of this material. However, in combination with yield measurements it can be used to gain more insight into the mechanism of adsorption.

All three methods tested for investigating adsorption behavior are consistent with each other and are useful for obtaining information for ion source development. Results from one method can be used to predict others.
None of the two online methods yields all the information available on adsorption behavior online. Instead, they complement each other, and it should be decided for each case which method is the most suitable.

4.1.3 Discussion of results from Oak Ridge vs. ISOLDE

The results obtained at Oak Ridge agree qualitatively with those by the ISOLDE group. However, the suppression factor observed is generally much smaller. The biggest differences are seen in Rb (see table 4.16, where the value for 300°C at Oak Ridge is extrapolated), followed by In. The suppression factor gained by changing the geometry and introducing the quartz at high temperatures are similar at ISOLDE (120) and Oak Ridge (189). When lowering the temperature of the quartz line, the effects reported by ISOLDE are much larger.

There are several possible reasons for this behavior, although none of them seems sufficient to explain the considerable difference in results.

Table 4.16: Yields, yield percentage and yield suppression for Rb measured at ISOLDE and Oak Ridge

Line temp. (°C)	Yield ISOLDE (Ions/μC)	Suppression factor ISOLDE	Yield OR (Ions/μA s)	Suppression factor OR
1800	1.8E08	**1**	6.8E05	**1**
1150	1.5E06	**120**	3.6E03	**189**
700	2.2E04	**8181**	2.2E03	**309**
300	3.3E03	**54545**	5.1E02 (extr.)	**1333**

a) Comparing different materials

The quartz glass used at ISOLDE was procured from a different producer. Variations in density, surface structure and contaminations may alter the adsorption behavior.

b) Comparing different geometries

With different relative heights of target and ion source extraction, the vertical part leading upwards from the target container is slightly longer in the Oak Ridge TIS unit. A cool spot in this region might lead to a reduction of yields, though whether this effect would be stronger at higher or lower line temperatures is difficult to estimate.

c) Comparing different absolute temperatures

The temperature gradient in the Oak Ridge transfer line, although basically a copy of the ISOLDE prototype #1 (“warm line”), differs, if slightly, from the one reported by ISOLDE. Because of the different heater design and more efficient heat shielding, the temperature in the middle of the line is higher in the Oak Ridge transfer line, creating a steeper gradient.

d) Comparing different temperature ranges

The suppression factors at ISOLDE are gained from comparing yields taken at the standard transfer line temperature (≈1800° C) to yields gained with a transfer line cooled down to temperatures between 680 and 300° C. Oak Ridge suppression factors (except those given in table 4.16 where yields from another TIS unit where used) compare the maximum temperature of the modified TIS (≈1150° C) with the lowest achievable temperature (≈690° C at coldest spot).

e) Comparing different ion sources

The experiments at ISOLDE were performed using a surface / laser ion source; all experiments at Oak Ridge used the EB plasma ion source. Lettry et al. (Lettry, 1998) report atoms being surface-ionized on the hot surfaces of the TIS unit. In another paper, investigations of extraction of ions created by laser ionization outside the extraction fields are presented (Lettry, 2003). These ions will slowly diffuse towards the extraction field, resulting in a broad peak in the release curve (see fig. 4.20).

This is assumed to be caused by a plasma that confines the produced ions and keeps them from being neutralized by wall collisions. This effect is still visible at a cavity temperature of 1270° C and disappears when the cavity is cooled down to 1170° C.

Assuming that surface ionization is indeed taking place in the transfer line of the TIS system, this will have different effects depending on to which ion source the transfer line is connected. For a surface / laser ion source, ions created before the actual ionization cavity can increase the overall ionization efficiency. For a plasma ion source, positive ions created in the transfer line will be repelled by the positive potential of the anode and not enter the ion source.

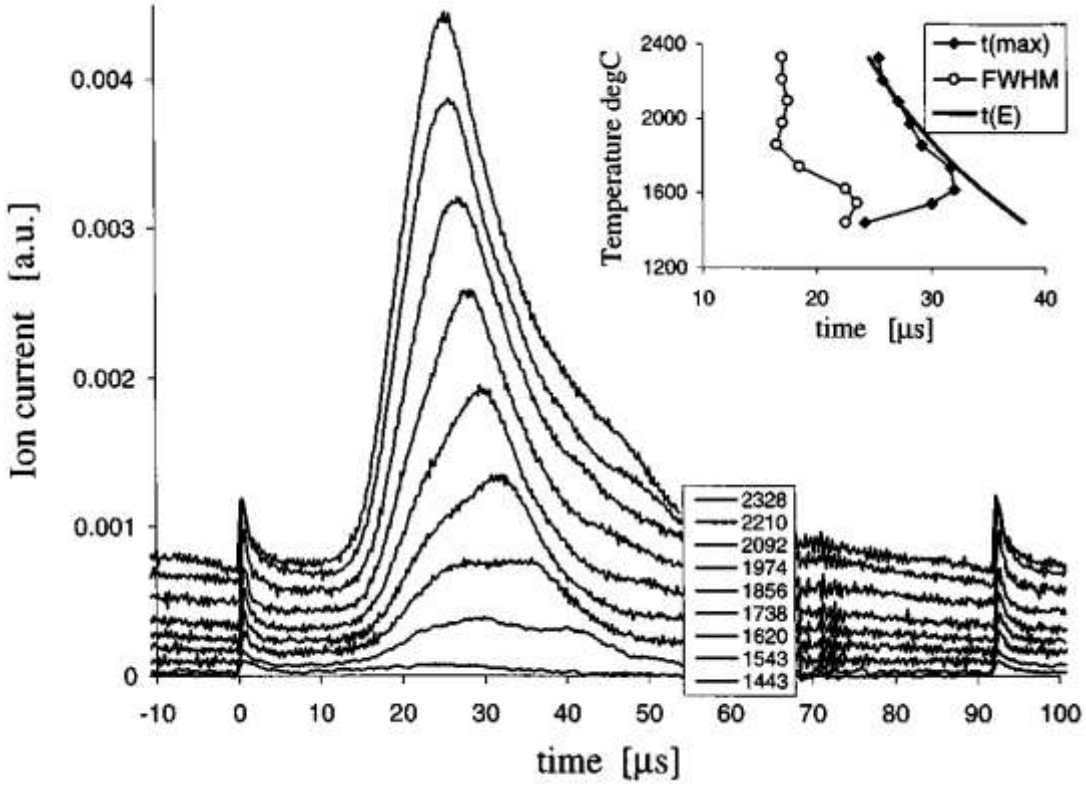

Fig. 4.20: Release curves of ^{65}Cu ions released from a 30 mm W cavity after the laser pulses for temperatures between 1400° C and 2300° C.

A reduction of the line temperature as well as the introduction of a surface with a lower work function (quartz) will reduce surface ionization in the transfer line. For surface ion sources, reduction of temperature will reduce the overall ionization efficiency of surface-

ionizing elements. In the case of a plasma ion source, the release efficiency of these elements could increase.

The suppression factors shown in table 4.16 suggest that the introduction of quartz and the change of geometry do not influence the surface ionization probability in the transfer line greatly, possibly because ionization has to take place close to the ion source to allow extraction of the created ions. The lowering of the temperature of the transfer line leads to a reduction of both surface ionization and the plasma confining the ions. In case of a surface ion source this would lead to a considerable suppression of surface-ionizing elements as has been observed by the ISOLDE group.

4.2 Spectroscopy

4.2.1 Motivation

The main goal for the ^{131}Cd experiment was the identification of the single-hole (SH) proton levels in the neutron-magic N=82 isotope ^{131}In. They are the only single-nucleon shell-model basis states around doubly-magic ^{132}Sn that are unknown by now. Of particular interest in this context are the depth of the $\pi\, f_{5/2}$ hole and the $\pi\, p_{3/2}$- $\pi\, p_{1/2}$ spin-orbit splitting. Theoretical agreement on these levels has not been achieved so far.

The evolution of the single-particle (SP) structure plays a crucial role in all calculations of nuclear properties of nuclides far from stability, where no experimental data are available.

4.2.2 Results

During the ISOLDE experiment IS393 in June 2006, data on mass 131 were taken for 44h with the laser on and for 16h without the laser. All “laser on” spectra were summed up as were all “laser off” spectra. Comparison of the data shows lines from the decay of ^{131}Cd and its daughters. The lines that were found to be present in the “laser on” but not the “laser off” sum spectra and could not be assigned to another nuclide are: 841keV, 2640keV, 3866keV and 6039keV. Sections from the spectra showing these lines are discussed below:

841keV

The line at 841keV (arrow) is only seen with the laser on (see fig. 4.21 and 4.22). The line at 858keV is from the decay of ^{129}Sn (half-life: 6min). Mass 129 had been used to check on the laser efficiency shortly before cycling back to mass 131. This left some residual activity in the tape station which decayed before the next “laser off” spectra were taken.

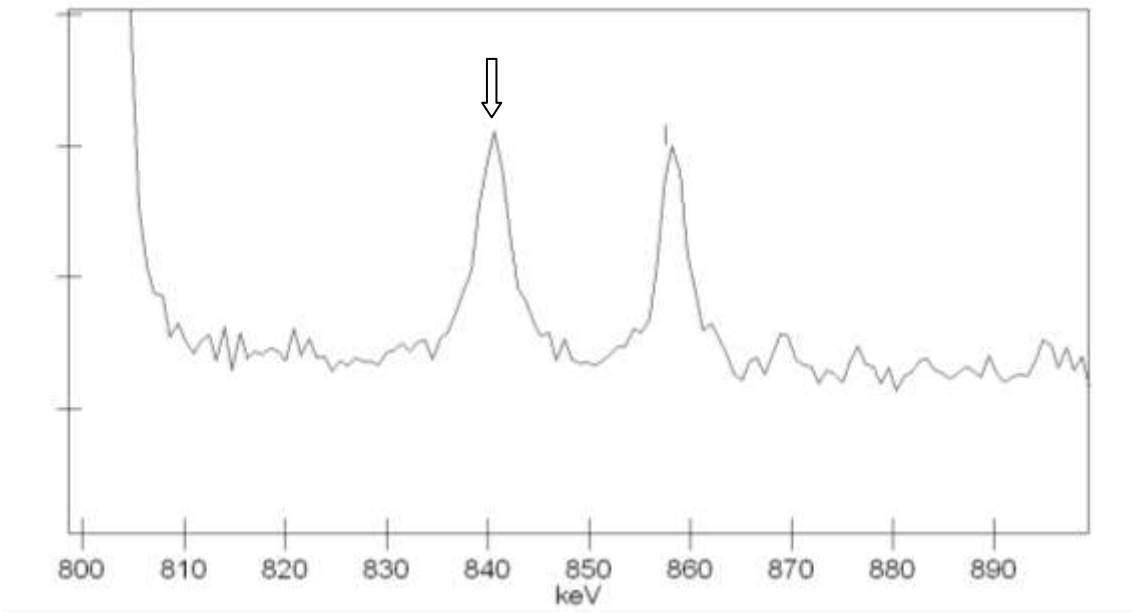

Fig. 4.21: Section of the “laser on” γ spectra on mass 131, 800 to 900 keV

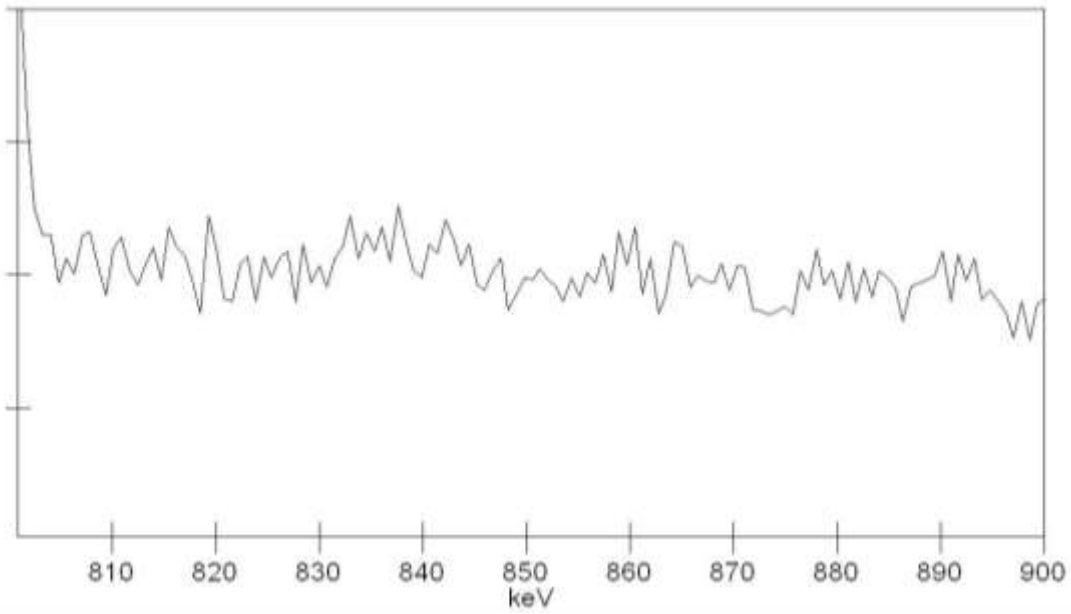

Fig. 4.22: Section of the “laser off” sum spectra on mass 131, 800 to 900 keV

2432keV

The line at 2432 keV (arrow, fig. 4.23) has been shown to be the main line in the decay of ^{131}In (Fogelberg, 2004). It is absent in the “laser off” spectra (fig. 4.24), proving that the medium temperature quartz transfer line suppresses the release of In from the TIS. It is present in the “laser on” sum spectra due to the decay of ^{131}Cd into ^{131}In and thus proof of the release of ^{131}Cd from the ion source.

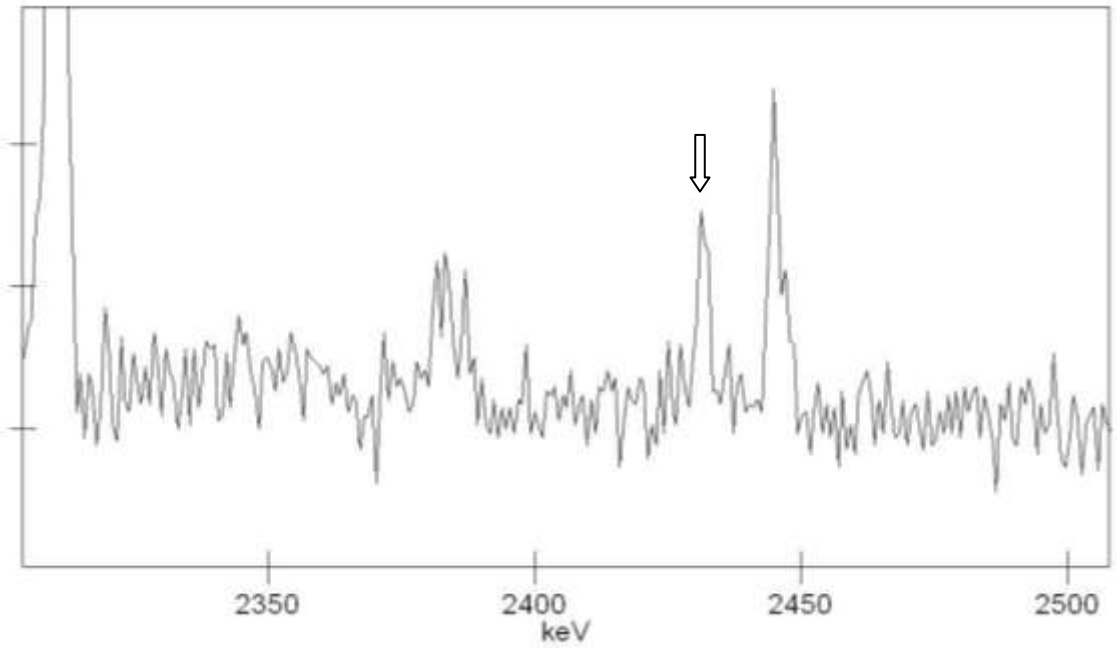

Fig. 4.23: Section of the “laser on” sum spectra on mass 131, 2300 to 2500 keV

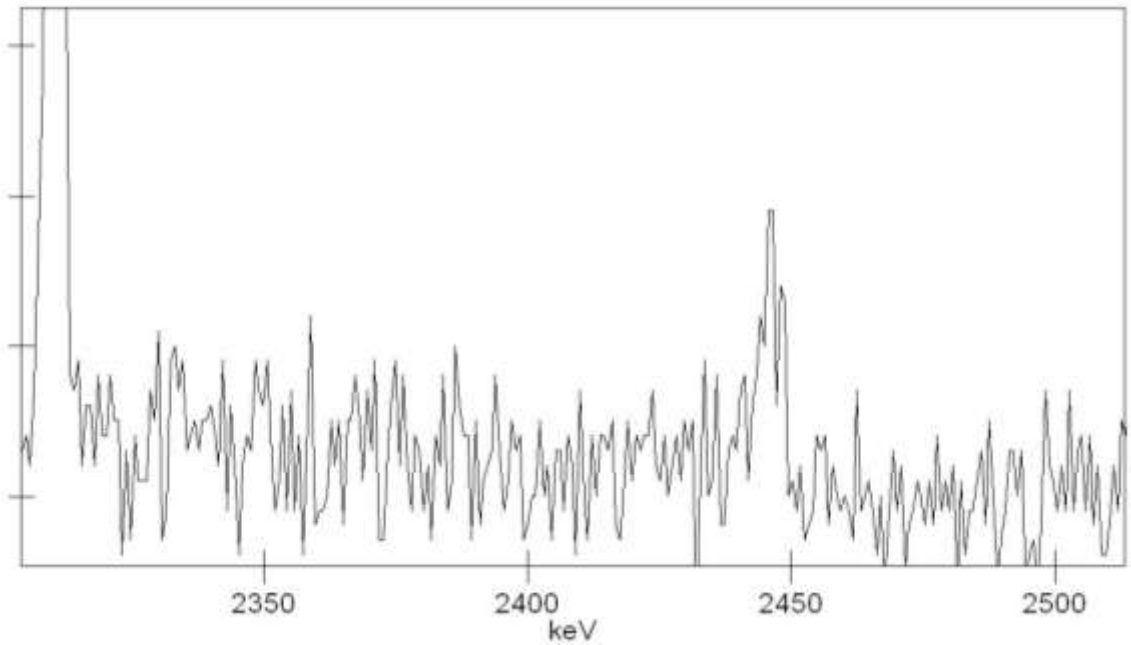

Fig. 4.24: Section of the “laser off” sum spectra on mass 131, 2300 to 2500 keV

2640keV

A low intensity line appears at 2640 keV with the laser on (fig. 4.25 vs. fig 4.26). It may not be visible in the “laser off” sum spectra due to shorter counting time. The line could not be assigned to any nuclide with a suitable half-life that could have been deposited on the tape.

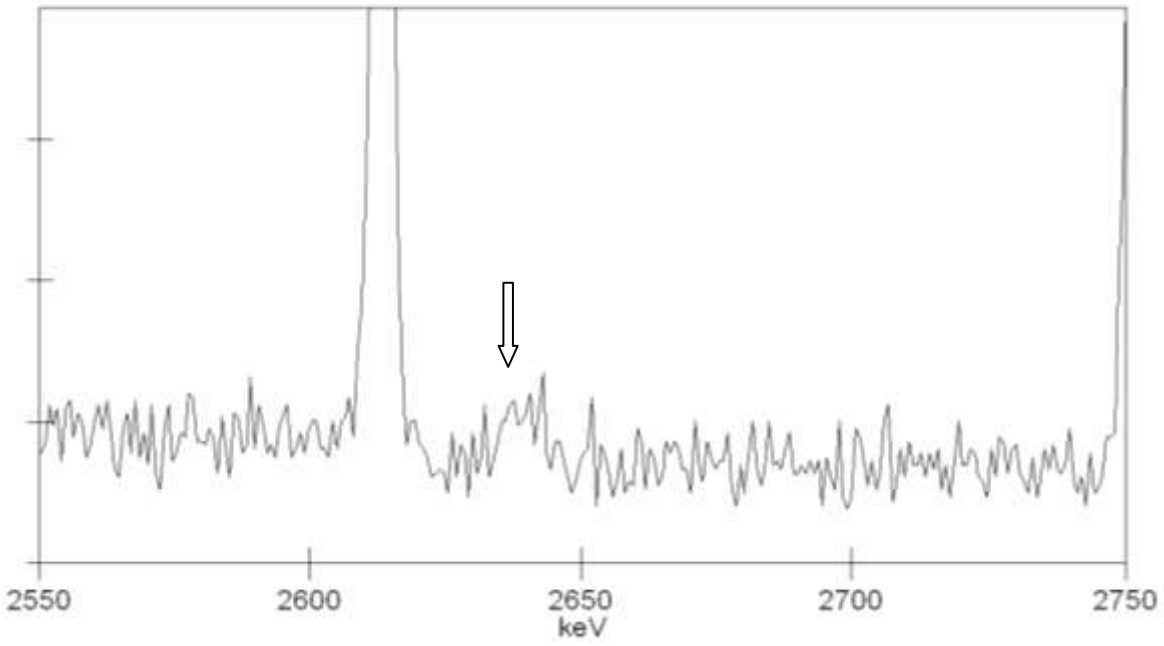

Fig. 4.25: Section of the “laser on” sum spectra on mass 131, 2550 to 2750 keV

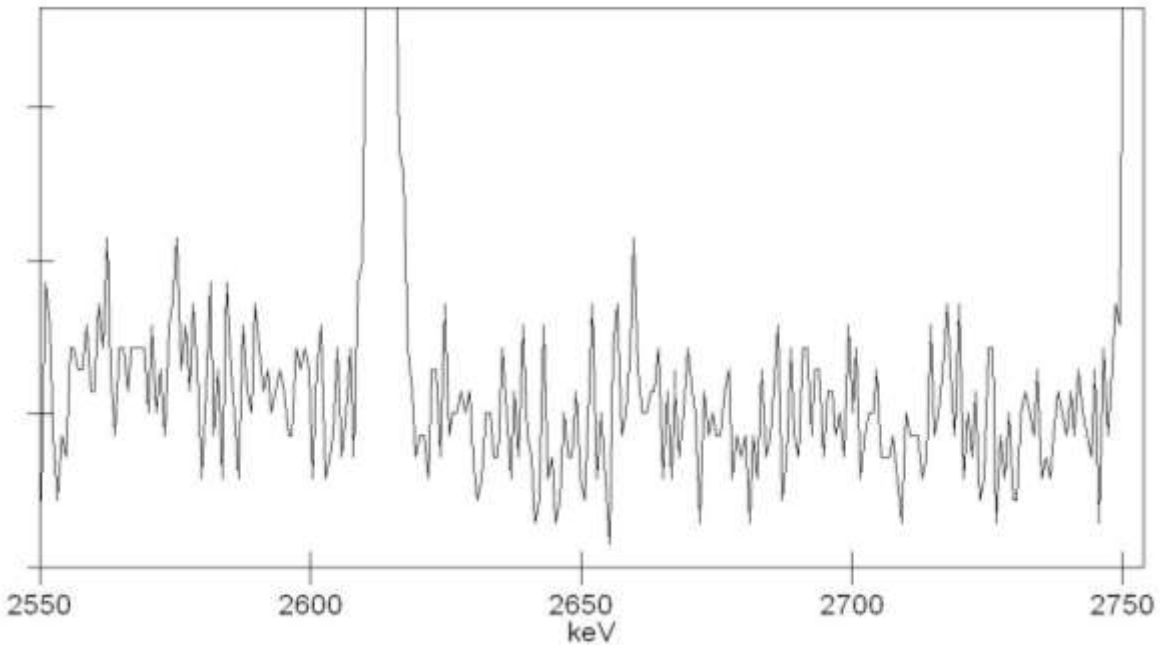

Fig. 4.26: Section of the “laser off” sum spectra on mass 131, 2550 to 2750 keV

3866keV

Another low intensity line that is present in the “laser on” spectra only shows at 3866keV. It could not be assigned to another nuclide.

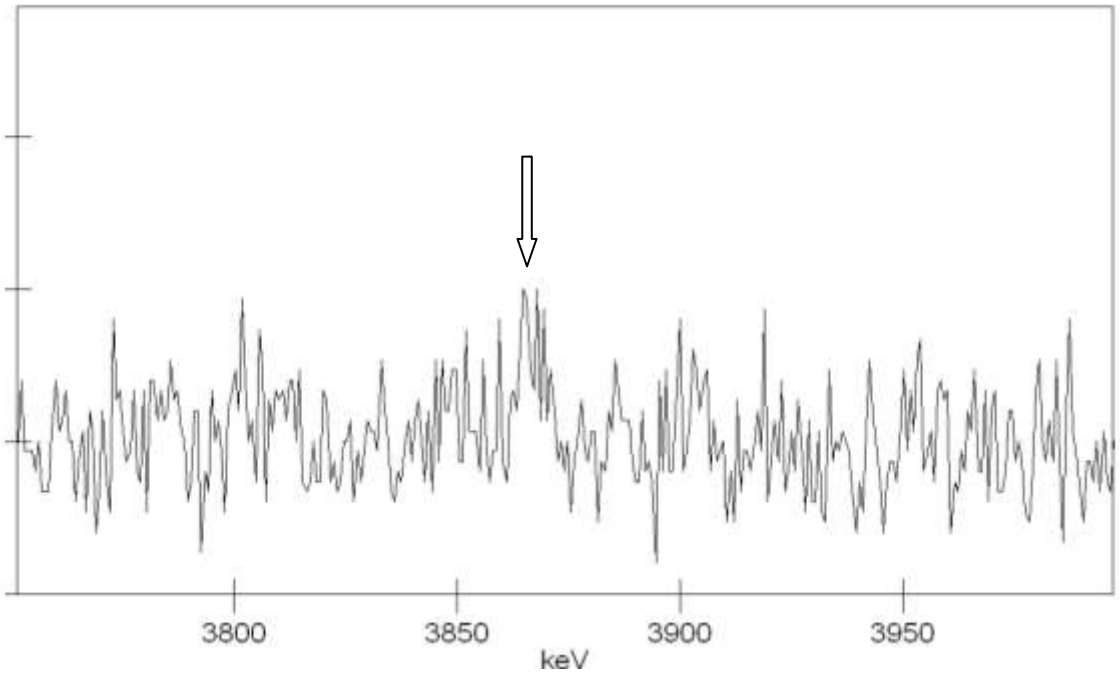

Fig. 4.27: Section of the “laser on” sum spectra on mass 131, 3750 to 4000 keV

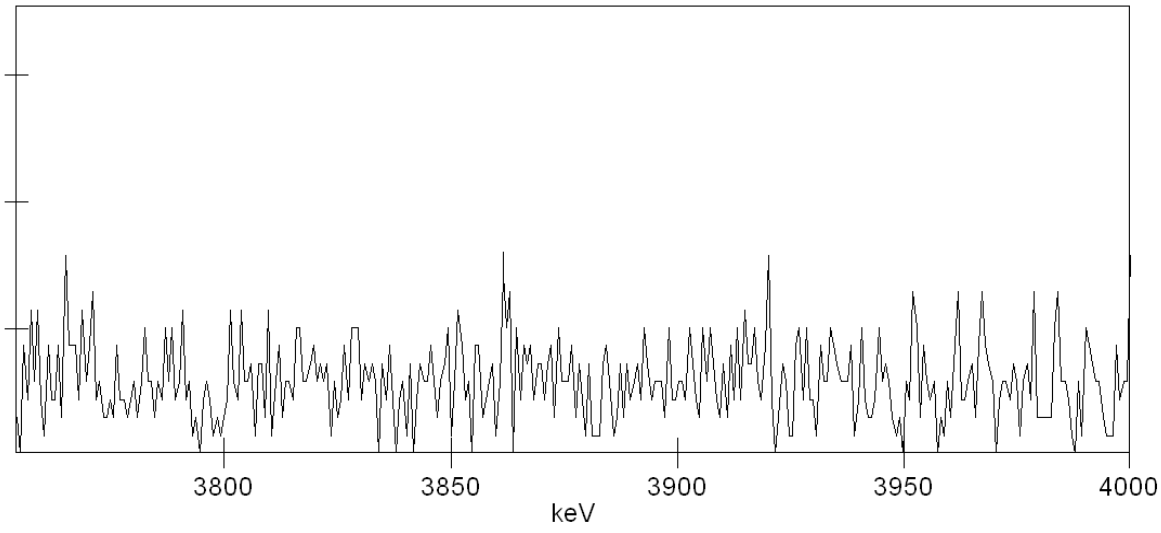

Fig. 4.28: Section of the “laser off” sum spectra on mass 131, 3750 to 4000 keV

6038 keV

The highest energy line detected in the “laser on” spectra only was found at 6039keV. The line at 6129keV is from the decay of ^{16}N, produced by an (n,p) reaction on ^{16}O, which is commonly found in the background at ISOL facilities.

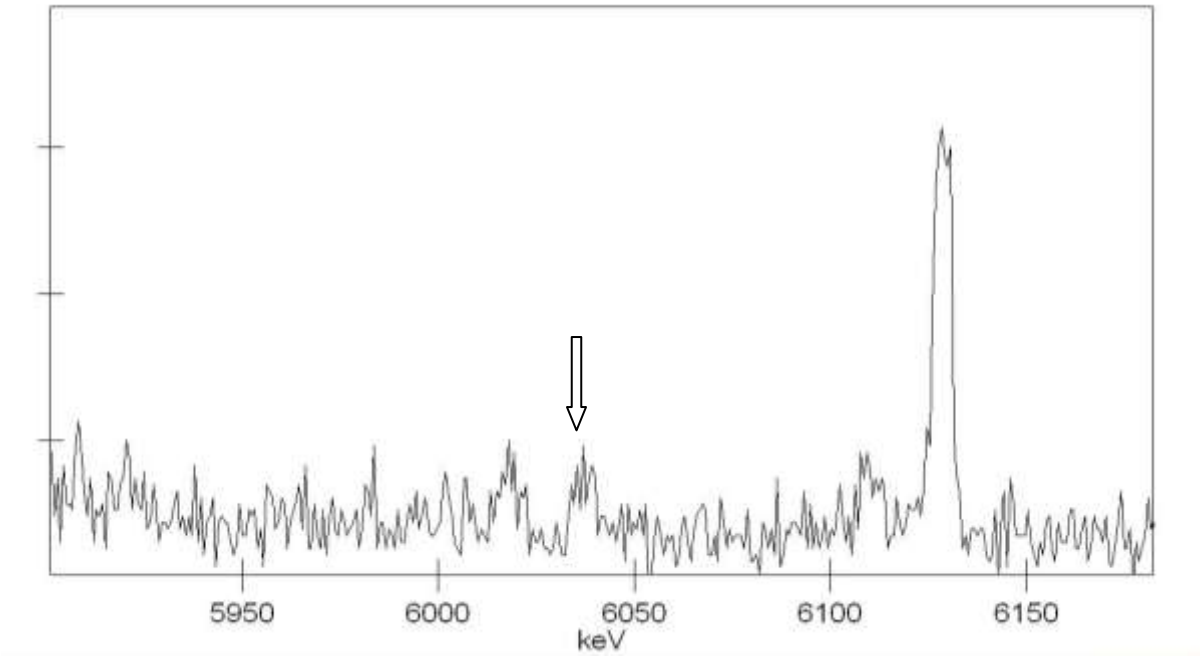

Fig. 4.29: Section of the “laser on” sum spectra on mass 131, 5950 to 6200 keV

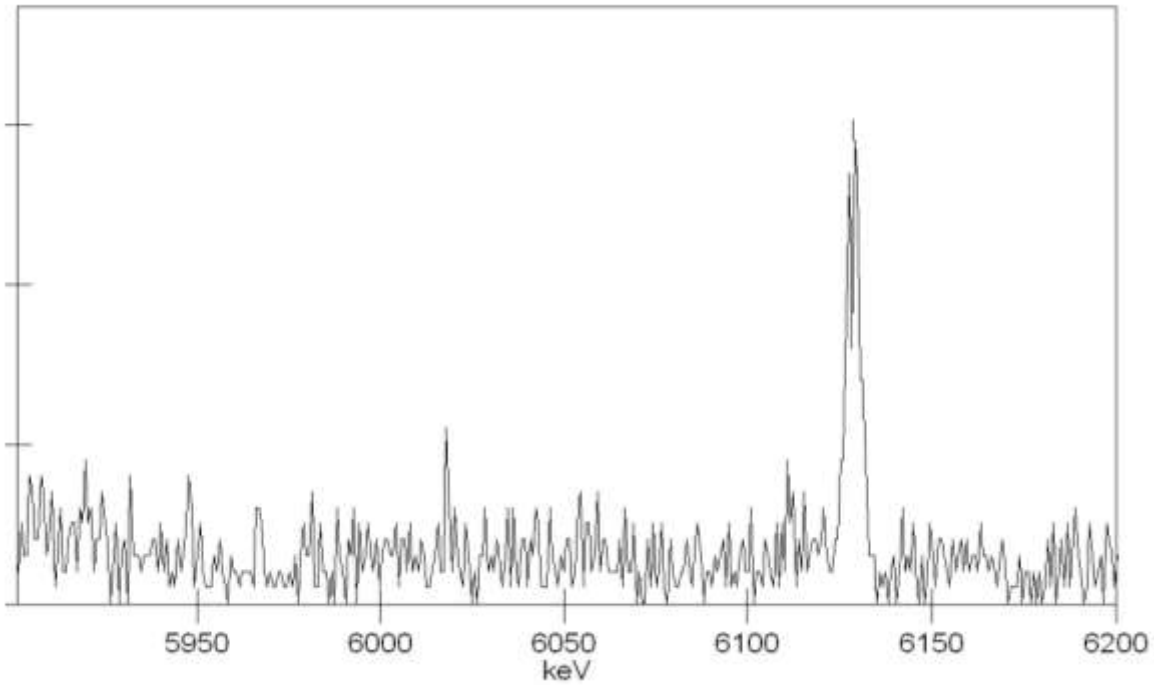

Fig. 4.30: Section of the “laser off” sum spectra on mass 131, 5950 to 6200 keV

4.2.3 Discussion

The main points of interest in this experiment are a) the development of the π $p_{3/2}$- π $p_{1/2}$ spin-orbit splitting towards the shell closure and b) the depth of the $f_{5/2}$ level with increasing N/Z.

Experimentally, a steady increase of the spin-orbit splitting has been observed, from 261 keV in ^{115}In to 524 keV in ^{127}In, and a tentative result of 631 keV in ^{129}In (Kratz, 2005). Values between 0.6 and 1.4 MeV have been predicted (see table 4.17). For the $\pi p_{1/2} - \pi f_{5/2}$ transition, which provides information about the quadrupole proton strength, the experimentally found energies increase from 706 keV to 976 keV (^{115}In to ^{127}In). Models predict energies between 1.3 MeV and 2.6 MeV (Leander, 1984) (Heyde, 1980) (Brown, 1998).

Table 4.17: Proposed energy levels for ^{131}Cd from various models

Energy splitting (MeV)	Heyde (1980)	Leander (1984)	Brown (1998)	QRPA (2004)	Exp.
$p_{1/2} - p_{3/2}$	0.6	1.4	1.1	1.3	0.84
$p_{1/2} - f_{5/2}$	1.3	2.6	2.6	2.4	2.64

Fig. 4.31 shows the decay scheme of ^{131}Cd as proposed by Hannawald et al. (Hannawald, 2000) after experimentally determining a surprisingly short half-life ($t_{1/2}$ = 68 ± 3 s) and low beta delayed-neutron emission probability (P_n = 3.5 %). A relatively high Q_β value of 12.6 MeV from the EFTSI-Q formula was introduced to reduce the half-life for Gamow-Teller (GT) decay; the lowest 3QP state fed by the $\nu g_{7/2} \rightarrow \pi g_{9/2}$ GT transition was shifted down below the neutron separation energy S_n to account for the low beta delayed-neutron emission probability. To reproduce the higher Q_β value and the shift of the 3QP state, a modified Nilsson potential with a reduction of the l^2 term by 25 % was used in the calculations. This also leads to a downward shift of the other low-lying 1QP and 3QP states relative to QRPA predictions.

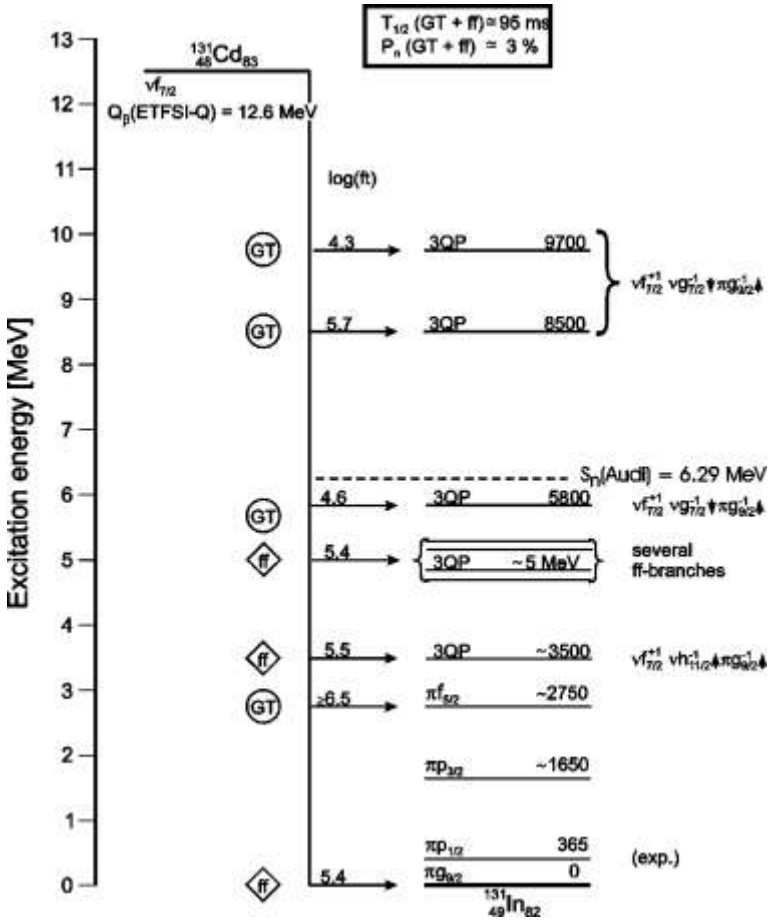

Fig. 4.31: Decay scheme of ^{131}Cd as proposed by Hannawald et al.

Fig. 4.32 shows the tentative assignment of the observed gamma rays:

- The 841 keV line corresponds to the π $p_{3/2}$- π $p_{1/2}$ energy difference, resulting in the π $p_{3/2}$ level being placed at 1146 keV.
- The 2640 keV line is assigned to the π $f_{5/2}$ to π $p_{1/2}$ decay. This places the π $f_{5/2}$ level at 2945 keV.
- The 3866 keV line is assigned to the lowest 3QP level and its decay into the ground state.
- The 6038 keV line corresponds to the 3QP level just below the neutron separation energy.

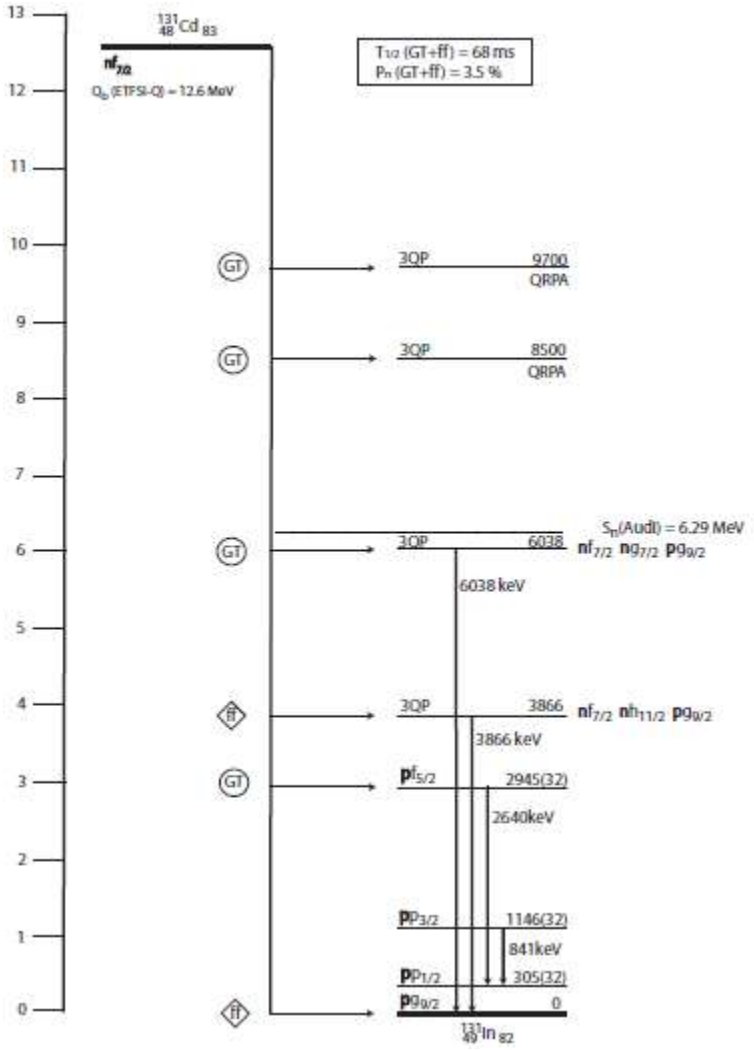

Fig. 4.32: Tentative level scheme for ^{131}In

In this scheme, the π $p_{1/2}$ was set at 305(32) keV, derived from the Q_β values given in (Fogelberg, 2004). The M1 transition from the $f_{5/2}$ to the $p_{3/2}$ level should have a similar transition probability as the E2 transition from $f_{5/2}$ to $p_{1/2}$. The gamma energy observed should be approximately 1799 keV. However, it could not be detected in this experiment, possibly due to a higher background at lower energies.

With this assignment of energy levels, both the spin-orbit splitting and the energy of the $f_{5/2}$ to $p_{1/2}$ follow the trend shown by the lower mass In isotopes. The increase of the spin-orbit splitting is lower than predicted by most models (see table 4.17), while the value of the $f_{5/2}$ to $p_{1/2}$ transition is consistent with the upper end of the range of predicted values. Overall, the model by Brown (Brown, 1998) agrees best with the experimental values.

5 CONCLUSIONS

5.1 Target-ion source development

The purpose here was to investigate and quantify the interactions of elements with different surface materials and the application of these interactions for radioactive ion beam purification.

This has been done using one off-line and two on-line methods: thermochromatography, measurements of yields and determination of hold-up times. All three methods seem to be well suited to investigate adsorption behavior and all produced consistent results.

Thermochromatography allows the most control over experiment parameters and yields very precise information on adsorption enthalpies; however, because of the use of an inert gas flow, results may not be directly transferable in the case of an irreversible interaction.

The two online methods were executed using a specially designed target-ion source unit with a variable-temperature transfer line and an opening to change transfer line surfaces. The system proved to be well suited to the task; however, a capability to reach even lower line temperatures would increase the sensitivity and precision of the measurements.

Yield measurements directly show the suppression of an element when changing temperature or surface material and allow the investigation of a broad range of elements in a comparatively short time. It is, however, not as sensitive to small changes in adsorption behavior as the other methods.

Hold-up time parameters are very sensitive to variations in sticking times and allow determination of adsorption enthalpies as well. Cases of irreversible interaction of atoms with a given surface will, however, not be detected with this method.
Thus the two online methods complement each other in the investigation of adsorption behavior on-line and the method must be carefully chosen for each case.

The results presented here show that there is indeed a chemical interaction of elements with a given surface; its strength and mechanism vary depending upon the combination of adsorbate and surface. Rb on quartz glass is a good example for a strong, at-least-partially irreversible interaction; Ag shows a strong but reversible

interaction with both Ta and quartz glass. The noble gases are good examples for weak to non-existent interactions with any surface.
Knowing the interactions of produced radionuclides with all surfaces present in the target-ion source unit is critical for the production of high-intensity beams. Sufficiently strong interactions like the one of Rb on quartz glass or Ag on low-temperature Ta can be used for beam purification.

Comparison with the results gained at ISOLDE make it seem likely that the yield suppression observed there are not solely the effect of a chemical interaction of alkali metals with the quartz glass surface. The effects of changing the geometry, surface material and area for surface ionization and temperature of the transfer line appear to contribute to the reduction of yields of easily surface-ionized elements extracted from a surface ion source.

These results have led to a better understanding of adsorption processes in the transfer line and their dependence on temperature and surface material. This is very useful for the optimization of yields of radioactive nuclides. However, it seems that in most cases investigated, the interactions are not strong enough to lead to a significant purification of radioactive ion beams. Furthermore, no new adsorption material that can remove a contaminant has been found.

Investigations of other, more specific, adsorption materials and in lower temperature ranges may prove to be more successful. Examples for these materials are graphite or zeolites with tailored surface area properties.

5.2 Spectroscopy

The obtained data of ^{131}Cd are proof of the improvement in beam quality achieved by the use of the medium-temperature quartz transfer line. The spectra show very little isobaric contaminations. Several new lines for ^{131}In have been detected.

Since the acquisition system could not take coincidence data, the assignation of levels is necessarily tentative. However, the results seem to be very consistent with predictions based on the short half-life and low probability for beta-delayed neutrons. For the spin-orbit splitting and the $f_{5/2}$ hole the levels in ^{131}In seem to follow the trend that has been observed for the less neutron rich In nuclides. The results are also in good agreement with more recent nuclear structure models, *e.g.* (Brown, 1998).

6 BIBLIOGRAPHY

Alton, G. D. (1993). *Nucl. Instr. Meth. 328* , 325-329.

Alton, G. D. (1998). *Physics Div. Progress Report ORNL-6957* .

Becquerel, H. (1896). *Compte Rendus 122* , 420 ff.

Becquerel, H. Comptes Rendus . *122*.

Bouquerel, E. (2007). *Eur. Phys. J. Special Topics 150* , 277-280.

Bouquerel, E. (2008). *Nuclear Instruments and Methods in Physics Research B 266* , 4298-4302.

Brown, B. A. (1998). *Phys. Rev. C 58* , 220 ff.

Carter, H. K. (1997). *Nucl. Instr. Meth. B 126* , 166-169.

Carter, H. K. (2008). *Nucl. Instr. Meth. B 266* , 4702-4705.

chemistry, H. (n.d.). *HSC chemistry*. Retrieved 6 1, 2010, from http://www.hsc-chemistry.net/

Cowlard, F. L. (1967). Vitreous Carbon - A New Form of Carbon. *Journal of Materials Science 2* , 507-512.

Dresser, M. J. (1968). *J. of Appl. Phys. 39* , 338 ff.

Eberhart, K. (2000). *Kerntechnik 65* , 269-274.

Eichler, B. (1982). *Radiochim. Acta 30* , 233 ff.

Fick, A. E. (1859). *Ann. Phys. 94* , 59 ff.

Fogelberg, B. (2004). *Phys. Rev. C 70* .

Fujioka, M. (1981). *Nucl. Instr. Meth. 186* , 409-412.

G. D. Alton, Y. L. (2000). *Nucl. Instr. Meth. B 170* , 515-522.

G. D. Alton, Y. L. (2006). *Rev. of Sci. Instr. 77* , 03A711.

Gilliland, E. R. (1934). *Ind. Eng. Chem. 26* , 681 ff.

Glicksman, M. E. (2000). *Diffusion in solids: field theory, solid-state principles and applications.* NY: Wiley.

Gobain, S. (2009). Retrieved 5 25, 2010, from http://www.saint-gobain.com/en/group/innovation-and-research/new-products/saphir

H. Rossbach, B. E. (1984). ZfK Rossendorf.

Hannawald, M. (2000). *Phys. Rev. C 62* .

Heyde, K. (1980). *Phys. Rev. C 22* , 1267 ff.

Hickmann, U. (1993). *Radiochim. Acta 60* , 127-132.

Hohn, A. (2004). *Radiochim. Acta 92* , 513-516.

Hoyle, F. (1954). *Astrophysical Journal, Supplement Series 1* , 121-146.

Ingram, M. (1992). *Phys. Rev. Lett. 86* , 3064 ff.

Inst, G. (1996). *Gmelin Handbook of Anorganic Chemistry.* Berlin: Springer.

InterWinner. (2000). *InterWinner*. Retrieved 5 25, 2010, from http://www.itech-instruments.com/InterWinner.pdf

Jost, C. (2005). *Diploma thesis.*

Koester, U. H. (2001). *Radiochim. Acta 89* , 749-756.

Kofoed-Hansen, O. (1951). *Phys. Rev. 82* , 96-97.

Kogan, M. N. (1969). *Rarefied Gas Dynamics 88-89.* Plenum Press.

Kratz, K.-L. (1986). *Z. Phys. A - Atomic Nuclei 325* , 489 ff.

Kratz, K.-L. (2005). Addendum to INTC-Proposal P135.

Kronenberg, A. (2008). *Nucl. Instr. Meth. B 266* , 4267-4270.

Lambert, J. H. (1760). *Photometria sive de mensure de gratibus luminis, colorum umbrae.* Eberhart Klett.

Langmuir, I. (1925). *Proc. Roy. Soc. London 107* , 61 ff.

Leander, G. (1984). *Phys. Rev. C 30* , 416 ff.

Lettry, J. (1997). *Nucl. Instr. Meth. B 126* , 130-134.

Lettry, J. (1998). *Rev. of Sci. Instr. 69* , 761-763.

Lettry, J. (2003). *Nucl. Instr. Meth. B 204* , 363-367.

Liu, Y. (2009). *Application of Accelerators in Research and Industry 1099* , 737-741.

Loeb, L. B. (1934). *The Kinetic Theory of Gases.* McGraw-Hill Book Company, Inc.

Maxwell, J. C. (1866). *On the Dynamical Theory of Gases.* F.R.S.L.& E.

Pauling, L. (1925). *J. Am. Chem. Soc. 47* , 781-790.

Rudstam, G. (1965). *Nucl. Instr. Meth. 38* , 282 ff.

Rudstam, G. (1973). *Radiochim. Acta 20* , 85-91.

S. Sundell, H. R. (1992). *Nucl. Instr. Meth. B 70* , 160-164.

Santana-Leitner, M. (2005). *PhD thesis.*

Schaedel, M. (2003). *The Chemistry of Superheavy Elements.* Kluwer Academic Publishers.

Spejewski E.H., C. H. (2008). ISOL yield predictions from hold-up time measurements. *NIM B* , 4271-4274.

Stix, T. H. (1992). *Waves in Plasmas.* New York, Berlin, Heidelberg: Springer-Verlag.

Stracener, D. W. (2003). *Nucl. Instr. Meth. B 204* , 42 ff.

Thomas. (1997). *Principles and Practice of Heterogeneous Catalysis.* VCH.

Vertes, A. (2003). *Handbook of Nuclear Chemistry 5.*

Wolf, B. (1995). *Handbook of Ion Sources.* CRC Press Inc.

Wovchko, E. (1995). *Langmuir 11* , 2592-2599.

7 ACKNOWLEDGEMENTS

This research was partly sponsored by the Deutsche Forschungsgemeinschaft and the National Nuclear Security Administration under the Stewardship Science Academic Alliances program through U.S. Department of Energy Cooperative Agreement #DE-FG52-08NA28552 through a contract between Rutgers University and Oak Ridge Associated Universities.